ADDITIVE MANUFACTURING OF NiTi SHAPE MEMORY ALLOYS WITH BIOMEDICAL APPLICATIONS

Additive Manufacturing of NiTi Shape Memory Alloys with Biomedical Applications

By

Ali Safdel, BSc., MSc.

A Thesis

Submitted to the School of Graduate Studies in Partial Fulfillment of the Requirements

for the Degree Doctor of Philosophy

McMaster University

DOCTOR OF PHILOSOPHY (2023) McMaster University

(Mechanical Engineering) Hamilton, Ontario

TITLE: Additive Manufacturing of NiTi Shape Memory Alloys with Biomedical Applications

AUTHOR: Ali Safdel

B.Sc. in Materials Science and Engineering (Iran University of Science and Technology)

M.Sc. in Materials Science and Engineering (University of Tehran)

SUPERVISOR: Dr. M. A. Elbestawi

NUMBER OF PAGES: xxii, 171

Dedicated to

My beloved parents, Monireh and Saeed

for their endless support and encouragement

My wonderful wife, Dr. Nafiseh Zaker

for her love, patience, and devotion

Preface

This Ph.D. thesis has been prepared by following the guidelines established by McMaster University on writing an integrated article thesis, also known as a sandwich thesis. The thesis is comprised of six main chapters discussing the laser powder bed fusion processing of NiTi alloys and their applications. Chapters 2-5 are composed of four journal papers and the corresponding citation and contributions are listed in the following:

Chapter 2: a version of this chapter is published as a research article, titled “New insights on the laser powder bed fusion processing of a NiTi alloy and the role of dynamic restoration mechanisms”, in the “Journal of Alloys and Compounds 885 (2021)”. Ali Safdel conducted the experiments, acquired the data, performed the analysis, and wrote the initial draft and Dr. Elbestawi revised the manuscript.

Chapter 3: a version of the provided discussions in this chapter is published as a research article entitled “The role of texture and restoration mechanisms in defining the tension-compression asymmetry behavior of aged NiTi alloys fabricated by laser powder bed fusion”, in the “Materials Science and Engineering: A (2023)” journal. Ali Safdel performed the experimental work, collected the data, and wrote the initial draft. Dr. Nafiseh Zaker prepared samples for transmission electron microscopy by plasma-focused ion beam and contributed to the discussions related to the presence of precipitates. Dr. Botton revised the initial draft, and Dr. Elbestawi reviewed and edited the manuscript.

Chapter 4: a version of this chapter has been published as a short communication (letter), titled as “Distortion and printability of stent structures in laser powder bed fusion

processing of NiTi alloys" in the "Materials Letters 300 (2021)" journal. Ali Safdel conducted the experiments, performed the simulations, analyzed the data, and wrote the first draft. Dr. Elbestawi revised and edited the manuscript.

Chapter 5: a version of this chapter is currently submitted for peer review to the "Journal of Alloys and Compounds" as a research article entitled "Laser powder bed fusion of differently designed NiTi stent structures having enhanced recoverability and superelasticity". Ali Safdel performed the experimental works, acquired, and studied the data. Dr. Torbati-Sarraf contributed to the paper by conducting the X-ray computed tomography scans and post-processing the raw data. Dr. Elbestawi reviewed and edited the initial manuscript.

Lay Abstract

This study focuses on the laser powder bed fusion processing of NiTi alloys and the feasibility of fabricating very thin stent structures for biomedical applications. A comprehensive correlation between the process and the material's-structure and properties is established to facilitate the fabrication of NiTi alloys with tailored properties. In the first step, the impact of LPBF processing parameters and post-treatments on evolving the microstructure, texture, superelasticity, and asymmetry is examined. Subsequently, the feasibility of manufacturing very thin mesh structured stents is scrutinized followed by in-depth investigations into differently designed stents considering properties such as surface characteristics, mechanical properties, superelasticity, and recoverability. The obtained results and the represented discussions offer imperative insights, helping to better understand the complexity of the LPBF process and the present challenging aspects. Moreover, detailed contributions are made with the goal of paving the road ahead for the production of patient-specific NiTi stents with enhanced properties.

Abstract

Laser powder bed fusion (LPBF) has proven to be a versatile additive manufacturing technique to manufacture metallic components with intricate geometries in a controlled atmosphere. To this end, several studies in recent years aimed to assess the capabilities of this approach to fabricate NiTi alloys, which are known to be notorious during production due to the strict composition requirements, impurity pickup, formation of undesired secondary phases, and the need for specific vacuum furnaces. Moreover, the flexibility of readily changing the design is another task that conventional approaches fail to perform. NiTi alloys are classified as smart materials and are widely used in the biomedical industry to manufacture stents and implants owing to their remarkable flexibility, superelasticity, and biocompatibility. Nonetheless, there are also various challenges with LPBF in order to fabricate high quality parts, necessitating in-depth systematic investigations. Taking the current literature into account, this thesis is divided into two phases, from which the first one aims to provide new insights and perspectives to manufacture NiTi alloys with tailored properties and the second phase consists of a series of meticulous studies to assess the feasibility of fabricating thin mesh-structured stents with improved superelasticity and recoverability.

To this end, the first chapter initially focuses on one of the most problematic challenges during the LPBF process which is the generation of high residual stresses, delamination, and process termination. Through experimental and modeling, an optimum range of processing parameters is identified initially, which can result in the fabrication of highly dense parts with very low levels of stress and negligible nickel loss. The generation of

stresses during the process at higher temperatures could stimulate the occurrence of the dynamic restoration mechanisms, affecting the parts' mechanical properties and transformation behavior.

Secondly, the identified optimum processing parameter was employed to manufacture tensile and compressive specimens, and the superelasticity and asymmetrical behavior of fabricated NiTi alloys were assessed after subsequent aging treatments. It was established that texture is highly affected by both dynamic and static restoration mechanisms during the LPBF and aging, respectively. In this regard, the asymmetrical superelastic behavior of NiTi alloys could be tuned based on the intended applications.

Third, the capabilities of the LPBF process to manufacture a very thin NiTi stent were assessed by simulations and the in-process vertical distortion, proving that stents can be manufactured via LPBF if a lower level of volumetric energy density is used.

Lastly, benefiting from the findings and the results of the previous steps, differently designed meshed stent structures having very thin struts were successfully manufactured via the LPBF approach. These highly dense stents were able to exhibit comparable surface characteristics, mechanical properties, superelasticity, and recoverability after deformation, which are all important to further advance the frontiers of knowledge in the field of additively manufactured stents with the aim of producing high quality adaptable patient-specific stents in the future.

Acknowledgments

First and foremost, l would like to extend my sincere gratitude to Dr. Elbestawi, my supervisor and mentor, who has supported me in every step of my research with his knowledge and patiently guided me to overcome the most difficult obstacles that I have faced in this journey. His encouragement and commitment are unparalleled, and I am honored to have pursued my Ph.D. studies under Dr. Elbestawi's supervision.

I would also like to express my appreciation to Dr. Grandfield and Dr. Selvaganapathy, for their meticulous attention to the details of my project and their insightful and constructive comments and feedback. Their knowledge helped me to devise concrete plans at each step and navigate through the challenges. I am also grateful to Dr. Javier Ganame for our many discussions related to the medical aspects of the project. Moreover, I would like to thank our collaborators, Dr. Zaker and Dr. Botton who conducted the sample preparation and acquired transmission electron microscopy images, and Dr. Torbati-Sarraf who obtained and analyzed the X-ray computed tomography data.

I would also like to show my gratitude to the staff of the department of mechanical engineering, the department of materials science and engineering, and the Canadian center for electron microscopy (CCEM) at McMaster University who taught me and trained me to use a variety of complicated instruments throughout these years. I am also grateful for having highly knowledgeable colleagues and friends in the "Additive Manufacturing Group" at McMaster University, and for the scientific discussions we had over the past four years.

Words cannot describe how grateful I am to my family and friends, who loved and supported me unconditionally and encouraged me to jump higher with each step. I am blessed to have such wonderful loving parents, compassionate in-laws, an amazing brother (Sepehr), and a kind sister-in-law (Narges). Last but not least, I am proud and grateful to have a brilliant wife, Dr. Nafiseh Zaker, who has always inspired me to have dreams, encouraged me to reach my goals, and taught me to enjoy the journey, no matter how difficult it can get.

Contents

Page

List of Figures

List of Tables

Chapter 1

Introduction

1.1 Background

In the early 1960s, Buehler and his coworkers at the naval ordnance laboratory (NOL) in the United States discovered a very unique behavior for an equiatomic alloy consisting of both Nickel and Titanium (Ni-Ti), which was later named the shape memory effect (SME). This discovery has been considered a breakthrough ever since and to this date, NiTi alloys are also commonly referred to as Nitinol [1]. Having unique properties such as SME and superelasticity (SE), in addition to low elastic anisotropy, high ductility, corrosion resistance, and acceptable biocompatibility, led to countless investigations throughout the years to understand the behavior of this exceptional material [2–4]. These studies resulted in numerous applications for NiTi alloys in various fields, including aerospace, civil, military, automotive, and most importantly biomedical industry [5–7]. Nowadays, NiTi alloys are widely used to produce surgical tools, implants, orthodontic wires, guide wires, and specifically stents [8–13]. Figure 1-1 illustrates the Ti-Ni phase diagram, in which the highlighted middle region of the graph indicates the NiTi intermetallic compound. This region is wide enough to have a single NiTi phase structure owing to the certain solubility of Ni and Ti in each other. However, any deviations from the semi-equiatomic composition can lead to the formation of other secondary phases which can affect the material's

functional and mechanical properties. Thus, controlling the composition of the material during manufacturing is imperative, and is one of the many challenges to fabricate NiTi components with tailored properties [14].

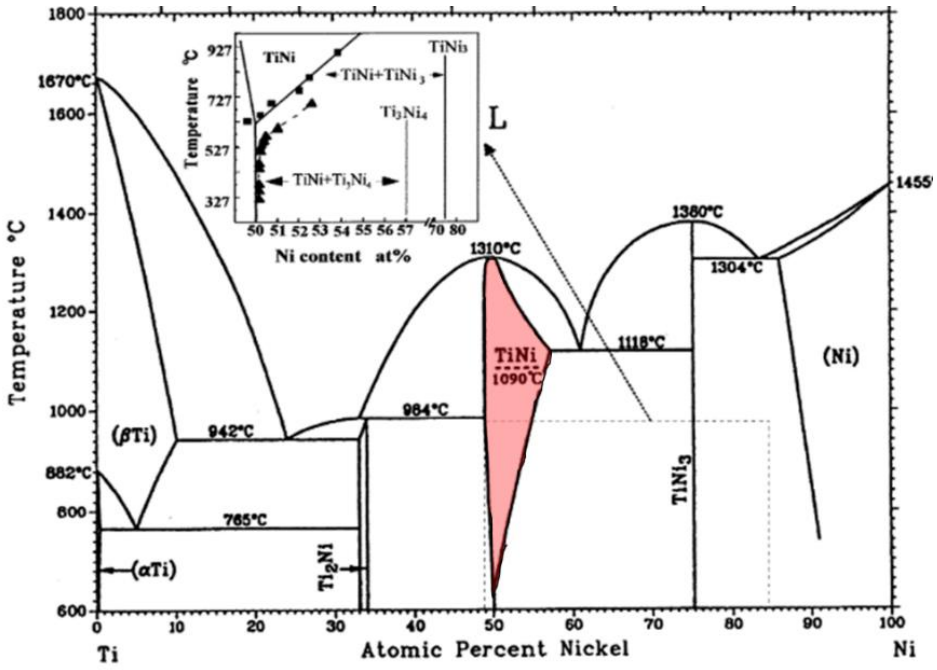

Figure 1-1 Phase diagram of the Ni-Ti alloy [14].

Microstructural studies of the NiTi alloy have revealed the presence of two main temperature-dependent phases: austenite and martensite, with notably different mechanical properties. Austenite, as the high-temperature phase, possesses a symmetric cubic B2 structure, while martensite, as the low-temperature phase, has an asymmetrical monoclinic B19' crystal structure. [15–17]. Thermoelastic martensite transformation can be induced either thermally, or mechanically due to the mobile interface of the austenite and martensite phase, causing SME or SE to occur [18–20]. The transformation between the martensite and austenite phases during heating or cooling is shown in Figure 1-2 by differential scanning calorimetry (DSC) curves. The austenite phase starts to transform into the

martensite phase during cooling at M_s temperature, and the transformation ends at M_f temperature. Similarly, during heating, reverse transformation occurs, causing the martensite structure to transform back to austenite (in the temperature range of A_s to A_f). These two transformations can be easily identified by the exothermic or endothermic peaks in the DSC graph, respectively [21].

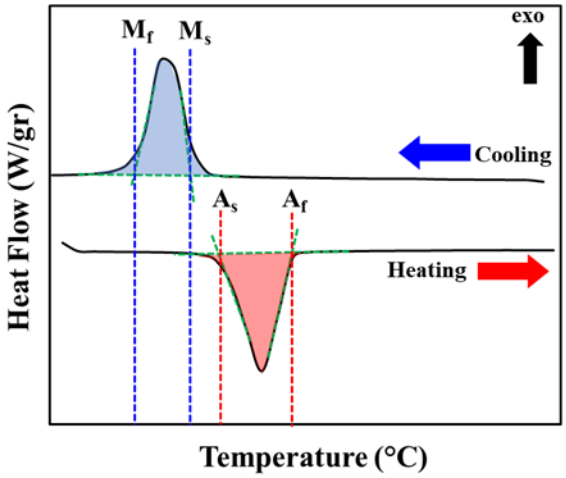

Figure 1-2 A typical DSC curve of an equiatomic NiTi alloy [21].

The martensitic phase transformation can also be triggered by mechanical deformation. Tensile stress-strain curves of a semi-equiatomic NiTi alloy, tested at two different temperatures, are shown in Figure 1-3. For the blue curve, the testing temperature was below M_f, which denotes that martensite was the stable phase, and for the red curve, the temperature was above A_f, indicating that austenite was the primary phase. The curves have been divided into four different zones denoting the involved microstructural evolution mechanisms. In this regard, regime I in both curves indicates the elastic deformation of the stable phase, whether it is austenite or martensite. Upon reaching a certain stress level, a semi-plateau stress region is observed for both curves, attributed to the stress induced

martensite (SIM) transformation in the austenitic alloy and the detwinning of the twinned martensite variants in the martensitic alloy.

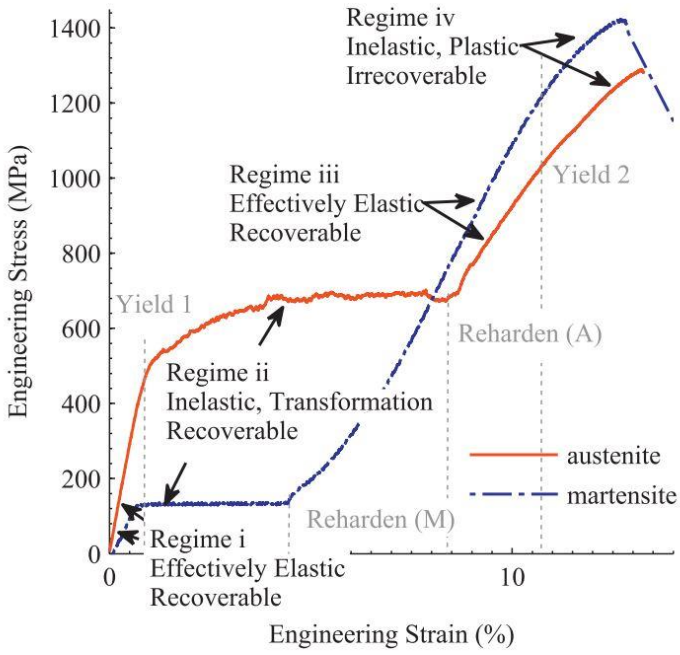

Figure 1-3 Tensile test curves at temperatures below M_f (blue curve) and above A_f (red curve) [22].

It is interesting to point out that in both cases, the accommodated strain is inelastic and can be recovered during unloading or heating the deformed material. Further deformation then leads to an increase in the slope of the curves, elastic deformation of the induced detwinned martensite, and ultimately plastic deformation of the material. This figure is particularly important since it presents a glimpse of how SME and SE occur, and accordingly, more details will be given in the following two sections to better define the underlying mechanisms [22].

1.1.1 Shape memory effect (SME)

The stress-strain-temperature curve of a NiTi alloy is illustrated in Figure 1-4(a), representing the SME. Starting at point A in the graph, for an alloy stored at temperatures above A_f, austenite is the main phase, which can transform into twinned martensite if cooled down to lower temperatures (B). Applying external stress to the present martensitic structure leads to reorientation and detwinning of the martensite variants and a macroscopic shape change. Detwinning, characterized by a stress plateau in the stress-strain curve, is defined as the process in which one of the martensite variants grows favorably in a specific direction at the expense of outgrowing and eliminating other variants (C). After unloading, this new configuration is retained (D), however, with subsequent heating to temperatures above A_f (E), reverse phase transformation from detwinned martensite to austenite occurs, and the initial shape of the material is recovered (A). This unique behavior is described as SME and its utilization leads to various applications, such as orthodontic wires and actuators [21].

1.1.2 Superelasticity (SE)

Through SE, a significant portion of strain can be recovered merely by unloading the deformed part. This phenomenon originates from the occurrence of the SIM transformation during the loading of an austenitic NiTi and the reverse transformation from martensite to austenite in unloading. The critical resolved shear stress (CRSS) is an imperative factor affecting the SIM transformation, which should be higher than the critical stress required for the activation of the SIM. In other words, by increasing the CRSS, plastic deformation and the activation of slip mechanisms during loading are postponed, providing the opportunity for the material to experience the SIM transformation before being

permanently deformed [23,24]. Figure 1-4(b) illustrates a theoretical stress-strain curve of a superelastic NiTi alloy during a typical load-unload tensile test.

As is shown in the figure, after the initial elastic deformation, SIM transformation (characterized by a stress plateau) starts to occur at a critical stress (σ_s), causing a phase change from austenite to martensite. Upon unloading, reverse transformation occurs, which forces the material to transform back to austenite, resulting in shape recovery. If the material was deformed to higher levels of strain, slip systems would have been activated, leading to plastic deformation and a definitive shape change. Many applications in various industries are benefiting from the superelastic behavior of NiTi alloys, with the biomedical industry taking the lead. In this regard, NiTi alloys with enhanced SE are used to manufacture stents, endodontic wires, implants, guidewires, and many other medical components [23,24]. It is worth mentioning that the occurrence of either SME or SE in Nitinol depends on several other factors as well, including temperature, chemical composition, present stable phase, and previous treatments [25].

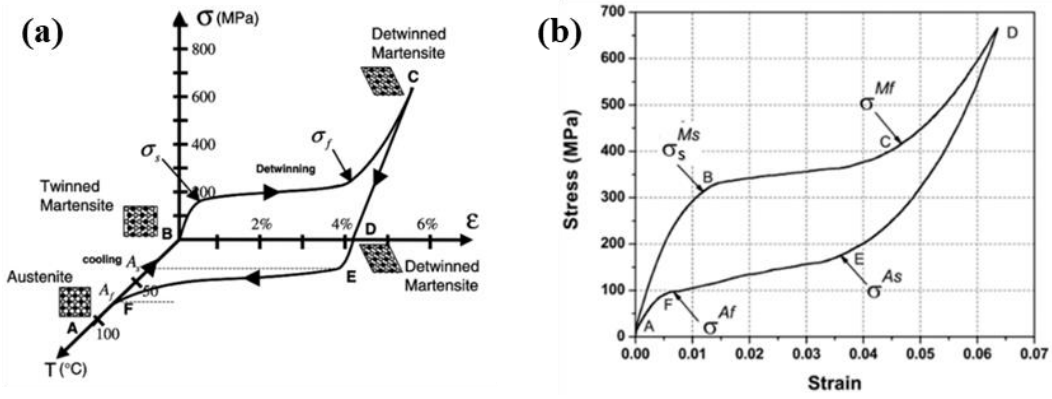

Figure 1-4 Schematic representation of (a) SME, and (b) SE response in NiTi alloys [21].

1.2 Fabrication methods of NiTi

Chemical composition plays a dominant role in determining the behavior of NiTi alloys, and even the slightest change in the composition can lead to significant alterations in the transformation temperatures, as illustrated in Figure 1-5(a). On the other hand, Ni evaporation during high-power processing procedures is quite probable, as is evident in Figure 1-5(b) from the considerably higher vapor pressure of Ni in comparison to Ti even at lower temperatures [16,26]. Therefore, controlling the composition of the NiTi alloy during fabrication is a challenging yet imperative task.

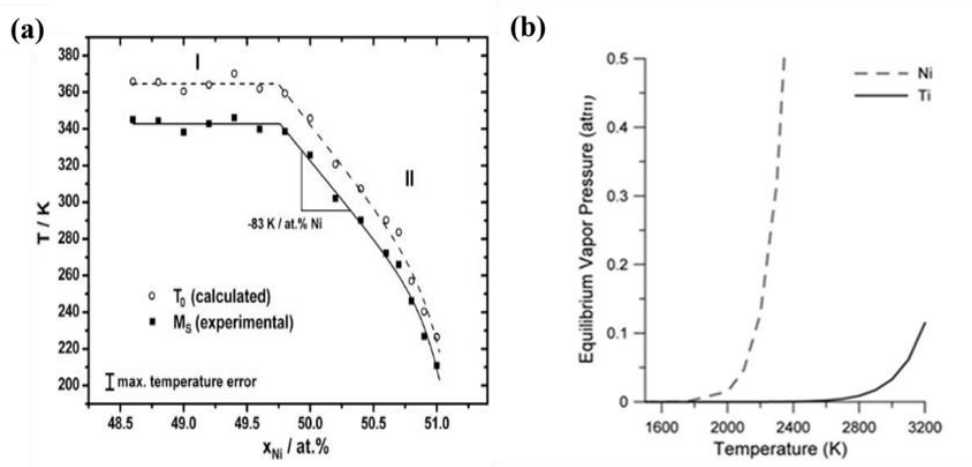

Figure 1-5 (a) M_s temperature vs. Ni content [16] and (b) the vapor pressure of Ni and Ti vs. temperature [26].

1.2.1 Conventional methods

The structural and functional properties of NiTi alloys, the nickel-titanium ratio, picked-up impurities and formed secondary phases are all highly dependent on the production method and processing parameters. Post-processing or machining is also extremely difficult due to the poor thermal conductivity, high elasticity, and frictional resistance of the alloy. Therefore, each fabrication step requires a deep understanding of its effects on the performance and quality of the final product [27]. Although there is no single recipe to

produce NiTi ingots, vacuum arc melting (VAM) or vacuum induction melting (VIM) techniques are conventionally used, followed by multiple heat treatments and machining processes [28]. Aside from casting approaches, powder metallurgy (PM) processing routes have also proved their capability to produce a near-net-shape component by overcoming some of the challenges of traditional methods. As illustrated in Figure 1-6, several conventional powder metallurgy processes have been used previously to manufacture NiTi components. Additive manufacturing, as an emerging powerful manufacturing approach, has been extensively used in recent years to produce metallic materials, which will be discussed in more detail in the following section [9].

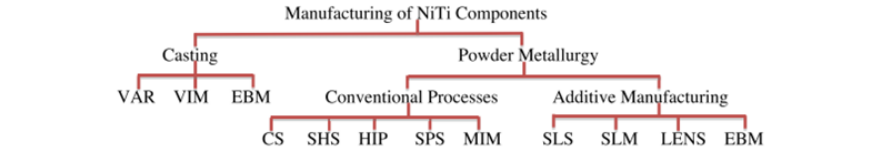

Method	Description	Method	Description
VAR	Vacuum Arc Remelting	SHS	Self-propagating High Temperature Synthesis (combustion) Synthesis
VIM	Vacuum Induction Melting	HIP	Hot Isostatic Pressing
EBM	Electron Beam Melting	SPS	Spark Plasma Sintering
CS	Conventional Sintering	MIM	Metal Injection Molding
SLS	Selective Laser Sintering	LENS	Laser Engineered Net Shaping
SLM	Selective Laser Melting		

Figure 1-6 Manufacturing techniques that are used to fabricate NiTi components [9].

1.2.2 Additive manufacturing

Consistent control of porosity (pore size, the arrangement of pores, and interconnection of pores), chemistry (impurity content, homogeneity, and intermetallic), and geometrical flexibility can not be achieved in conventional NiTi fabrication methods. With the advent of appealing Additive Manufacturing (AM) technologies in recent years, many of the mentioned issues were solved leading the scientific community to exploit these recently developed approaches to produce net shape Nitinol components. Especially, laser powder bed fusion (LPBF), as one the most prominent AM processes for fabricating metallic

materials, gained significant attention. LPBF utilizes a laser to provide enough heat to selectively melt a thin layer of powder that is distributed on a building platform in a sequential manner, contributing to the fabrication of the final part. This process is commonly referred to as selective laser melting (SLM) and is carried out in a chamber filled with high-purity Argon gas to minimize the effect of oxidation and impurity pickup and is highly capable of producing net-shape parts with complex geometries without requiring any major post processing [29–31].

1.3 Laser powder bed fusion of NiTi alloys

As was pointed out, the LPBF process employs a computer-aided design (CAD) model to selectively melt the metal powder by using a high power laser beam. During the process, numerous parameters such as laser power (P), powder layer thickness (t), scanning speed (υ), hatch spacing (h), and scanning strategy are all involved. According to the following equation, the volumetric energy density (E) is a parameter representing the correlation of the aforementioned factors and although it does not include many other influencing factors, it is widely used in the literature as a criterion determining "part printability".

$$E_v \text{ (J/mm}^3\text{)} = \frac{P}{\upsilon.h.t} \tag{1.1}$$

Processing parameters can define the microstructure, texture, surface characteristics, and properties of the material. The flexibility of readily changing the process parameters in LPBF can be exploited to control and alter the NiTi alloy microstructure, transformation temperatures, and the resulting mechanical behavior. The production of highly complex-shaped dense or porous NiTi parts with tailored properties is therefore feasible. Although few research groups around the world have focused on the LPBF processing of NiTi, much

work is yet to be done to fully understand the relations between the process, structure, and property (PSP) of the material. Moreover, only a handful of studies have been performed to produce high-quality parts and porous biocomponents, in which microstructural evolution has not been critically addressed [32–37].

1.3.1 Biomedical applications of AMed NiTi

Additively manufactured NiTi parts can be utilized in the biomedical industry by implementing correct processing parameters and proper post-treatment. For implant fabrication, porosity can be introduced throughout the structure to tune the stiffness in a way that matches the value of the bone. Thus, patient-specific stiffness-matched fixation implants can be manufactured [38]. Currently, additive manufactured NiTi surgical tools, orthopedic fixtures, bone staples, and various permeable implants are being investigated for possible clinical implications. For instance, Figure 1-7 demonstrates an additively manufactured porous tooth root which is inserted into a lower jaw to facilitate bone reconstruction.

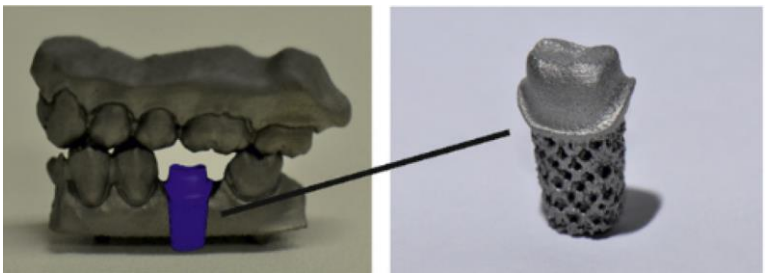

Figure 1-7 Additively manufactured porous NiTi tooth root [39].

Another important application for NiTi alloys is stents, which are utilized to treat coronary or peripheral artery diseases. Stents are tubular mesh-like structures that are inserted into a vessel or a tubular organ in the body to keep the passageway open. After being transported to the location where the intervention is required, NiTi stents can expand and reach their

final diameter. While different materials such as titanium, stainless steel, and cobalt chromium (CoCr) are being used to produce balloon-expandable stents, self-expandable NiTi alloys have exhibited promising outcomes owing to their superior superelastic properties and high level of biocompatibility. NiTi alloys can sustain elastic deformation up to 10% strain without any plastic deformation, which makes them uniquely appropriate to be deployed as self-expandable stents [40,41].

Currently, commercial stents are being produced by implementing a series of techniques such as tube preparation, laser micro-cutting, and subsequent heat treatment and surface modification processes. One of the many problems with these "off-the-shelf" stents is the occurrence of migration, due to the design difference between the artery and the stent, which causes the stent to move within the body, necessitating a second surgery to remove the unusable expanded stent.

In this regard, AM approaches have the potential to be exploited to fabricate patient-specific stents with desired geometry and tailored properties. At the time of the beginning of this project, this customization had not yet been carried out for stents, and no investigation had been performed to additively manufacture self-expandable NiTi stents with different designs. In recent years, less than a handful of studies [42–44] have started to focus on this imperative topic, although the designs were usually larger than functional stents, and meticulous examinations of mechanical properties, recoverability, and microstructure were mostly overlooked.

1.4 Motivation

According to the literature review, several topics have been identified which are not investigated comprehensively and therefore require more scrutiny. Although some studies

were conducted on LPBF of NiTi alloys, there is still a huge gap in fully understanding the process-structure-property relationships. Even for those studies, the researchers were mainly focused on the relationship between the process and the properties of the fabricated sample, while in-depth microstructural characterization and the underlying reasons for the observed results were left out.

Moreover, the capability of LPBF to fabricate very thin functional self-expandable NiTi stents with tailored properties has not been comprehensively assessed. Undoubtedly, the prerequisite of fabricating porous NiTi stent structures by LPBF is obtaining a comprehensive body of knowledge of the process-structure-property relationships. Microstructural features, mechanical properties, surface characteristics, and functional properties of the alloy are of utmost importance and should be fully understood to be able to fabricate porous biocomponents. The effects of heat treatment to improve the functional properties of the alloy, formation of secondary phases, and precipitates have been studied only for conventionally fabricated NiTi alloys and should also be studied for additively manufactured components according to their different microstructure and internal residual stresses. The asymmetric behavior of the fabricated parts, denoting the mismatch in the materials' response to the mode of deformation, should also be examined as well, considering most functional parts experience different deformation modes during their service conditions. Based on the presently available knowledge on additive manufacturing of NiTi alloys and the existing areas for further research, two main objectives were defined which are proposed in the following section.

1.5 Objectives

1.5.1 PSP relationship in NiTi alloys processed by LPBF

In this phase, according to the design of experiment (DOE) methodology and the existing research regarding LPBF of NiTi alloys, an optimized range of processing parameters is selected to fabricate cubic structures, tensile specimens, and cylindrical compression test samples. Density, chemical composition (Ni evaporation), mechanical properties, microstructural evolution, texture, superelasticity, asymmetrical behavior, and the effect of post-heat treatment is assessed, and contributions to the knowledge were made accordingly by publishing the results as two papers in high-impact journals. The goal was to optimize the properties of the part, by manipulating the processing parameters and the microstructure of the alloy. Throughout the LPBF process, the developed residual stresses, and the formation of secondary phases can also affect the material's properties which will be examined in this phase. Post-process heat treatment is also another factor that can be utilized to enhance the functional properties of the material which is another topic investigated in this phase. In summary, the first phase is divided into the following sub-objectives aiming to provide a comprehensive understanding of PSP relationships in NiTi alloys fabricated by LPBF:

- The effect of processing parameters on density, Ni evaporation, microstructural evolution, and texture of dense NiTi alloy manufactured by LPBF.
- The effects of processing parameters and post heat treatment on superelasticity, secondary phase formation, and the asymmetrical behavior of the material.

1.5.2 LPBF of high-quality NiTi stents with various designs

The second objective of this research takes advantage of the acquired data and the resulting optimum parameters of the first objective to produce high quality NiTi stents with different

designs. In the first step, the feasibility of fabricating thin stents will be assessed by considering the in-process distortion and the generation of residual stresses during the LPBF process. After confirming the processability, the manufactured stents are heat treated to reach their ultimate SE, and surface treatments are also carried out to improve their surface roughness. Fabricated stents are examined considering their structural integrity, density and internal porosities, compressive and bending behavior, and ultimately the SE behavior and the evolved microstructure are scrutinized as well. Accordingly, the following topics are considered in this phase:

- Utilizing optimum processing parameters to fabricate stents with different mesh structures and designs.
- Enhancement of surface characteristics by electropolishing treatments and assessing the level of internal porosities.
- Investigating the mechanical properties through compression, bending, and nanoindentation tests.
- Superelasticity and recoverability of the stents and microstructural characterization of the stents.

1.6 Thesis outline

Overall, the acquired results and data for this thesis have been prepared in a format of four publishable papers for each chapter from which three are already published and one is being revised according to the reviewers' comments. Accordingly, the thesis includes an introductory chapter in addition to the mentioned four main chapters which are all briefly denoted in the following:

Chapter 1 provides an introduction and the background related to NiTi alloys, their functional properties, manufacturing methods, and the advantages of additive manufacturing approaches to fabricate functional biomedical components.

Chapter 2 is dedicated to a comprehensive process-structure-property investigation on LPBF of NiTi, focusing on finding the optimum conditions for the fabrication of highly dense parts with negligible nickel loss and residual stresses. The possibility of the involvement of the dynamic restoration mechanisms and their effects during the LPBF process is examined by theoretical predictions, numerical modeling, and experimental data.

Chapter 3 deals with the subsequent heat treatment steps to enhance the superelasticity of the fabricated parts and the asymmetrical superelastic response is investigated in tensile and compressive deformation modes considering the effects of scanning strategy and the evolved texture during the LPBF and the conducted -aging treatment.

Chapter 4 provides a brief view of the capabilities of the LPBF process in the fabrication of stents with very thin struts considering the developed stresses, vertical distortion, and process continuation.

Chapter 5 benefits from the results of all the other previous chapters, in which high quality NiTi stents with different structural designs are fabricated by LPBF. The stents are examined and compared by considering surface roughness, dimensional accuracy, density, and internal structural integrity on the one hand, and their mechanical properties are assessed through compression, three-point bending, and nanoindentation tests, on the other hand. Superelasticity and the evolved microstructure are discussed as well.

Chapter 6 summarizes the main findings and conclusions of this research and defines the main contributions of the present thesis to the literature.

1.7 References

[1] N. El-Bagoury, M.M. Hessien, Z.I. Zaki, Influence of aging on microstructure, martensitic transformation and mechanical properties of NiTiRe shape memory alloy, Met. Mater. Int. 20 (2014) 997–1002. doi:10.1007/s12540-014-5003-0.

[2] A. Safdel, A. Zarei-Hanzaki, A. Shamsolhodaei, P. Krooß, T. Niendorf, Room temperature superelastic responses of NiTi alloy treated by two distinct thermomechanical processing schemes, Mater. Sci. Eng. A. 684 (2017) 303–311. doi:10.1016/j.msea.2016.12.047.

[3] J. Khalil-Allafi, B. Amin-Ahmadi, M. Zare, Biocompatibility and corrosion behavior of the shape memory NiTi alloy in the physiological environments simulated with body fluids for medical applications, Mater. Sci. Eng. C. 30 (2010) 1112–1117. doi:10.1016/j.msec.2010.06.007.

[4] M. Es-Souni, M. Es-Souni, H. Fischer-Brandies, Assessing the biocompatibility of NiTi shape memory alloys used for medical applications, Anal. Bioanal. Chem. 381 (2005) 557–567. doi:10.1007/s00216-004-2888-3.

[5] M.H. Wu, L.M. Schetky, Industrial Applications for Shape Memory Alloys, Int. Conf. Shape Mem. Superelastic Technolgies. 182 (2000) 171–182. doi:10.1103/PhysRevLett.99.225701.

[6] J.M. Jani, M. Leary, A. Subic, Shape Memory Alloys in Automotive Applications, Appl. Mech. Mater. 663 (2014) 248–253. doi:10.4028/www.scientific.net/AMM.663.248.

[7] J. Mohd Jani, M. Leary, A. Subic, M.A. Gibson, A review of shape memory alloy research, applications and opportunities, Mater. Des. 56 (2014) 1078–1113. doi:10.1016/j.matdes.2013.11.084.

[8] A.R. Pelton, V. Schroeder, M.R. Mitchell, X.Y. Gong, M. Barney, S.W. Robertson, Fatigue and durability of Nitinol stents, J. Mech. Behav. Biomed. Mater. 1 (2008) 153–164. doi:10.1016/j.jmbbm.2007.08.001.

[9] M.H. Elahinia, M. Hashemi, M. Tabesh, S.B. Bhaduri, Manufacturing and

processing of NiTi implants: A review, Prog. Mater. Sci. 57 (2012) 911–946. doi:10.1016/j.pmatsci.2011.11.001.

[10] K. Gall, H. Sehitoglu, Role of texture in tension-compression asymmetry in polycrystalline NiTi, Int. J. Plast. 15 (1999) 69–92. doi:10.1016/S0749-6419(98)00060-6.

[11] F.J. Gil, M. Cenizo, E. Espinar, a. Rodriguez, E. Rúperez, J.M. Manero, NiTi superelastic orthodontic wires with variable stress obtained by ageing treatments, Mater. Lett. 104 (2013) 5–7. doi:10.1016/j.matlet.2013.03.135.

[12] K.K. Kapnisis, D.O. Halwani, B.C. Brott, P.G. Anderson, J.E. Lemons, A.S. Anayiotos, Stent overlapping and geometric curvature influence the structural integrity and surface characteristics of coronary nitinol stents, J. Mech. Behav. Biomed. Mater. 20 (2013) 227–236. doi:10.1016/j.jmbbm.2012.11.006.

[13] D. Kapoor, Nitinol for Medical Applications: A Brief Introduction to the Properties and Processing of Nickel Titanium Shape Memory Alloys and their Use in Stents, Johnson Matthey Technol. Rev. 61 (2017) 66–76. doi:10.1595/205651317X694524.

[14] K. Otsuka, X. Ren, Physical metallurgy of Ti-Ni-based shape memory alloys, Prog. Mater. Sci. 50 (2005) 511–678. doi:10.1016/j.pmatsci.2004.10.001.

[15] C.M. Hwang, C.M. Wayman, Phase transformations in TiNiFe and TiNi alloys, Scr. Mater. 17 (1983) 1345–1350.

[16] J. Frenzel, E.P. George, A. Dlouhy, C. Somsen, M.F.X. Wagner, G. Eggeler, Influence of Ni on martensitic phase transformations in NiTi shape memory alloys, Acta Mater. 58 (2010) 3444–3458. doi:10.1016/j.actamat.2010.02.019.

[17] T. Kurita, H. Matsumoto, H. Abe, Transformation behavior in rolled NiTi, J. Alloys Compd. 381 (2004) 158–161. doi:10.1016/j.jallcom.2004.03.108.

[18] S. Miyazaki, K. Otsuka, C.M. Wayman, The shape memory mechanism associated with the martensitic transformation in TiNi alloys, Acta Metall. 37 (1989) 1885–1890. doi:10.1016/0001-6160(89)90073-4.

[19] K.L.L. Ng, Q.P.P. Sun, Stress-induced phase transformation and detwinning in NiTi polycrystalline shape memory alloy tubes, Mech. Mater. 38 (2006) 41–56. doi:10.1016/j.mechmat.2005.05.008.

[20] J. Ye, R.K. Mishra, A.R. Pelton, A.M. Minor, Direct observation of the NiTi martensitic phase transformation in nanoscale volumes, Acta Mater. 58 (2010) 490–498. doi:10.1016/j.actamat.2009.09.027.

[21] D.C. Lagoudas, Shape memory alloys: Modelling and Engineering Applications, Springer, 2008. doi:10.1007/978-3-319-03188-0_1.

[22] A.P. Stebner, S.C. Vogel, R.D. Noebe, T. A. Sisneros, B. Clausen, D.W. Brown, A. Garg, L.C. Brinson, Micromechanical quantification of elastic, twinning, and slip strain partitioning exhibited by polycrystalline, monoclinic nickel-titanium during large uniaxial deformations measured via in-situ neutron diffraction, J. Mech. Phys. Solids. 61 (2013) 2302–2330. doi:10.1016/j.jmps.2013.05.008.

[23] Y. Soejima, S. Motomura, M. Mitsuhara, T. Inamura, M. Nishida, In situ scanning electron microscopy study of the thermoelastic martensitic transformation in Ti–Ni shape memory alloy, Acta Mater. 103 (2016) 352–360. doi:10.1016/j.actamat.2015.10.017.

[24] H. Sehitoglu, I. Karaman, R. Anderson, X. Zhang, K. Gall, H.J. Maier, Y. Chumlyakov, Compressive response of NiTi single crystals, Acta Mater. 48 (2000) 3311–3326. doi:10.1016/S1359-6454(00)00153-1.

[25] F. Khaleghi, J. Khalil-Allafi, V. Abbasi-Chianeh, S. Noori, Effect of short-time annealing treatment on the superelastic behavior of cold drawn Ni-rich NiTi shape memory wires, J. Alloys Compd. 554 (2013) 32–38. doi:10.1016/j.jallcom.2012.11.183.

[26] M.I. Khan, A. Pequegnat, Y.N. Zhou, Multiple memory shape memory alloys, Adv. Eng. Mater. 15 (2013) 386–393. doi:10.1002/adem.201200246.

[27] M. Elahinia, N. Shayesteh Moghaddam, M. Taheri Andani, A. Amerinatanzi, B.A. Bimber, R.F. Hamilton, Fabrication of NiTi through additive manufacturing: A review, Prog. Mater. Sci. 83 (2016) 630–663. doi:10.1016/j.pmatsci.2016.08.001.

[28] A.M. Ortega, J. Tyber, C.P. Frick, K. Gall, H.J. Maier, Cast NiTi shape-memory alloys, Adv. Eng. Mater. 7 (2005) 492–507. doi:10.1002/adem.200400173.

[29] C. Wang, X.P. Tan, Z. Du, S. Chandra, Z. Sun, C.W.J. Lim, S.B. Tor, C.S. Lim, C.H. Wong, Additive manufacturing of NiTi shape memory alloys using pre-mixed powders, J. Mater. Process. Technol. 271 (2019) 152–161. doi:10.1016/j.jmatprotec.2019.03.025.

[30] T. DebRoy, H.L. Wei, J.S. Zuback, T. Mukherjee, J.W. Elmer, J.O. Milewski, A.M. Beese, A. Wilson-Heid, A. De, W. Zhang, Additive manufacturing of metallic components – Process, structure and properties, Prog. Mater. Sci. 92 (2018) 112–224. doi:10.1016/j.pmatsci.2017.10.001.

[31] J.W. Mwangi, L.T. Nguyen, V.D. Bui, T. Berger, H. Zeidler, A. Schubert, Nitinol manufacturing and micromachining: A review of processes and their suitability in processing medical-grade nitinol, J. Manuf. Process. 38 (2019) 355–369. doi:10.1016/j.jmapro.2019.01.003.

[32] C. Haberland, M. Elahinia, J.M. Walker, S. Saedi, A.S. Turabi, M.T. Andani, Thermomechanical characterization of Ni- rich NiTi fabricated by selective laser melting, Smart Mater. Struct. 25 (2016).

[33] Y. Yang, J.B. Zhan, Z.Z. Sun, H.L. Wang, J.X. Lin, Y.J. Liu, L.C. Zhang, Evolution of functional properties realized by increasing laser scanning speed for the selective laser melting fabricated NiTi alloy, J. Alloys Compd. 804 (2019) 220–229. doi:10.1016/j.jallcom.2019.06.340.

[34] I. Shishkovsky, I. Yadroitsev, I. Smurov, Direct Selective Laser Melting of Nitinol Powder, Phys. Procedia. 39 (2012) 447–454. doi:10.1016/j.phpro.2012.10.060.

[35] M. Speirs, X. Wang, S. Van Baelen, A. Ahadi, S. Dadbakhsh, J.-P. Kruth, J. Van Humbeeck, On the Transformation Behavior of NiTi Shape-Memory Alloy Produced by SLM, Shape Mem. Superelasticity. 2 (2016) 310–316. doi:10.1007/s40830-016-0083-y.

[36] C. Haberland, M. Elahinia, J.M. Walker, H. Meier, J. Frenzel, On the development of high quality NiTi shape memory and pseudoelastic parts by additive

manufacturing, Smart Mater. Struct. 23 (2014). doi:10.1088/0964-1726/23/10/104002.

[37] M.R. Karamooz-Ravari, M. Taheri Andani, M. Kadkhodaei, S. Saedi, H. Karaca, M. Elahinia, Modeling the cyclic shape memory and superelasticity of selective laser melting fabricated NiTi, Int. J. Mech. Sci. 138–139 (2018) 54–61. doi:10.1016/j.ijmecsci.2018.01.034.

[38] N. Shayesteh Moghaddam, A. Jahadakbar, A. Amerinatanzi, M. Elahinia, H. Karaca, D. Dean, Finite Element Simulation and Additive Manufacturing of Stiffness-Matched NiTi Fixation Hardware for Mandibular Reconstruction Surgery, Bioengineering. 3 (2016) 36. doi:10.3390/bioengineering3040036.

[39] C. Haberland, M. Elahinia, J.M. Walker, H. Meier, J. Frenzel, On the development of high quality NiTi shape memory and pseudoelastic parts by additive manufacturing, Smart Mater. Struct. 23 (2014) 104002. doi:10.1088/0964-1726/23/10/104002.

[40] D.J. McGrath, B. O′Brien, M. Bruzzi, P.E. McHugh, Nitinol stent design – understanding axial buckling, J. Mech. Behav. Biomed. Mater. 40 (2014) 252–263. doi:10.1016/j.jmbbm.2014.08.029.

[41] G. Antherieu, N. Connesson, Y. Payan, D. Favier, P. Mozer, NiTi based stent for the treatment of acute urinary retention due to benign prostatic hyperplasia: a preliminary study on NiTi wires and tubes under pure bending, Comput. Methods Biomech. Biomed. Engin. 17 (2014) 190–191. doi:10.1080/10255842.2014.931679.

[42] P. Jamshidi, C. Panwisawas, E. Langi, S.C. Cox, J. Feng, L. Zhao, M.M. Attallah, Development, characterisation, and modelling of processability of nitinol stents using laser powder bed fusion, J. Alloys Compd. 909 (2022) 164681. doi:10.1016/j.jallcom.2022.164681.

[43] X. Li, S. Hao, B. Du, B. Feng, H. Li, P. Qiu, B. Huang, L. Cui, Y. Yang, High-Performance Self-Expanding NiTi Stents Manufactured by Laser Powder Bed Fusion, Met. Mater. Int. (2022). doi:10.1007/s12540-022-01317-2.

[44] S. Maffia, V. Finazzi, F. Berti, F. Migliavacca, L. Petrini, B. Previtali, A.G. Demir, Selective laser melting of NiTi stents with open-cell and variable diameter, Smart Mater. Struct. 30 (2021). doi:10.1088/1361-665X/ac1908.

Chapter 2

New insights on the laser powder bed fusion processing of a NiTi alloy and the role of dynamic restoration mechanisms

Complete Citation:

A. Safdel, M.A. Elbestawi, New Insights on The Laser Powder Bed Fusion Processing of a NiTi Alloy and The Role of Dynamic Restoration Mechanisms, J. Alloys Compd. 885 (2021) 160971. doi: 10.1016/j.jallcom.2021.160971.

Abstract:

NiTi alloys are a remarkable class of materials capable of exhibiting unique behaviors such as shape memory effect and superelasticity. Laser powder bed fusion (LPBF), as one of the most prominent additive manufacturing processes, has been recently used by many researchers to fabricate high-quality NiTi alloys with desired properties. In this research, those findings were exploited to utilize an optimum range of volumetric energy density to produce dense parts and offer new insights into the microstructure and properties of the fabricated parts. Although the development of high residual stresses has been frequently reported, the effects of those stresses on the microstructural evolution of NiTi parts during the process have been rarely discussed. By utilizing finite element and analytical approaches, it was predicted that the driving force for the activation of restoration mechanisms, namely dynamic recovery and recrystallization, is provided at elevated temperatures, and the temperature range in which those mechanisms occur was calculated. Detailed microstructural investigations confirmed the results, revealing columnar grains along the building direction with strong substructures caused by dynamic recovery, in addition to new recrystallized grains at boundaries of the melt pools and scanned tracks. It was concluded that dynamic recovery acts as the dominant restoration mechanism during LPBF of NiTi alloys, affecting both the microstructure and mechanical properties of the final part. Additionally, the peak temperature of the melt pool is a paramount factor that, if increased, results in further progress of the dynamic recovery mechanisms.

Keywords:

NiTi; Laser powder bed fusion; Electron backscattered diffraction; Dynamic recrystallization; Dynamic recovery; Finite element analysis.

2.1 Introduction

Near stochiometric Ni-Ti alloy, also known as Nitinol, is an appealing intermetallic compound due to its shape memory effect (SME) and superelastic (SE) response [1–3]. These unique functional properties are observed due to the occurrence of the thermoelastic martensite transformation, in which transitions occur between the austenite (A) phase, having a symmetrical BCC (B2) crystallographic structure, and the asymmetrical monoclinic (B19′) martensite (M) phase. The small strain-thermal hysteresis of this transformation increases the mobility of the austenite/martensite interface and therefore results in shape recovery of the deformed NiTi alloy during unloading (SE) or heating (SME) [4–6]. In addition to these properties, NiTi alloys exhibit exceptional biocompatibility [7], high ductility [8], corrosion resistance [9], and fatigue resistance [10], which altogether made the material an ideal candidate to fabricate biomedical components. Nowadays, Nitinol is utilized to fabricate various stent structures [11–13], scaffolds [14], orthodontic wires [15], and implants [16].

Due to the strict compositional control requirements during the process, the fabrication of NiTi alloys has always been challenging, and only a few approaches are capable of producing high-quality parts with only simple geometries. The drawbacks of traditional fabrication methods to produce geometrically complex parts and the inability to effectively control the chemical composition and the processing parameters led the researchers to focus on the relatively new additive manufacturing (AM) techniques [17–19]. Among various AM processes, the rapidly advancing laser powder bed fusion (LPBF) process has gained unparalleled attention to produce net-shape NiTi components [19–23]. Based on a computer-aided design (CAD) model, LPBF utilizes a laser to provide enough heat to selectively and sequentially melt a thin layer of powder distributed on a building platform.

This process is carried out in a chamber filled with high purity inert gas to minimize the effects of oxidation and impurity pickup. However, the presence of common defects in the final part, such as porosities, cracks, residual stresses, loss of alloying elements, and surface roughness, presented new challenges which should be comprehensively addressed [24]. Despite various studies to find the optimum processing parameters for LPBF of NiTi, the findings in many areas are still inconclusive, requiring further detailed investigations. In particular, in-depth characterization of the evolved microstructure and the involved mechanisms throughout the process were left out in most studies, leading to an enormous gap in understanding the process-structure-property relationships of a NiTi alloy fabricated by LPBF.

During the LPBF process, the sample endures multiple rapid heating and cooling cycles, which result in the generation of high levels of residual stresses. The development of high residual stresses and the increase in the dislocation density and stored energy in the material was mostly viewed only as an aftermath of the LPBF process, while the consequent microstructural evolution during fabrication, stimulated by the presence of high values of stresses at elevated temperatures has been rarely discussed. Mirkoohi et al. [25] employed an analytical approach and found out that the accumulation of these stresses in addition to high temperatures during LPBF of an Inconel-718 alloy leads to strain hardening or thermal softening. In other words, it was predicted that the required driving force for the activation of dynamic restoration mechanisms is provided during the LPBF process, significantly affecting the microstructural evolution of the fabricated parts. Although the occurrence of dynamic restoration mechanisms has been widely studied for NiTi alloys processed by hot compression [26], hot rolling [27], or hot forging [28], their contribution in defining the

final structure of additively manufactured NiTi components with different processing conditions is yet to be determined.

To that end, this study aimed to design a sophisticated experiment by utilizing the currently available literature regarding additively manufactured NiTi alloys to present new valuable insights on their behavior through the LPBF processes. Primarily, the development of residual stresses in NiTi will be qualitatively assessed using low and high energy densities, and then the printability, loss of Ni content, and transformation behavior will be studied to find the optimum processing window in the present study. Most importantly, as a novel highlight of this research, a combination of analytical and numerical modeling approaches will be exploited to assess the activity of the restoration mechanisms during the LPBF processing of NiTi alloys and evaluate the contribution of dynamic recrystallization (DRX) and dynamic recovery (DRV), on defining the final microstructure and mechanical properties of the fabricated NiTi components.

2.2 Experimental procedures

2.2.1 Initial Powder Feedstock

The NiTi powder was supplied by AP&C (a GE additive company), located in Quebec, Canada. The chemical composition of the as-received powder in Table 2-1 shows that the material is a Ni-rich NiTi alloy, which complies with the F2063 standard criteria.

F2063 is a standard that determines if a material meets the chemical composition required for manufacturing biomedical components [29].

Table 2-1 Chemical analysis of the as-received powder (weight percent)

Element	Ni	C	Co	Cu	Cr	Fe	Nb	N + O	Ti
F2063	54.5-57.0	0.050	0.050	0.010	0.010	0.050	0.025	0.050	Bal.
Measured	55.7	0.034	0.010	0.001	0.004	0.023	<0.002	0.021	Bal.

The morphology of the powder particles was examined by a JEOL-6610 scanning electron microscope (SEM), which according to Figure 2-1(a, b), revealed that the powder particles are mostly in the shape of perfect spheres, and no irregularly shaped particles are apparent in the images. Several plasma jets were focused on a pre-alloyed NiTi wire in an inert atmosphere (Ar) to melt and atomize the wire into powder particles. The cooling rate of the solidified powder particles is slower than other atomization processes (e.g., gas or water atomization), leading to the complete spheroidization of the particles with fewer satellites.

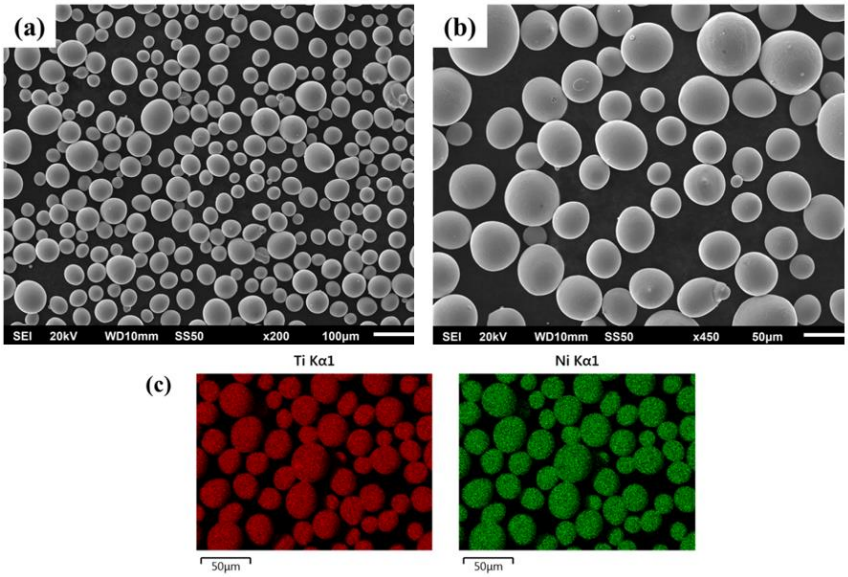

Figure 2-1 (a,b) SEM micrographs of the initial NiTi powder feedstock in different magnifications, showing well-rounded particles with very few satellites. (c) EDS maps of nickel and titanium concentrations in the as-received powder.

According to Figure 2-1(c), the powder feedstock was examined by energy-dispersive X-ray spectroscopy (EDS), and as expected, no evidence of individual Ni or Ti elemental powder particles was apparent in the final batch. This is particularly important since those particles are known to cause inhomogeneities and secondary phases [30].

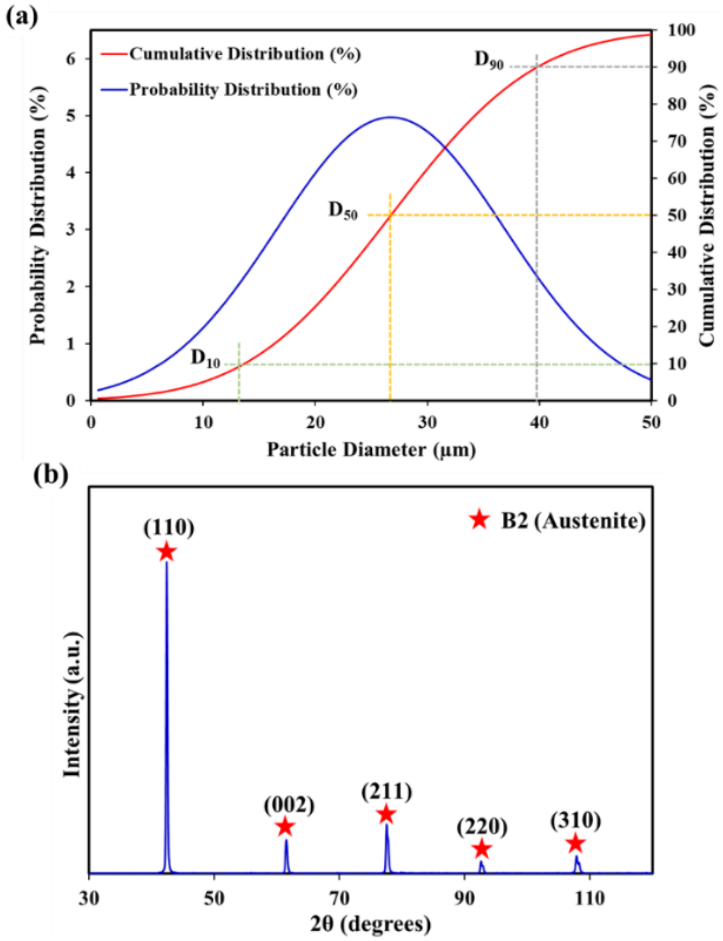

Figure 2-2 (a) probability of size distribution and cumulative distribution, and (b) the XRD pattern of the NiTi powder.

The particle size distribution (PSD) was measured, and the probability and cumulative distribution graphs of the powder particles are shown in Figure 2-2(a). The value of D_x, indicating that *x*% of the particles are smaller or equal to D, the measured particle diameter, was also estimated. Accordingly, D_{10}, D_{50}, and D_{90} were determined to be 14, 27, and

40μm, respectively. Therefore, the diameter of more than 80% of particles is between 14 – 40 μm, signifying that the as-received powder is highly fitting to be used as the feedstock of the LPBF process. X-ray diffraction pattern (Figure 2-2b) of the as-received powder was acquired in the 2θ range of 30-120º using a CuKα (λ=1.5406$\dot{A}$) radiation to analyze the phase fractions. A sharp peak is observed at approximately 42º, which is the characteristic peak of the (110) austenite phase, proving that the material has an austenitic B2 crystallographic structure.

2.2.2 LPBF Processing Parameters

Processing parameters, in particular laser power (P), powder layer thickness (t), scanning speed (υ), and hatch spacing (h), are all imperative and should be thoroughly considered due to their effects on the part's microstructure, physical, and mechanical properties. The volumetric energy density (E – J/mm^3) is calculated by Eq. (2.1) and is a factor that is commonly used in the literature as a criterion to determine the printability of a material [31], although it does not include many other influencing factors (laser spot size, scanning strategy, preheating temperature) [32].

$$E_v = \frac{P}{v.h.t.} \tag{2.1}$$

The LPBF processing parameters used by other researchers to successfully fabricate dense NiTi components are summarized in Table 2-2. Despite the sporadic behavior of the reported data, volumetric energy densities of around 40-126 J/mm^3 have been identified to result in the fabrication of a defect-free dense NiTi component.

Table 2-2 Processing parameters, PSD, and specifications of the equipment previously utilized in LPBF fabrication of NiTi alloys

P (W)	v (mm/s)	h (µm)	t (µm)	E_v (J/mm3)	Scanning Strategy	d_{eff} (µm)	PSD (µm)	Equipment	Reference
250	1100	60	30	126	Alternating x/y	80	25-45	In-house	[22]
77	200	120	50	64.1	NA	52	25-75	SLM solutions	[33]
250	1250	120	30	55.5	Alternating x/y	80	25-75	Phenix systems	[19,34,35]
40	160	75	30	111	Alternating x/y	80	24-45	In-house	[1]
56	133	120	50	70	Linear/circular	55	35-180	SLM solutions	[16,36]
50	100, 160	100	60	52, 83	NA	70	11-38	Phenix systems	[37]
40, 250	160, 1042	75, 80	30	111, 100	NA	80	25-45	In-house	[38]
250	1250	120	30	55.5	NA	80	25-75	Phenix systems	[39]
250	1250	80	30	83.33	Alternating x/y	80	25-75	Phenix Systems	[3]
200	1000	100	50	40	Alternating x/y	40	15-60	SLM Solutions	[40]
250	1000	120	30	69.4	Alternating x/y	NA	25-75	Phenix systems	[18]
60-95	300-850	110	25	45.5-72.7	Meander x/y	NA	24-55	Concept laser	[41]

For this study, test coupons with a dimension of $10 \times 10 \times 5$ mm^3 (L×W×H) were fabricated using an EOS-M280 LPBF machine (EOS, Germany), which is equipped with a fibre laser system capable of delivering a maximum power of 400W. As is indicated in Table 2-2, the mentioned EOS machine has never been used to fabricate NiTi alloys, which is decisive since the parts' final structure can be affected by the utilized equipment, laser spot size, chamber size, recoating blade, and the direction of the gas flow inside the chamber. Accordingly, a wide range of processing parameters (Table 2-3) was nominated, amongst which only those combinations that resulted in volumetric energy density values of 40-

125J/mm^3 were selected for the LPBF process. The layer thickness was maintained to be constant (30µm) for all samples, and an alternating x-y scanning strategy with a stripe width of 5mm, as is demonstrated in Figure 2-3, was employed during the fabrication process.

Table 2-3 Selected processing parameters to fabricate the as-received NiTi alloy powder

P (W)	v (mm/s)	h (mm)	t (mm)	E_v (J/mm^3)
50-100-150-200-250	250-500-750-1000-1250	0.08-0.10-0.12	0.03	40-125

Each part with the same processing parameters was printed three times to ensure process stability and repeatability, and a NiTi building platform, supplied by Fort Wayne Metals (IN, USA), was used for the fabrication of the parts. The building platform was preheated to 200ºC in order to decrease the thermal gradient and limit the consequent development of high residual stresses at the printing interface. The chamber was primarily pre-flooded with high purity Argon gas, and then a constant gas flow was maintained during the process to prevent oxidation and impurity pickup.

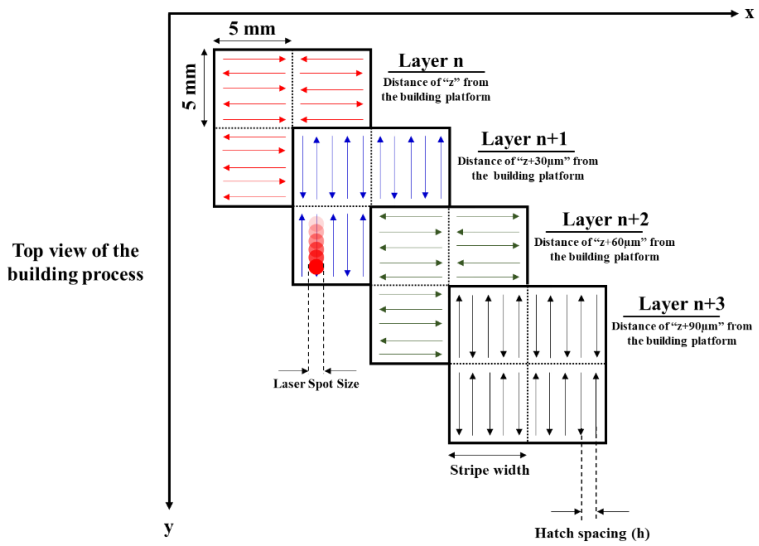

Figure 2-3 Top view of the laser movement during the LPBF process, schematically demonstrating the scanning strategy and the other important processing parameters.

All fabricated samples were then cut from the building platform using electro-discharge machining (EDM). According to Chen et al. [42], the fabricated parts' microstructure and properties are not identical at different heights relative to the building platform. Therefore, for consistency, the middle section of the fabricated specimens was considered as the main area of interest, and samples were extracted accordingly via EDM for further characterizations. It is worth mentioning that no subsequent heat treatments were applied prior to further analysis. For brevity and clarity, samples were labeled according to the utilized processing parameters, and the coding reference is represented in Table 2-4.

Table 2-4 Processing parameters that were used to fabricate each labeled sample

Label	P (w)	v (mm/s)	h (mm)	Label	P (w)	v (mm/s)	h (mm)	Label	P (w)	v (mm/s)	h (mm)
A1	100	250	0.12	B1	200	750	0.08	C1	150	500	0.08
A2	150	500	0.1	B2	250	750	0.12	C2	200	500	0.12
A3	150	750	0.08	B3	200	750	0.1	C3	250	750	0.1
A4	100	500	0.1	B4	250	1000	0.1	C4	50	250	0.08
A5	150	750	0.1	B5	150	500	0.12	C5	250	1000	0.08
A6	150	750	0.12	B6	200	1250	0.08	C6	200	1000	0.08
A7	100	500	0.12	B7	50	250	0.1	C7	100	500	0.08
A8	150	1250	0.08	B8	100	750	0.08	C8	250	1000	0.12
A9	250	1250	0.12	B9	200	1000	0.1	C9	250	1250	0.08
A10	100	750	0.1	B10	200	1000	0.12	C10	250	1250	0.1
A11	150	1000	0.1	B11	150	1000	0.08	C11	200	750	0.12
A12	200	1250	0.12	B12	200	1250	0.1	C12	50	250	0.12

2.2.3 Characterization Methods

According to the Archimedes principle, the relative density of the fabricated specimens was measured using a high precision balance with an accuracy of ±0.01 mg. The acquired data were then compared to the measurements of metallographic approaches obtained from

the commercial ImageJ software. For optical microscopy observations, samples were ground by SiC abrasive papers (grit sizes of 600, 800.1200, 2400, and 4000), and then they were further polished by 9, 6, 3, and 1μm diamond pastes to obtain a mirror-like surface finish. A Keyence VHX digital microscope was used to investigate the state of the defects, pores, and cracks in each sample.

The nickel content of the samples was estimated by a Varian Inc. Vista-Pro inductively coupled plasma optical emission spectrometer (ICP-OES), in which ~0.1gr samples were digested in a solution of 1:1:1 hydrofluoric acid (HF), nitric acid (HNO3), and hydrochloric acid (HCl). The solution was diluted with distilled water with a ratio of 1:20 before measurements, and each solution was analyzed five times for higher precision. Transformation temperatures and the behavior of the martensitic transformation were examined by Q2000 (TA instrument) differential scanning calorimetry (DSC) in accordance with the ASTM F2004 standard [43]. Each sample was first heated up to 150ºC, kept at that temperature for 5min to achieve thermal equilibrium, and was subsequently cooled down to -70ºC, held for 5 min, and heated up to 150ºC with the same rate. The rate of 10ºC/min was applied for both heating and cooling cycles.

Microstructural characterization of samples was carried out using a JEOL JSM-7000F SEM, equipped with a Schottky field emission gun (FEG) and Nordlys II electron backscatter diffraction (EBSD) camera, operating at an acceleration voltage of 20 kV. Due to the sensitivity of EBSD to surface preparation in the acquisition of high-quality patterns, samples were further polished by a diamond paste of 0.5 and 0.1μm sizes and a colloidal silica suspension. Post-processing of the acquired data was conducted in Aztec and Channel 5 software. EBSD orientation maps or inverse pole figure (IPF) color maps were utilized to investigate the samples' microstructure. In these maps, the crystallographic

direction of the scanned grains across an area of interest is plotted based on different colors and a reference direction (e.g., building direction). These colors and the corresponding crystal orientations in the IPF maps can be interpreted by the color key on the stereographic triangle. Lastly, the Vickers hardness values (HV) of the samples were measured using a Clemex automatic micro-hardness tester, in which a load of 300gf was applied for each indentation.

2.3 Finite Element Modelling

The cantilever design, which was also utilized by other studies [44–47], was employed to model the deflection behavior of the material, and the geometry of the part is illustrated in Figure 2-4(a). The commercial ABAQUS2019 software was used to model the process in a sequential manner, in which transient heat transfer equations are solved to predict the temperature fluctuations of the part. Then the development of residual stresses is measured by applying the acquired thermal history and temperature fluctuations. The laser beam movement, which acts as the primary heat source, was converted into a g-code by the open-source ReplicatorG software, and the AM-Modeler plugin was utilized to input the resulting code in the model. The extracted g-code contains data about the time and coordinates that the laser beam is scanning the part. In other words, the scanning speed, hatch spacing, layer thickness, and scanning strategy are all defined by this parameter. To save computational time without sacrificing the model's accuracy, the effective laser diameter was considered in the model, assuming that the laser has a uniform power distribution on the powder bed.

As is demonstrated in Figure 2-4(a), linear hexahedron elements were used to mesh the part, and the elements in single layers were added sequentially by considering a dwell time

of 10s to resemble the recoating procedure. Element activation approach was utilized, in which stress-free elements at the melting temperature are introduced to the system, and the fluctuations in temperature and thermal straining are calculated through the numerous subsequent heating and cooling stages. To mimic the actual process, heat radiation and heat convection of the part and the surrounding area were also implemented in the model. More details regarding the modeling methodology and the governing equations are given by Narvan et al. [46] and Li et al. [48]. Ultimately, the deflection of the cantilever is utilized to qualitatively demonstrate the effect of the developed residual stresses, which can be measured by adding a cutting step to the printed part in the model. As is depicted in Figure 2-4(b), by cutting the side supports, the cantilever is deflected due to the occurrence of stress relaxation.

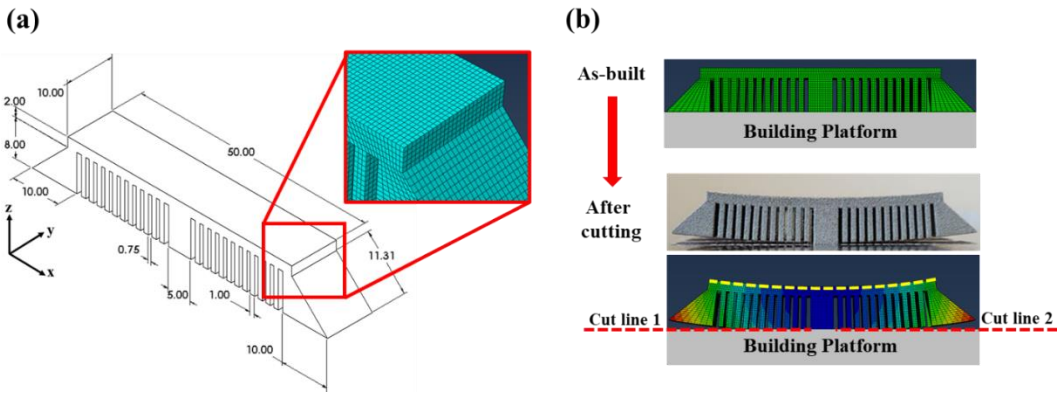

Figure 2-4 (a) cantilever dimensions (in mm) and a brief view of the meshing approach, and (b) the view of the part before and after cutting the side supports.

Thermophysical properties of the NiTi alloy used for the numerical simulations in this section and the analytical predictions in section 4.5 are represented in Table 2-5. These values were either extracted from the literature or were obtained by simulations based on the TCNI8.0 database in ThermoCalc software. For the sake of brevity and comparison, only B8 and C1 conditions were modeled, in which low and high volumetric energy

densities of 56 and 125J/mm^3 were implemented. In order to investigate the reliability of the model, the same cantilever geometry was fabricated, and the deflection of the top surface after cutting the side supports was measured by using a Mitutoyo CRYSTA-Apex S544 coordinate measuring machine (CMM) having an accuracy of 0.1μm.

Table 2-5 The most important room temperature thermophysical properties of the processed austenitic NiTi alloy

Property (symbol)	Dimension	Value	Reference
Laser absorption efficiency (A)	-	0.35	[49]
Melting temperature (T_m)	K	1584	[50]
Boiling temperature (T_b)	K	3560	ThermoCalc
Thermal conductivity (K)	$W/m.K$	18	[51]
Thermal diffusivity (α)	m^2/s	3.87×10^{-6}	[52]
Young's modulus (E)	GPa	83	[53]
Coefficient of thermal expansion (CTE)	$1/K$	11×10^{-6}	[51]
Poisson's ratio (ν)	-	0.3	[54]
Volumetric enthalpy (h_s)	J/m^3	1.87×10^{9}	ThermoCalc
Laser spot size (D)	m	10^{-4}	[55]
Emissivity	-	0.5	[53]

2.4 Results and Discussion

2.4.1 Delamination and the effects of residual stresses

The first few layers during the LPBF process are of utmost importance due to the significantly high thermal gradients and the developed residual stress. The accumulation of these stresses can lead to warpage and flaking of the thin deposited material [55–59], which results in recoater impact and process discontinuity. The mechanism of this behavior

is depicted in Figure 2-5. When the laser beam scans a fresh layer (Figure 2-5a), a steep temperature is applied, and the previously solidified layers bend due to the thermal expansion. This expansion is much higher in solidified layers closest to the surface, causing the material to lean toward the laser beam (Figure 2-5a). When the laser moves away and the material cools down, shrinkage occurs for the scanned layer leading to a contraction in the top layers. As a result, a concave shape toward the laser beam is formed (Figure 2-5c). If this delamination exceeds a critical distance of more than one layer thickness, the recoater blade will hit the solidified material, leading to process discontinuity and damaging both the blade and the fabricated part. Since the EOS machine uses a rigid ceramic blade recoater, even the slightest delamination ($> 30\mu m$) prevents the progress, which was an issue mainly observed when volumetric energy density values exceeded 83.33J/mm^3. In order to mitigate this problem, a carbon fiber brush recoater was installed on the EOS machine, which permits a higher degree of freedom and ensures process continuity, even when the few layers are experiencing minor delamination. The other benefits of utilizing a soft recoater have also been recently reported elsewhere [60].

Consequently, all parts were successfully fabricated by utilizing the mentioned range of processing parameters. However, successful fabrication of parts is not the goal of the process, and fabricated parts should be optimized in terms of the developed residual stresses, microstructure, and properties.

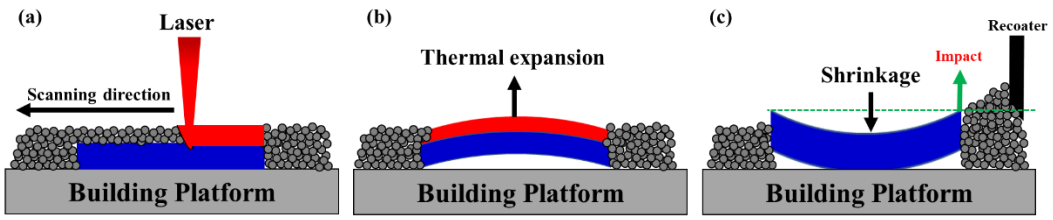

Figure 2-5 The occurrence of flaking behavior and delamination in LPBF processing of NiTi alloys.

The development of residual stresses in low and high levels of volumetric energy densities (56 and 125J/mm^3) was compared according to the conducted finite element analysis (FEA) and measurement of the cantilever's deflection. The results are demonstrated in Figure 2-6(a), along with comparing the deflection values for other materials obtained from the indicated studies. The volumetric energy densities that are displayed in the figure for different materials were identified as optimized E_v values. Direct comparison of the deflection values is not possible since different processing parameters were utilized for the simulations, and the materials' properties, particularly, coefficient of thermal expansions (CTEs) and thermal diffusivities (α) are completely different. Nonetheless, it is apparent that the deflection of the NiTi cantilever, when a lower energy density is utilized, is in the range of other materials when optimum processing conditions are used. However, a significantly higher deflection is evident when a high value of volumetric energy density was employed, suggesting a higher level of developed residual stresses. Consequently, increasing the volumetric energy density leads to the development of higher residual stresses, which can cause significant deflection in the case of the NiTi cantilever beam, and delamination of parts during the process. More importantly, the plastic deformation and deflection of the cantilever beam after LPBF signifies the formation of high values of residual stresses, which is not only imperative with respect to the feasibility of the process but also is paramount in considering its effects on the microstructure and the mechanical properties of the final parts.

Moreover, comparing the simulated deflection values with the experimentally measured ones in Figure 2-6(b) denotes that the model is highly reliable, although the residual stresses, specifically at higher E_v values, are slightly overestimated. This difference, on the one hand, can be attributed to the formation of unstable keyholes and spherical porosities,

which reduces the material constraints during the LPBF process, and on the other hand, is related to the occurrence of restoration mechanisms as a consequence of the presence of high levels of stresses at elevated temperatures. Both of these mechanisms will be further examined in sections 2.4.2 and 2.4.6 of the thesis, respectively.

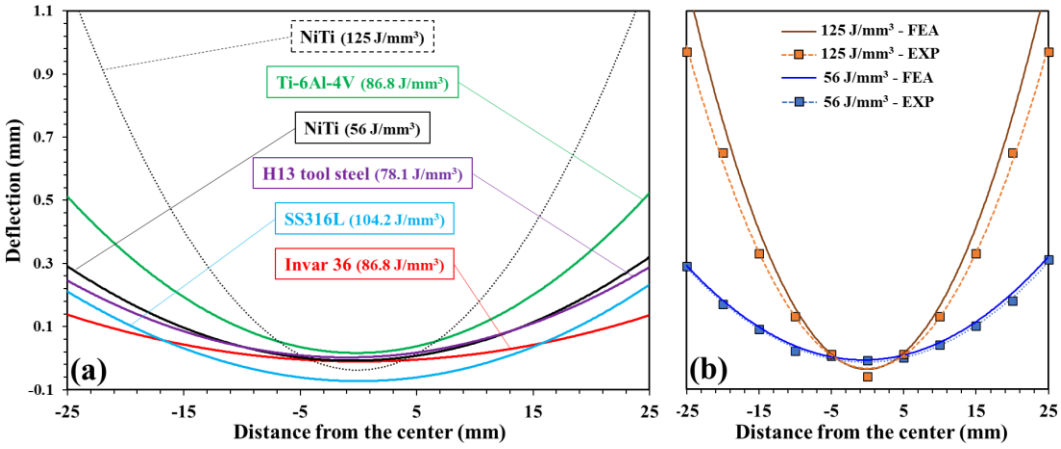

Figure 2-6 (a) the deflection values of the NiTi cantilever obtained from FEA by employing two different volumetric energy density levels (56 and 125J/mm^3) and the results of other studies for Ti-6Al-4V [45], H13 tool steel [46], stainless steel 316L [44], Invar 36 [47], and (b) the comparison between the simulated and experimentally measured deflection of NiTi beams.

2.4.2 Density and the level of porosities

Table 2-6 represents the measured relative density of each fabricated sample, and since the measurement was conducted by both Archimedes and metallographic approaches, the standard deviation (σ) is also pointed out. As is apparent, most samples were highly dense, having relative densities of 98% or higher. However, the variations in relative density need further explanation in view of the utilized processing parameters.

Table 2-6 The values of the relative density and standard deviation (σ) measured by Archimedes and metallographic approaches.

Label	Relative density	σ	Label	Relative density	σ	Label	Relative density	σ
A1	98.57	0.17	B1	99.00	0.51	C1	95.87	1.57
A2	96.17	1.28	B2	99.34	0.46	C2	91.73	1.58
A3	99.68	0.11	B3	99.59	0.04	C3	98.37	0.32
A4	99.89	0.04	B4	99.17	0.30	C4	99.20	0.39
A5	99.65	0.01	B5	97.12	0.31	C5	99.63	0.15
A6	99.44	0.33	B6	99.88	0.02	C6	99.83	0.11
A7	99.90	0.04	B7	99.64	0.26	C7	99.88	0.06
A8	99.95	0.05	B8	99.95	0.05	C8	98.68	0.25
A9	99.88	0.06	B9	99.82	0.09	C9	99.73	0.23
A10	99.73	0.17	B10	99.76	0.12	C10	99.81	0.11
A11	99.84	0.12	B11	99.90	0.03	C11	99.19	0.48
A12	99.78	0.06	B12	99.93	0.03	C12	99.59	0.07

Linear heat input in additive manufacturing is defined as the ratio of the laser power to the laser scanning speed $\left({}^{P}/_{v}\right)$. This ratio, which is also recognized as linear energy density (E_L), governs the instantaneous interactions of the laser beam with the powder bed and can be utilized to predict the appearance of defects. It was observed that high values of linear heat input could lead to a significant temperature increase to the point where keyhole mode would be the dominant deposition mode. Deposition in keyhole mode during LPBF of NiTi alloys is of utmost importance because of the high vapor pressure of the Ni element in these alloys. Due to the high speed of the LPBF process, keyhole deposition cannot be effectively controlled, causing keyholes to destabilize and rapidly form and collapse. As a result, nearly spherical porosities are formed, consisting of entrapped vaporized material [24].

Figure 2-7 demonstrates the correlation between the relative density of the processed materials and the linear heat input in hatch spacings of 80, 100, and 120µm. Each graph has been divided into three zones according to the observed microstructure. Red trendlines

were superimposed on each curve to show the variations of the data clearly. In zone (I), the lowest heat inputs were used, which is the zone that showed the highest relative densities. It should be mentioned that lack of fusion defects and irregular porosities were not observed for any of the fabricated samples, indicating that the utilized processing parameters are able to fully melt the material. Zone (II) is an intermediate zone where keyhole porosities are observed for linear heat inputs higher than 0.2 J/mm. In zone (III), further increasing the P/v ratio, more keyhole porosities are noticed, resulting in lower relative densities. In Figure 2-7(b, c), an unexpected increase in relative density was observed at a linear heat input of 0.33 J/mm. The red dots in these figures represent sample C3 and B2, respectively, in which the laser power was 250W, and the scanning speed was 750mm/s. This high-powered laser creates a larger melt pool, and the utilized lower scanning speed increases the chance of the evaporated metals (Ni) to exit the pool through its surface. Although keyholes are still formed, they are more stabilized, and therefore fewer porosities are left behind after each scan.

Hence, to obtain a highly dense NiTi alloy without keyhole porosities and to prevent the loss of alloying elements, the linear heat input must be less than 0.2J/mm. The highest relative densities (~99.95%) were recorded for samples B8 and A8, and to the best of the authors' knowledge, this is the highest density level acquired for a NiTi part fabricated via LPBF. The hatch spacing for both B8 and A8 was 80μm, and the laser power and scanning speed were 150W and 1250mm/s for A8, while they were 100W and 750mm/s for B8.

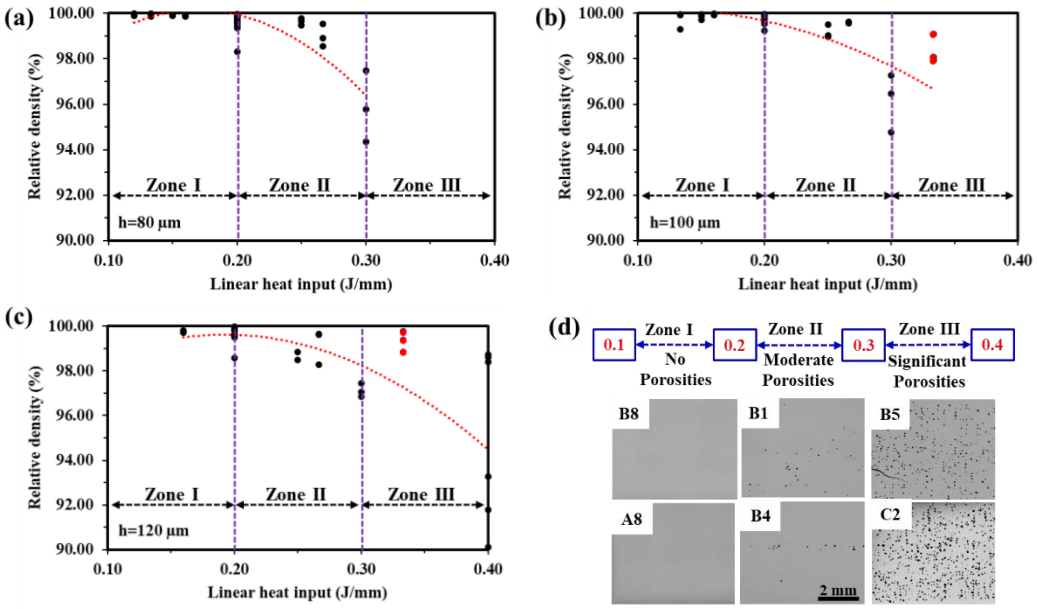

Figure 2-7 Variations in the measured relative densities of the parts fabricated by different linear heat inputs and hatch spacings of (a) 80, (b) 100, (c) 120µm; and (d) optical micrographs of some of the selected parts showing no keyholes, moderate keyholes, and significant keyholes in zones I, II, and III, respectively.

2.4.3 Loss of alloying elements

The severe effect of keyhole deposition in LPBF is not limited to the deterioration of relative density. The involved evaporation contributes to the loss of alloying elements during the process, changing the NiTi alloy's chemical composition and rendering the part useless for biomedical applications. In other terms, the variations in Ni content due to its high vapor pressure can affect the thermoelastic martensite transformation behavior, impacting the SME and SE of the material. The nickel content (wt.%), measured by ICP-OES, is depicted in Figure 2-8 for all fabricated samples as a function of linear heat input. Conventional elemental characterization methods, such as energy dispersive spectroscopy and X-ray fluorescence, lack the required accuracy to estimate the Ni-content, while ICP-OES can precisely measure down to PPM levels. The fluctuations in the Ni content of the matrix as a function of linear heat input for hatch spacings of 80, 100, and 120µm in Figure

2-8 demonstrate that higher heat inputs resulted in lower nickel contents. As mentioned in the previous section, keyhole formation causes Ni evaporation, and the higher the peak temperature (i.e., the heat input), the higher the possibility of evaporation. A very slight decline in nickel content is yet visible for samples that did not exhibit any signs of keyholes and spherical porosities (Zone I). This minor drop (~0.1wt%) in NiTi alloys is related to the involvement of conductive vaporization mechanisms in which the alloying elements vaporize from the surface of the melt pool prior to reaching a steady state in which further loss is prevented. Consequently, both conduction and keyhole modes during the LPBF can effectively contribute to the loss of alloying elements. However, this loss is negligible for conductive vaporization, while it can be highly significant when keyhole mode is involved [42,61].

Moreover, a noteworthy trend starts to appear by observing the variations in Ni content in different hatch spacings. Red trendlines with their corresponding equations are superimposed on the graphs. As is evident from Figure 2-8(a), the slope of the trendline is much higher when a hatch spacing of 80µm was utilized for fabrication. By increasing the hatch distance to 100µm, according to Figure 2-8(b), the slope is decreased, and ultimately when the hatch distance of 120µm was employed (Figure 2-8c), the lowest slope was recorded. Lower hatch spacings during the LPBF result in higher volumetric energy densities, which cause a significant temperature increase in the laser path and its neighboring tracks. The effective laser spot size in the utilized EOS machine is 100µm, which denotes that in hatch spacings of 80µm, the overlapping of laser tracks leads to further temperature increase and higher degrees of evaporation. However, during the fabrication of parts with a hatch distance of 120µm, the temperature increase in neighboring tracks is considerably lower, resulting in a gentle slope according to the

represented figure. The overall trend and the changes in the nickel content are also shown in Figure 2-8(d), confirming that the increase in volumetric energy density causes a depletion in the nickel content of the matrix.

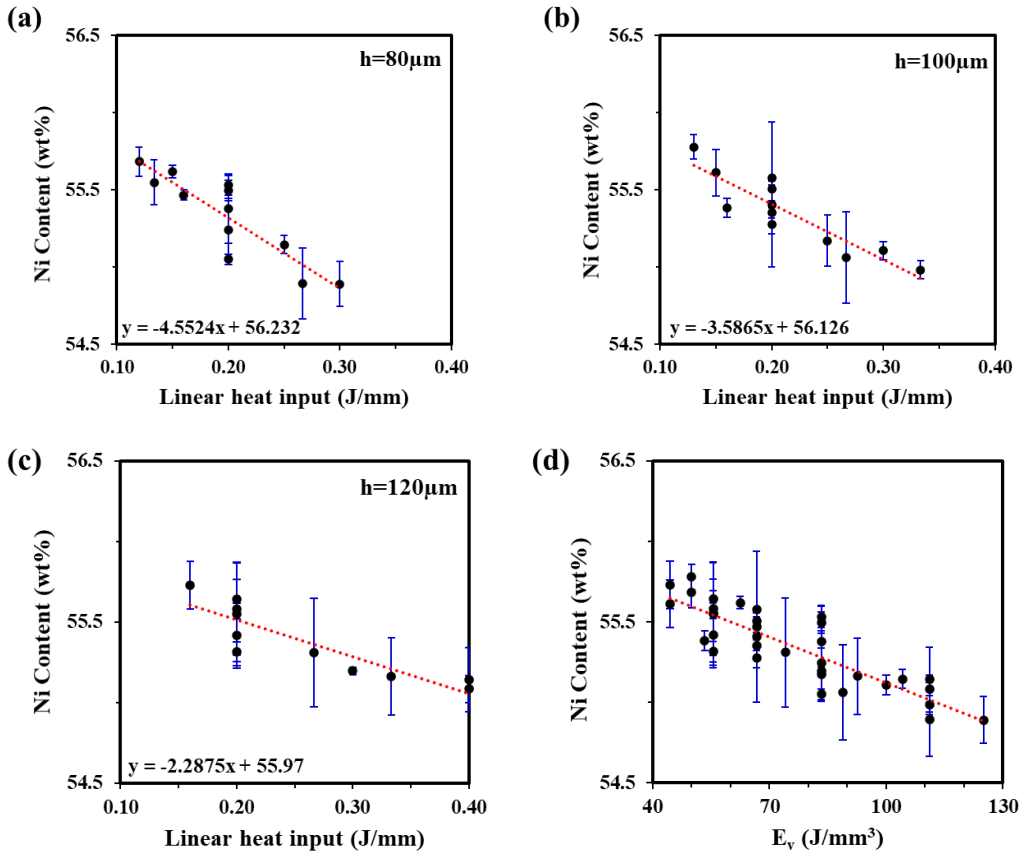

Figure 2-8 (a-c) the effect of the linear heat input on nickel evaporation during the LPBF processing of the NiTi alloy at different hatch spacings, and (d) the overall trend in nickel content as a function of volumetric energy density.

2.4.4 Microstructure and the role of restoration mechanisms

Amongst all the samples processed by a wide range of processing parameters, B8 and A8 were selected for further microstructural investigations since no defects were apparent in their structure, and the highest density values along with the lowest Ni drop were achieved for these samples. According to Figure 2-9, both samples possess columnar structures, in

which the grains are elongated in a direction parallel to the building direction. A strong texture along <001>, parallel to the BD, is also evident from this figure. In epitaxial solidification, when a laser beam scans a new layer of powder, not only the heat input of the laser beam causes the powder particles on the surface of the bed to melt, but also it provides enough heat for the previously consolidated layer to get partially melted again. To this end, columnar grains tend to grow in the BD direction, which is also the direction that offers the highest heat flow, resulting in the illustrated stretched grains.

Detailed assessment of Figure 2-9 also reveals the presence of a strong substructure within each grain, noticed by the slight color deviations in the IPFs maps and the formation of very fine grains at particular locations (indicated by dashed circles), suggesting that other mechanisms should be involved as well. To find out, LPBF should be fundamentally scrutinized in terms of both the temperature fluctuations and the stresses evolution during fabrication.

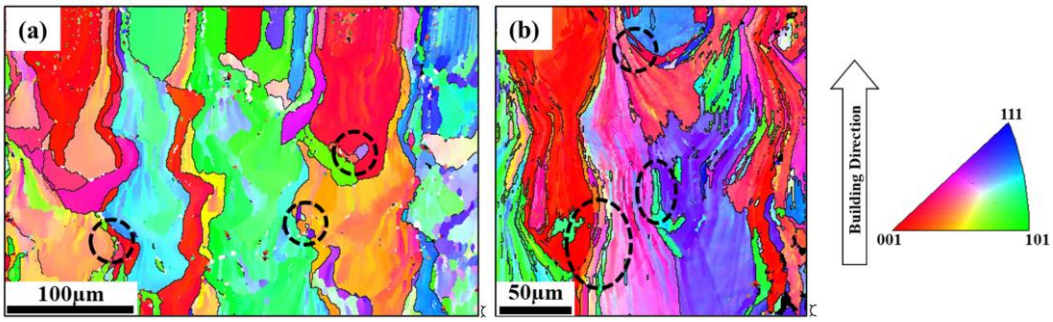

Figure 2-9 IPF maps of (a) sample B8 and (b) sample A8, in a direction parallel to the BD.

As was mentioned earlier, the imposed numerous rapid heating and cooling stages during the LPBF and the solidified material's acting constraints result in the development of high values of residual stresses. According to the previously discussed FEA and the deflection

values of the cantilever beam, the level of developed stresses is increased when higher volumetric energy densities and, therefore, higher heat gradients are involved. However, the development of stresses and the subsequent increase in dislocation density should not only be viewed as an after-effect of the LPBF process, and the consequences of the presence of those stresses on the microstructural evolution of samples during high-temperature fabrication should also be examined. To put it simply, in addition to the high temperature of the process, the material is enduring high mechanical loads, which together are the main characteristics of a typical thermomechanical process. Thermomechanical processes are of utmost importance since they stimulate the occurrence of the restoration mechanisms, in which the microstructure of the material is significantly evolved. The possible outcomes of microstructure evolution during the activation of restoration mechanisms are schematically drawn in Figure 2-10. As is depicted, restoration mechanisms are divided into two main categories, namely dynamic recovery (DRV) and dynamic recrystallization (DRX), from which the latter can occur either in a continuous (cDRX) or discontinuous (dDRX) manner.

In DRV, dislocations can glide, climb, and cross-slip, which results in the annihilation of some dislocations and lower stored energy in the material. Also, the subsequent rearrangement of the remaining dislocations contributes to the formation of low angle grain boundaries (LAGB) and equiaxed subgrains (shown by blue lines). On the other hand, through DRX, new grains with high angle grain boundaries (HAGB) can nucleate and grow at the boundaries of the preexisting growing grains (dDRX), or HAGBs are formed by the rotation and continuous increase in the misorientation angle of the LAGBs (cDRX). As is illustrated in Figure 2-10, full advancement of DRX can lead to a fully recrystallized structure with low dislocation density and refined equiaxed grains. The occurrence of DRX

and the refinement of grains in LPBF of 316L stainless steel was recently observed in a study by Eskandari et al. [62].

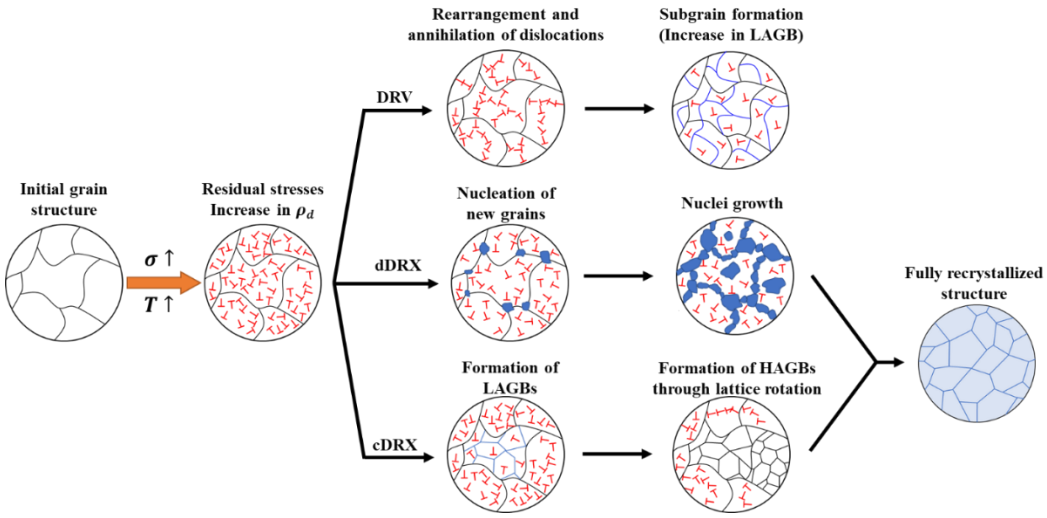

Figure 2-10 Schematic view of the dynamic restoration mechanisms and the microstructural evolution through each mechanism.

2.4.5 Predicting the activity of restoration mechanisms in LPBF of NiTi alloys

For further examinations, classical constitutive relationships and analytical approaches were utilized to predict the occurrence of DRX and DRV during LPBF processing of NiTi alloys. Since dynamic restoration mechanisms are thermally activated, temperature plays a critical role, although other factors such as stress levels, strains, and strain rates are also influential. The classical Zener-Hollomon approach is most commonly used to predict the occurrence of the mentioned restoration mechanisms [62,63], and the Zener-Hollomon parameter (Z) is calculated via Eq. (2.2):

$$Z = \dot{\varepsilon} \exp\left\{\frac{Q}{RT}\right\} \tag{2.2}$$

here $\dot{\varepsilon}$ is the strain rate (s^{-1}), Q is the activation energy (J/mol), R is the universal gas constant (8.314 J/mol.K), and T is the temperature of the process (K). The next step toward the calculation of the Z value is to measure the strain rate of the process, which is caused by the thermal fluctuations in the powder bed, imposed by a rapidly moving laser beam. In addition to the processing parameters, the amount of heat dissipation during fabrication is also affected by the temperature and the thermal conductivity of the material. The following equation is used to estimate the strain rate in the LPBF process [64]:

$$\dot{\varepsilon} = \frac{KT_{peak}v}{P} \tag{2.3}$$

where K is the thermal conductivity of the material (W/m.k), T_{peak} is the maximum temperature of the melt pool (K), P is the laser power (W), and v is the scanning speed (mm/s). The strain rate was estimated to be 437 and $564s^{-1}$, for B8 and A8, respectively. The peak temperature of the melt pool is proportional to the normalized volumetric enthalpy (H_n) and the boiling temperature of the material. The value of H_n is equal to $\Delta H/h_s$, where ΔH is the specific enthalpy, and h_s is the enthalpy of the material at the melting temperature. According to King et al. [65], the value of H_n in LPBF is correlated to the thermophysical properties of the material and the processing parameters via the following equation:

$$H_n = \frac{AP}{h_s\sqrt{\pi\alpha v D^3}} \tag{2.4}$$

here A indicates the laser absorptivity, α is the thermal diffusivity (m^2/s), and D is the laser spot size. Eq. (2.4) is used to measure the maximum temperature of the melt pool, which results in a peak temperature between the melting point and boiling temperature of the material [65,66].

$$T_{peak} = \frac{H_n . T_b}{H_n^{max}} \tag{2.5}$$

where H_n represents the heat input of the process and H_n^{max} is the maximum normalized enthalpy value in which evaporation and keyhole formation does not occur, and its value can be estimated by using the following equation [62,65]:

$$H_n^{max} = \frac{\pi . T_b}{T_m} \tag{2.6}$$

It is worth mentioning that these equations are applicable only for those processing parameters that did not result in the keyhole formation. In other words, according to Eq. (2.5), the peak temperature is scaled to a temperature between the melting temperature and the boiling point of the material. Calculations based on the equations given in this section resulted in a peak temperature of 2191 and 2546K for samples B8 and A8, respectively.

To further confirm the accuracy of the utilized analytical model, a finite element simulation was conducted using the commercial ABAQUS software, in which the temperature of a selected spot at the center of the samples, when a high-powered laser beam scans it during the LPBF process was simulated. The results revealed a maximum temperature of 2178K for B8 and 2494K for A8, confirming the high accuracy of the mentioned analytical models. For brevity, only the variation in temperature for a single nod during the LPBF processing of sample A8 is illustrated in Figure 2-11(a). As is evident, at multiple points, the maximum temperature of the material exceeds the alloy's melting temperature. On the one hand, when the laser is moving to the neighboring tracks, the temperature significantly increases due to the overlapping of the scanning tracks, and on the other hand, when upper layers are scanned, the abrupt temperature increase causes a significant rise in the

temperature of the lower layers. This behavior was also reported by other researchers, who simulated the temperature of the molten pool during the LPBF processing of different materials [48,67].

Based on these calculations and the simulation results, the Zener-Hollomon parameter was measured, and the value of Ln(Z) as a function of temperature is displayed in Figure 2-11(b). Earlier, it was stated that the Z-value is a critical factor in determining the occurrence of the restoration mechanisms. Morakabati et al. [68] noted that the optimum Z-value for the activation of restoration mechanisms in NiTi alloys is between 10^9 to 10^{13} ($\ln(Z) \cong 21 - 30$), while no evidence of dynamic restoration processes was observed in Z-values higher than 10^{14} ($\ln(Z) \cong 33$).

Identification of the dominant restoration mechanism in NiTi alloys is a controversial topic, and while some researchers believe that DRX is the dominant restoration mechanism [69,70], others [26,68] argue that DRV plays a prominent role in defining the structure of the material. Stacking fault energy (SFE), as an intrinsic property of a material, is an imperative factor that governs the dislocations' movements and the consequent occurrence of DRX or DRV. As a rule, higher SFE and Z values result in DRV, whereas DRX occurs at lower SFE and Z values. A series of simulations in a study based on the molecular dynamics (MD) approach [71] revealed that the SFE of an austenitic NiTi alloy is very high (>142 mJ/m^2), signifying that the probability of the occurrence of DRV is expected to be higher than DRX.

Assuming DRV as the main restoration mechanism, the ln(Z) range in which the occurrence of restoration mechanisms has been previously reported is plotted in Figure 2-11(b) as a function of the temperature. Accordingly, the graph is divided into three zones:

(I) in this zone, DRV is believed to be the main restoration mechanism, although partial DRX might occur as well, (II) the lower temperatures and higher Z-values limit the occurrence of dynamic restoration, resulting in partial DRV as the only acting mechanism for high SFE NiTi alloys, and zone (III), where extremely high Z-values ($>10^{14}$) are obtained, which indicates no active dynamic restoration. However, in this zone, grains still have a chance to grow in the presence of higher temperatures.

Since the ln(Z) was plotted as a function of temperature, the calculations contribute to finding the temperature range in which the dynamic restoration mechanism might be activated during the LPBF process. Hence, the temperature range of the occurrence of DRV or DRX, corresponding to zone (I) and (II) in Figure 2-11(b), is superimposed on Figure 2-11(a). Evidently, at many points during manufacturing, the required conditions for the occurrence of restoration mechanisms are met, concluding that samples must have experienced recovery or recrystallization during the LPBF process. However, this prediction should be verified by further microstructural examinations.

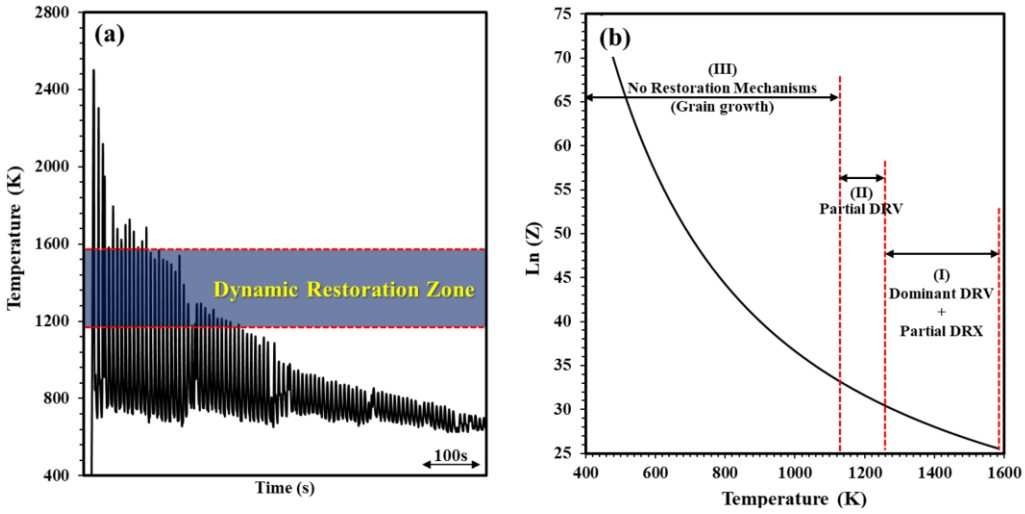

Figure 2-11 Temperature fluctuations during LPBF of sample A8 at a selected location, and (b) the variations in the Zener-Hollomon value as a function of temperature.

2.4.6 Verifying the occurrence of DRV and DRX

To verify the previous predictions and assess the involvement of restoration mechanisms, EBSD recrystallization fraction maps were acquired for B8 and A8 samples. Channel 5 software was utilized to post-process the EBSD data, which is capable of revealing the areas that are affected by recrystallization or recovery. Each grain is primarily identified based on a given value for the misorientation angle (15º). Subsequently, the average misorientation angle between each scanned point within the grain is measured. This value is then compared to the subgrains' misorientation angle (2º), and if lower, that grain is classified as recrystallized. If the value is lower than 2º, but the misorientation angle between any subgrains is higher than 2º, the selected grain is categorized as substructured. Finally, average values higher than 2º indicates a deformed grain. According to this methodology, the restoration maps showing recrystallized, substructured, and deformed grains for samples B8 and A8 are depicted in Figure 2-12.

The recrystallization and recovery fraction maps in Figure 2-12(a, b) reveal that most areas of the samples consist of substructured grains (indicated by the yellow color), which is an indication of recovery mechanisms. Therefore, it can be confirmed that dynamic restoration mechanisms played a significant role during the LPBF processing of NiTi alloys to define the final microstructure. However, blue areas in these figures reveal that DRV was not the only complicit mechanism, and partial DRX is apparent in some particular regions where new equiaxed grains are formed. It was mentioned that the nucleation and growth of new grains is an indication of the dDRX process, and usually, new grains form at triple junctions or the boundaries of the preexisting grains. As is represented in Figure 2-12(a, b), new dDRX grains are not only formed at the preexisting boundaries of other grains but also are preferably formed at the boundaries of the melt pools and the overlapped scanned tracks.

A closer inspection of grain boundary maps in Figure 2-12(c, d) signifies that the state of grain boundaries is different for B8 and A8. For A8, as opposed to B8, a densely interconnected network of low angle boundaries accompanied by a significant number of equiaxed subgrains are apparent from the accumulation of green boundaries, which indicates a higher degree of recovery. As was mentioned, the peak temperature of A8 was estimated to be higher than B8 during the process, resulting in lower Z-values for A8 and a higher probability of the activation of restoration mechanisms. In other words, the dynamic restoration zone for A8 is wider in A8 in comparison with B8, causing the microstructure of A8 to experience a higher degree of recovery.

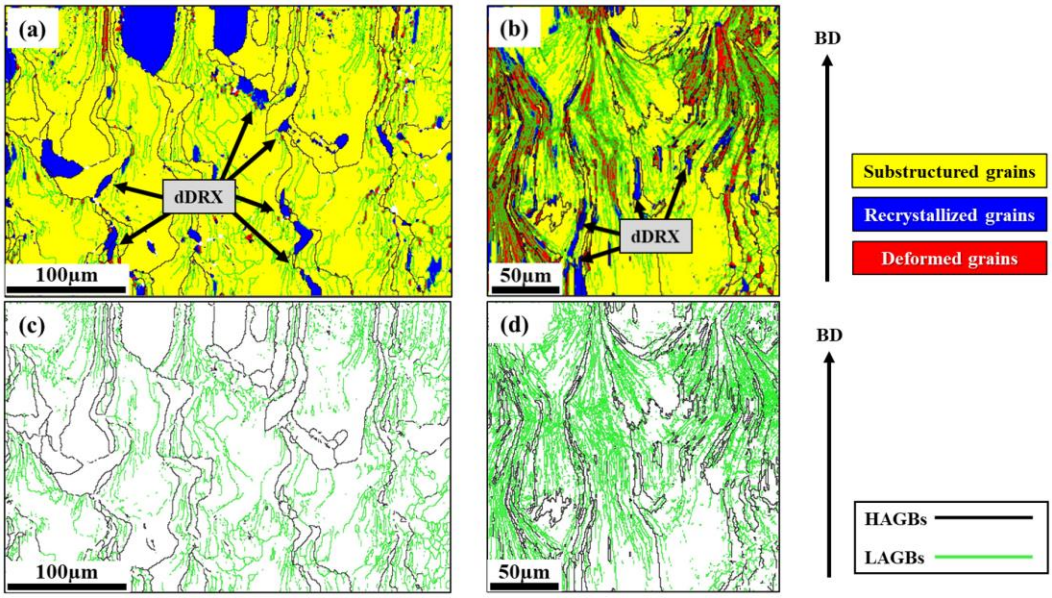

Figure 2-12 Restoration maps for (a) B8 and (b) A8 are shown in the top row, in which yellow, blue, and red colors indicate substructure, recrystallized, and deformed grains, respectively. In the bottom row, the grain boundary maps reveal the LAGB in green and HAGBs in black for (c) B8 and (d) A8.

Consequently, the microstructural observations confirm the conducted analytical predictions, indicating that DRV acts as the main restoration mechanism in microstructural

development and the substructural evolution of a NiTi alloy during the LPBF process. Furthermore, the higher the peak temperature of the melt pool, the higher the progress of the restoration mechanisms, specifically DRV, during the LPBF processing of NiTi alloys.

2.4.7 Hardness

The evolution of the microstructures of each sample during the process affects the mechanical properties of the fabricated part. To this end, the Vickers hardness (HV) of the fabricated specimens was measured by 36 indentations, and the values are illustrated in Figure 2-13 as a function of the volumetric energy density. Two different trends are observed from the measured HV values. In the left section of the graph, increasing the volumetric energy results in recording higher hardness values, but after reaching a peak value, HV decreases by further increasing the volumetric energy density. It was shown that increasing E_v leads to higher residual stresses in the material and a higher density of dislocations. This increase in the density of dislocations can stimulate the material to exhibit higher hardness values. However, the activation of recovery mechanisms and their progress can significantly affect the microstructure and the states of the dislocations. During recovery, those dislocations that have opposite signs are annihilated, and the LAGBs are derived into opposite directions, resulting in a network of equiaxed subgrains. The development of recovery mechanisms was confirmed for samples processed by higher heat inputs and therefore experienced higher temperatures. Thus, the occurrence of DRV mechanisms, along with the observed partially recrystallized substructure, mainly at higher heat inputs, can effectively decrease the dislocation density, reducing the material's hardness.

Additionally, higher levels of porosities, when higher volumetric energy densities are used, can also affect the hardness of the fabricated components. Although no indentations were

made directly on an area where a visible porosity was present, still the voids that are located in the deeper levels can cause a hardness drop. Therefore, the decrease in HV in higher energy densities is believed to be due to the combination of both recovery effects and the presence of porosities.

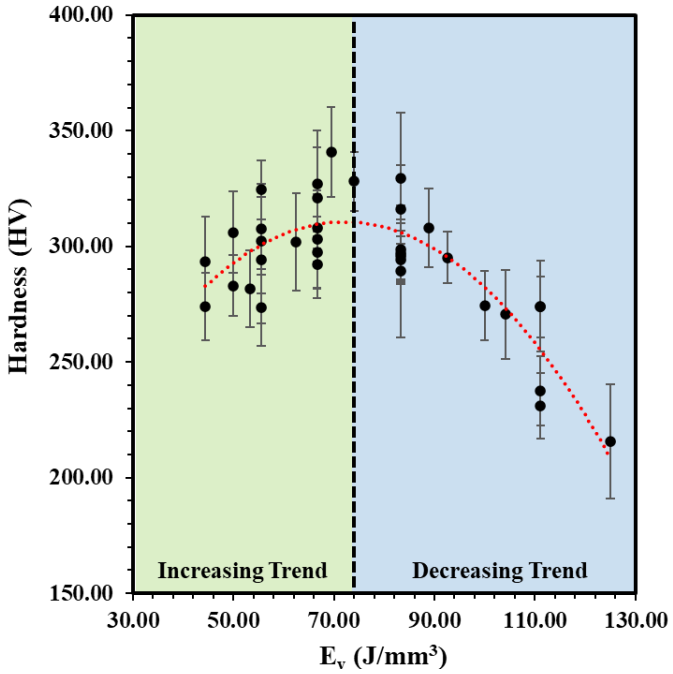

Figure 2-13 Vickers Hardness (HV) values as a function of volumetric energy density for all samples. A total of 36 indentations were made to estimate the mean HV and standard deviation.

2.4.8 Transformation behavior

The occurred changes in the behavior of the $A \leftrightarrow M$ transformation are critical regarding the fabricated parts' applications which should be carefully considered in LPBF of NiTi alloys. In the previous sections, it was presented that the chemical composition of the material and the microstructure of the fabricated samples are changed in different processing conditions. Both of these factors can affect the transformation behavior of the material.

Figure 2-14 demonstrates a schematic view of the acquired DSC curves of the LPBF processed samples. As is illustrated, two distinct peaks are evident in the DSC graphs, which are attributed to the exothermic $A \rightarrow M$ transformation in cooling and the endothermic $M \rightarrow A$ transformation in heating. As is marked in the figure, on the one hand, the values of the transformation temperatures can be extracted from the curves, and on the other hand, the area under the peaks can be calculated, which is proportional to the enthalpy of the transformation (ΔH). Accordingly, transformation temperatures, transformation enthalpy, and shape of the peaks reveal beneficial insights, which are discussed in the following by analyzing different samples fabricated at different volumetric energy densities.

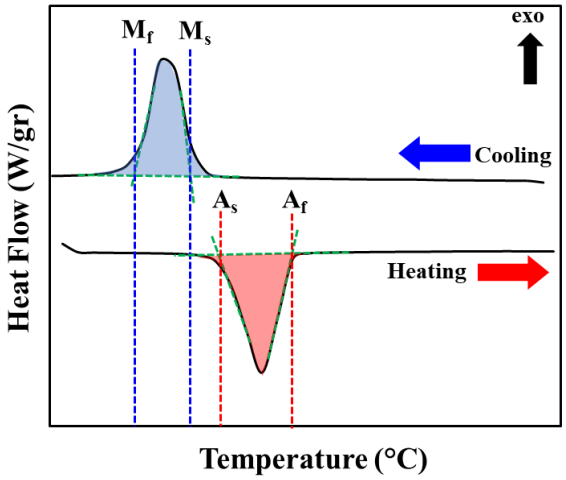

Figure 2-14 Schematic representation of a DSC curve of a NiTi alloy during a cooling or heating cycle.

The estimated values of the M_s and A_f for the fabricated samples are plotted in Figure 2-15(a) as a function of the volumetric energy density. As is shown, both transformation temperatures are increased by employing higher volumetric energy densities, which can be attributed to the changes in the chemical composition of the material. As was mentioned in

section 4.3, nickel evaporation in higher heat inputs can alter the chemical composition of the material, and the lower the nickel content of the matrix, the higher the temperature of the $B2 \leftrightarrow B19'$ transformations [72]. However, the changes in the transformation temperature cannot be governed by only the alterations of the chemical composition and the materials' different nickel contents. Different studies on cold worked NiTi alloys acknowledged that the transformation could be hindered by the presence of defects, thereby shifting the transformation temperatures to lower values during cooling [73,74]. These defects, which are basically dislocations, act as locking sites and hinder the free movement of the A/M mobile interface, causing transformation retardation [26]. To further investigate the transformation behavior of the fabricated samples, the values of $\Delta H_{B19'\rightarrow B2}$ and $\Delta H_{B2\rightarrow B19'}$ were calculated based on the DSC graphs, and the results are represented in Figure 2-15(b). The transformation enthalpy can be affected by the dissipated energy during the transformation, and the higher the transformation enthalpy, the lower the energy dissipation and the higher the mobility of the B2/B19′ interface [75].

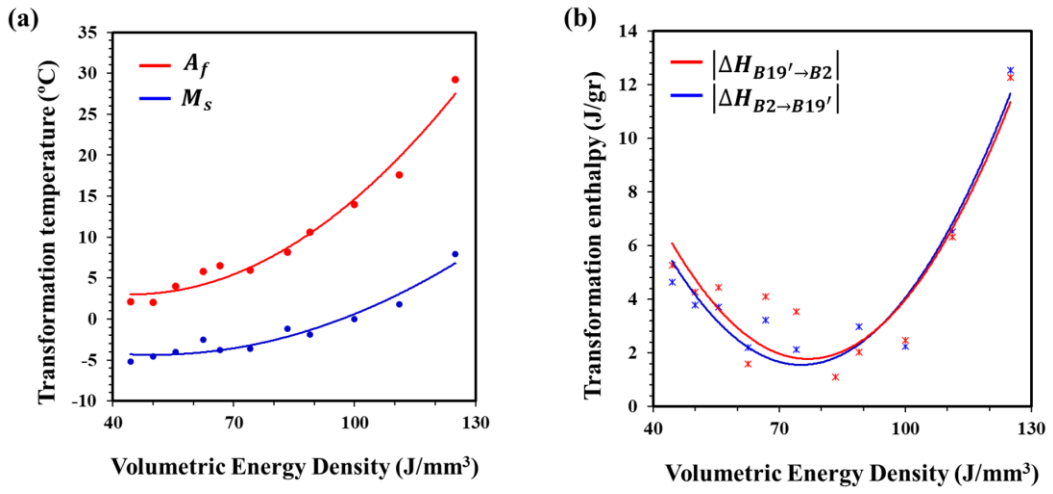

Figure 2-15 The estimated transformation (a) temperatures and (b) enthalpies for samples fabricated by different volumetric energy densities.

At a glance, the recorded enthalpies for all conditions are very low (<14J/gr), denoting the presence of a high number of defects and dense dislocation networks caused by the rapid non-equilibrium nature of the LPBF process. Interestingly, the observed trend for both transformation enthalpies corresponds to the hardness measurement in the previous section (Figure 2-13). Initially, samples have higher enthalpies at lower energy densities, but this value decreases to a minimum by further increasing the E_v. Therefore, the energy densities responsible for causing the highest hardness (i.e., highest dislocation densities) in the structure of samples lead to the lowest transformation enthalpies. Subsequently, the transformation enthalpies were increased in higher E_v values, ultimately resulting in the highest recorded enthalpy for the sample fabricated by the highest energy density. This is attributed to the previously mentioned fact that in higher heat inputs, the involvement of the dynamic restoration mechanisms is significantly boosted.

For further clarification, the DSC curves of different samples are exhibited in Figure 2-16. As a general rule, the sharper the peak, the fewer obstacles the transformation confronts, and the broader the peak, the higher the number of defects and the density of dislocations. As is illustrated, corresponding to the changes in the hardness values (Figure 2-13), the transformation peaks are easily distinguishable when low or high values of energy density are utilized, while they nearly vanish in medium E_v values. The findings in this section emphasize the role of the dynamic restoration mechanisms on the transformation behavior of the additively manufactured components and encourages future studies to assess the influence of these effects on the functional properties of the fabricated parts.

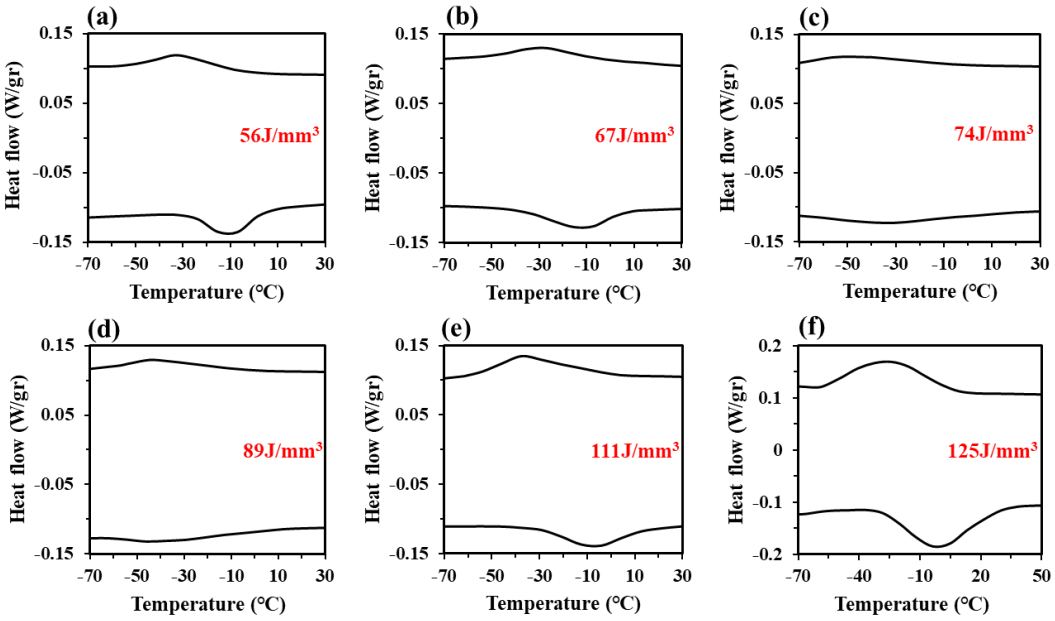

Figure 2-16 The acquired DSC curves for different samples manufactured by different volumetric energy density values.

2.5 Conclusion

Despite the previous studies on additive manufacturing of NiTi alloys, there are still many inadequacies and questions remained to be addressed. While numerous studies have acknowledged the development of high stresses during the LPBF processing of NiTi alloys, their effects were mostly assessed as an after-effect of the fabrication process, and their role in governing the occurrence of the microstructural evolution mechanisms, namely dynamic recovery and dynamic recrystallization has not been previously determined. In this regard, as a novel highlight of this work, a combination of numerical, analytical, and experimental approaches was utilized to evaluate the activity of the dynamic restoration mechanisms during the LPBF processing of NiTi alloys. On the one hand, predictions based on the Zener-Hollomon theory confirmed that the driving force for activating the DRV and DRX mechanisms is indeed provided in the LPBF processing of NiTi alloys, and

on the other hand, EBSD restoration fraction maps revealed that dynamic recovery is the dominant mechanism, although evidence of partial recrystallization was detected as well. Furthermore, it was found that increasing the heat input and the peak temperature of the process leads to the further progression of the restoration mechanisms and denser interconnected networks of substructures and subgrains. The results highlighted that the fabricated parts' properties, namely hardness and transformation behavior, are significantly affected by the involvement of these mechanisms at different volumetric energy densities. In this regard, lower hardness values and higher transformation enthalpies were acquired at higher energy levels, in which the microstructure of the material was significantly restored.

2.6 References

[1] S. Dadbakhsh, M. Speirs, J.P. Kruth, J. Schrooten, J. Luyten, J. Van Humbeeck, Effect of SLM parameters on transformation temperatures of shape memory nickel titanium parts, Adv. Eng. Mater. 16 (2014) 1140–1146. doi:10.1002/adem.201300558.

[2] G.P. Toker, M. Nematollahi, S.E. Saghaian, K.S. Baghbaderani, O. Benafan, M. Elahinia, H.E. Karaca, Shape memory behavior of NiTiHf alloys fabricated by selective laser melting, Scr. Mater. 178 (2020) 361–365. doi:10.1016/j.scriptamat.2019.11.056.

[3] N. Shayesteh Moghaddam, S. Saedi, A. Amerinatanzi, A. Hinojos, A. Ramazani, J. Kundin, M.J. Mills, H. Karaca, M. Elahinia, Achieving superelasticity in additively manufactured NiTi in compression without post-process heat treatment, Sci. Rep. 9 (2019) 1–11. doi:10.1038/s41598-018-36641-4.

[4] K. Otsuka, X. Ren, Physical metallurgy of Ti–Ni-based shape memory alloys, Prog. Mater. Sci. 50 (2005) 511–678. doi:10.1016/j.pmatsci.2004.10.001.

[5] J.P. Oliveira, N. Schell, N. Zhou, L. Wood, O. Benafan, Laser welding of precipitation strengthened Ni-rich NiTiHf high temperature shape memory alloys: Microstructure and mechanical properties, Mater. Des. 162 (2019) 229–234. doi:10.1016/j.matdes.2018.11.053.

[6] A. Safdel, A. Zarei-Hanzaki, H.R. Abedi, S. Pourbabak, D. Schryvers, R. Basu, Asymmetrical superelastic behavior of thermomechanically processed semi-equiatomic NiTi alloy in tensile and compressive modes of deformation, J. Alloys Compd. 878 (2021) 160443. doi:10.1016/j.jallcom.2021.160443.

[7] T. Habijan, C. Haberland, H. Meier, J. Frenzel, J. Wittsiepe, C. Wuwer, C. Greulich, T.A. Schildhauer, M. Köller, The biocompatibility of dense and porous Nickel–Titanium produced by selective laser melting, Mater. Sci. Eng. C. 33 (2012) 419–426. doi:10.1016/j.msec.2012.09.008.

[8] O. Benafan, R.D. Noebe, S. a. Padula, A. Garg, B. Clausen, S. Vogel, R. Vaidyanathan, Temperature dependent deformation of the B2 austenite phase of a

NiTi shape memory alloy, Int. J. Plast. 51 (2013) 103–121. doi:10.1016/j.ijplas.2013.06.003.

[9] J.J. Marattukalam, A.K. Singh, S. Datta, M. Das, V.K. Balla, S. Bontha, S.K. Kalpathy, Microstructure and corrosion behavior of laser processed NiTi alloy, Mater. Sci. Eng. C. 57 (2015) 309–313. doi:10.1016/j.msec.2015.07.067.

[10] J.W. Mwangi, L.T. Nguyen, V.D. Bui, T. Berger, H. Zeidler, A. Schubert, Nitinol manufacturing and micromachining: A review of processes and their suitability in processing medical-grade nitinol, J. Manuf. Process. 38 (2019) 355–369. doi:10.1016/j.jmapro.2019.01.003.

[11] S. Nagaraja, S.J.L. Sullivan, P.R. Stafford, A.D. Lucas, E. Malkin, Impact of nitinol stent surface processing on in-vivo nickel release and biological response, Acta Biomater. 72 (2018) 424–433. doi:10.1016/j.actbio.2018.03.036.

[12] K. Maleckis, E. Anttila, P. Aylward, W. Poulson, A. Desyatova, J. MacTaggart, A. Kamenskiy, Nitinol Stents in the Femoropopliteal Artery: A Mechanical Perspective on Material, Design, and Performance, Ann. Biomed. Eng. 46 (2018) 684–704. doi:10.1007/s10439-018-1990-1.

[13] A. Safdel, M.A. Elbestawi, Distortion and Printability of Stent Structures in Laser Powder Bed Fusion Processing of NiTi Alloys, Mater. Lett. (2021) 130163. doi:10.1016/j.matlet.2021.130163.

[14] M. Speirs, B. Van Hooreweder, J. Van Humbeeck, J.P. Kruth, Fatigue behaviour of NiTi shape memory alloy scaffolds produced by SLM, a unit cell design comparison, J. Mech. Behav. Biomed. Mater. 70 (2017) 53–59. doi:10.1016/j.jmbbm.2017.01.016.

[15] R. Bationo, C. Quilodran-naudon, F. Jordana, J. Colat-parros, In Vitro Assessment of Nickel Ion Release from Orthodontic Wires, ARC J. Dent. Sci. 4 (2019) 1–4. doi:10.20431/2456-0030.0404001.

[16] T. Bormann, R. Schumacher, B. Müller, M. Mertmann, M. De Wild, B. Muller, M. Mertmann, M. De Wild, Tailoring selective laser melting process parameters for NiTi implants, J. Mater. Eng. Perform. 21 (2012) 2519–2524. doi:10.1007/s11665-

012-0318-9.

[17] M. Elahinia, N. Shayesteh Moghaddam, M. Taheri Andani, A. Amerinatanzi, B.A. Bimber, R.F. Hamilton, Fabrication of NiTi through additive manufacturing: A review, Prog. Mater. Sci. 83 (2016) 630–663. doi:10.1016/j.pmatsci.2016.08.001.

[18] S. Saedi, N. Shayesteh Moghaddam, A. Amerinatanzi, M. Elahinia, H.E. Karaca, On the effects of selective laser melting process parameters on microstructure and thermomechanical response of Ni-rich NiTi, Acta Mater. 144 (2018) 552–560. doi:10.1016/j.actamat.2017.10.072.

[19] S. Saedi, A.S. Turabi, M.T. Andani, C. Haberland, H. Karaca, M. Elahinia, The influence of heat treatment on the thermomechanical response of Ni-rich NiTi alloys manufactured by selective laser melting, J. Alloys Compd. 677 (2016) 204–210. doi:10.1016/j.jallcom.2016.03.161.

[20] Q. Zhou, M.D. Hayat, G. Chen, S. Cai, X. Qu, H. Tang, P. Cao, Selective electron beam melting of NiTi: Microstructure, phase transformation and mechanical properties, Mater. Sci. Eng. A. 744 (2019) 290–298. doi:10.1016/j.msea.2018.12.023.

[21] Z. Xiong, Z. Li, Z. Sun, S. Hao, Y. Yang, M. Li, C. Song, P. Qiu, L. Cui, Selective laser melting of NiTi alloy with superior tensile property and shape memory effect, J. Mater. Sci. Technol. 35 (2019) 2238–2242. doi:10.1016/j.jmst.2019.05.015.

[22] S. Dadbakhsh, B. Vrancken, J.-P.P. Kruth, J. Luyten, J. Van Humbeeck, Texture and anisotropy in selective laser melting of NiTi alloy, Mater. Sci. Eng. A. 650 (2016) 225–232. doi:10.1016/j.msea.2015.10.032.

[23] J. Van Humbeeck, M. Speirs, X. Li, J.-P. Kruth, B. Vrancken, X. Wang, S. Kustov, Selective laser melting produced layer-structured NiTi shape memory alloys with high damping properties and Elinvar effect, Scr. Mater. 146 (2017) 246–250. doi:10.1016/j.scriptamat.2017.11.047.

[24] T. DebRoy, H.L. Wei, J.S. Zuback, T. Mukherjee, J.W. Elmer, J.O. Milewski, A.M. Beese, A. Wilson-Heid, A. De, W. Zhang, Additive manufacturing of metallic components – Process, structure and properties, Prog. Mater. Sci. 92 (2018) 112–

224. doi:10.1016/j.pmatsci.2017.10.001.

[25] E. Mirkoohi, H.C. Tran, Y.L. Lo, Y.C. Chang, H.Y. Lin, S.Y. Liang, Analytical mechanics modeling of residual stress in laser powder bed considering flow hardening and softening, Int. J. Adv. Manuf. Technol. 107 (2020) 4159–4172. doi:10.1007/s00170-020-05304-y.

[26] A. Safdel, A. Zarei-Hanzaki, A. Shamsolhodaei, P. Krooß, T. Niendorf, Room temperature superelastic responses of NiTi alloy treated by two distinct thermomechanical processing schemes, Mater. Sci. Eng. A. 684 (2017) 303–311. doi:10.1016/j.msea.2016.12.047.

[27] C.P. Frick, A.M. Ortega, J. Tyber, K. Gall, H.J. Maier, Multiscale structure and properties of cast and deformation processed polycrystalline NiTi shape-memory alloys, Metall. Mater. Trans. A. 35 (2004) 2013–2025. doi:10.1007/s11661-004-0150-4.

[28] A. Shamsolhodaei, A. Zarei-Hanzaki, M. Moghaddam, Structural and functional properties of a semi equiatomic NiTi shape memory alloy processed by multi-axial forging, Mater. Sci. Eng. A. 700 (2017) 1–9. doi:10.1016/j.msea.2017.04.011.

[29] ASTM F2063-18, Standard Specification for Wrought Nickel-Titanium Shape Memory Alloys for Medical Devices and Surgical Implants, West Conshohocken ASTM Int. (2018).

[30] R.F. Hamilton, B.A. Bimber, M. Taheri Andani, M. Elahinia, Multi-scale shape memory effect recovery in NiTi alloys additive manufactured by selective laser melting and laser directed energy deposition, J. Mater. Process. Technol. 250 (2017) 55–64. doi:10.1016/j.jmatprotec.2017.06.027.

[31] M. Narvan, K.S. Al-Rubaie, M. Elbestawi, Process-Structure-Property Relationships of AISI H13 Tool Steel Processed with Selective Laser Melting, Materials (Basel). 12 (2019) 2284. doi:10.3390/ma12142284.

[32] U. Scipioni Bertoli, A.J. Wolfer, M.J. Matthews, J.P.R. Delplanque, J.M. Schoenung, On the limitations of Volumetric Energy Density as a design parameter for Selective Laser Melting, Mater. Des. 113 (2017) 331–340.

doi:10.1016/j.matdes.2016.10.037.

[33] C. Haberland, M. Elahinia, J.M. Walker, H. Meier, J. Frenzel, On the development of high quality NiTi shape memory and pseudoelastic parts by additive manufacturing, Smart Mater. Struct. 23 (2014). doi:10.1088/0964-1726/23/10/104002.

[34] C. Haberland, M. Elahinia, J.M. Walker, S. Saedi, A.S. Turabi, M.T. Andani, Thermomechanical characterization of Ni- rich NiTi fabricated by selective laser melting, Smart Mater. Struct. 25 (2016).

[35] J.M. Walker, C. Haberland, M. Taheri Andani, H.E. Karaca, D. Dean, M. Elahinia, Process development and characterization of additively manufactured nickel-titanium shape memory parts, J. Intell. Mater. Syst. Struct. 27 (2016) 2653–2660. doi:10.1177/1045389X16635848.

[36] T. Bormann, B. Müller, M. Schinhammer, A. Kessler, P. Thalmann, M. De Wild, B. M??ller, M. Schinhammer, A. Kessler, P. Thalmann, M. De Wild, B. Müller, M. Schinhammer, A. Kessler, P. Thalmann, M. De Wild, Microstructure of selective laser melted nickel-titanium, Mater. Charact. 94 (2014) 189–202. doi:10.1016/j.matchar.2014.05.017.

[37] I. Shishkovsky, I. Yadroitsev, I. Smurov, Direct Selective Laser Melting of Nitinol Powder, Phys. Procedia. 39 (2012) 447–454. doi:10.1016/j.phpro.2012.10.060.

[38] M. Speirs, X. Wang, S. Van Baelen, A. Ahadi, S. Dadbakhsh, J.-P. Kruth, J. Van Humbeeck, On the Transformation Behavior of NiTi Shape-Memory Alloy Produced by SLM, Shape Mem. Superelasticity. 2 (2016) 310–316. doi:10.1007/s40830-016-0083-y.

[39] M. Taheri Andani, S. Saedi, A.S. Turabi, M.R. Karamooz, C. Haberland, H.E. Karaca, M. Elahinia, Mechanical and shape memory properties of porous Ni50.1Ti49.9alloys manufactured by selective laser melting, J. Mech. Behav. Biomed. Mater. 68 (2017) 224–231. doi:10.1016/j.jmbbm.2017.01.047.

[40] D.C. Ren, H.B. Zhang, Y.J. Liu, S.J. Li, W. Jin, R. Yang, L.C. Zhang, Microstructure and properties of equiatomic Ti–Ni alloy fabricated by selective

laser melting, Mater. Sci. Eng. A. 771 (2020). doi:10.1016/j.msea.2019.138586.

[41] Y. Yang, J.B. Zhan, B. Li, J.X. Lin, J.J. Gao, Z.Q. Zhang, L. Ren, P. Castany, T. Gloriant, Laser beam energy dependence of martensitic transformation in SLM fabricated NiTi shape memory alloy, Materialia. 6 (2019). doi:10.1016/j.mtla.2019.100305.

[42] W. Chen, Q. Yang, S. Huang, S. Huang, J.J. Kruzic, X. Li, Laser power modulated microstructure evolution, phase transformation and mechanical properties in NiTi fabricated by laser powder bed fusion, J. Alloys Compd. 861 (2021) 157959. doi:10.1016/j.jallcom.2020.157959.

[43] ASTM F2004, Standard Test Method for Transformation Temperature of Nickel-Titanium Alloys by thermal analysis, 05 (2015) 7–10. doi:10.1520/F2004-05R10.2.

[44] M. Yakout, M.A. Elbestawi, S.C. Veldhuis, S. Nangle-Smith, Influence of thermal properties on residual stresses in SLM of aerospace alloys, Rapid Prototyp. J. 26 (2020) 213–222. doi:10.1108/RPJ-03-2019-0065.

[45] M. Yakout, M.A. Elbestawi, S.C. Veldhuis, A study of the relationship between thermal expansion and residual stresses in selective laser melting of Ti-6Al-4V, J. Manuf. Process. 52 (2020) 181–192. doi:10.1016/j.jmapro.2020.01.039.

[46] M. Narvan, A. Ghasemi, E. Fereiduni, S. Kendrish, M. Elbestawi, Part deflection and residual stresses in laser powder bed fusion of H13 tool steel, Mater. Des. 204 (2021) 109659. doi:10.1016/j.matdes.2021.109659.

[47] M. Yakout, M.A. Elbestawi, Residual Stress Formation in Laser-Based Powder Bed Fusion (PBF-LB) of Invar 36, Struct. Integr. Addit. Manuf. Mater. Parts. (2020) 34–44. doi:10.1520/stp163120190149.

[48] C. Li, J.F. Liu, X.Y. Fang, Y.B. Guo, Efficient predictive model of part distortion and residual stress in selective laser melting, Addit. Manuf. 17 (2017) 157–168. doi:10.1016/j.addma.2017.08.014.

[49] A. Shamsolhodaei, Q. Sun, X. Wang, B. Panton, H. Di, Y.N. Zhou, Effect of Laser Positioning on the Microstructure and Properties of NiTi-Copper Dissimilar Laser

Welds, J. Mater. Eng. Perform. 29 (2020) 849–857. doi:10.1007/s11665-020-04637-9.

[50] A.J. Neurohr, D.C. Dunand, Mechanical anisotropy of shape-memory NiTi with two-dimensional networks of micro-channels, Acta Mater. 59 (2011) 4616–4630. doi:10.1016/j.actamat.2011.04.007.

[51] F. Nematzadeh, S.K. Sadrnezhaad, Effects of material properties on mechanical performance of Nitinol stent designed for femoral artery: Finite element analysis, Sci. Iran. 19 (2012) 1564–1571. doi:10.1016/j.scient.2012.10.024.

[52] C. Zanotti, P. Giuliani, G. Riva, A. Tuissi, A. Chrysanthou, Thermal diffusivity of Ni-Ti SMAs, J. Alloys Compd. 473 (2009) 231–237. doi:10.1016/j.jallcom.2008.05.040.

[53] J.E. Favelukis, A.S. Lavine, G.P. Carman, Experimentally validated thermal model of thin film NiTi, Smart Struct. Mater. 1999 Smart Struct. Integr. Syst. 3668 (1999) 617–629. doi:10.1117/12.350737.

[54] A.F.F. Saleeb, B. Dhakal, S. Dilibal, J.S.S. Owusu-Danquah, S.A. Padula II, On the modeling of the thermo-mechanical responces of four different classes on NiTi-based shape memory materials using a general multi-mechanism framework, Mech. Mater. 80 (2015) 67–86. doi:10.1016/j.mechmat.2014.09.001.

[55] F. Calignano, Design optimization of supports for overhanging structures in aluminum and titanium alloys by selective laser melting, Mater. Des. 64 (2014) 203–213. doi:10.1016/j.matdes.2014.07.043.

[56] P. Vora, K. Mumtaz, I. Todd, N. Hopkinson, AlSi12 in-situ alloy formation and residual stress reduction using anchorless selective laser melting, Addit. Manuf. 7 (2015) 12–19. doi:10.1016/j.addma.2015.06.003.

[57] H.S. Park, D.S. Nguyen, Study on Flaking Behavior in Selective Laser Melting Process, Procedia CIRP. 63 (2017) 569–572. doi:10.1016/j.procir.2017.03.146.

[58] D. Wang, Y. Yang, R. Liu, D. Xiao, J. Sun, Study on the designing rules and processability of porous structure based on selective laser melting (SLM), J. Mater.

Process. Technol. 213 (2013) 1734–1742. doi:10.1016/j.jmatprotec.2013.05.001.

[59] Y. Liu, Y. Yang, D. Wang, A study on the residual stress during selective laser melting (SLM) of metallic powder, Int. J. Adv. Manuf. Technol. 87 (2016) 647–656. doi:10.1007/s00170-016-8466-y.

[60] S.A.R. Shamsdini, M.H. Ghoncheh, M. Mohammadi, Effect of recoater-blade type on the mechanical properties and microstructure of additively manufactured maraging steels, Mater. Sci. Eng. A. 812 (2021) 141104. doi:10.1016/j.msea.2021.141104.

[61] A. Michael, Y.N. Zhou, M. Yavuz, M.I. Khan, Modelling the alloy element composition change in NiTi achieved through laser induced vaporization, Mater. Chem. Phys. 231 (2019) 87–94. doi:10.1016/j.matchemphys.2019.04.015.

[62] H.E. Sabzi, N.T. Aboulkhair, X. Liang, X.H. Li, M. Simonelli, H. Fu, P.E.J. Rivera-Díaz-del-Castillo, Grain refinement in laser powder bed fusion: The influence of dynamic recrystallization and recovery, Mater. Des. 196 (2020). doi:10.1016/j.matdes.2020.109181.

[63] A. Ahadi, A. Karimi Taheri, K. Karimi Taheri, I.S. Sarraf, S.M. Abbasi, The effect of deformation heating on restoration and constitutive equation of a wrought equiatomic NiTi alloy, J. Mater. Eng. Perform. 21 (2012) 516–523. doi:10.1007/s11665-011-9936-x.

[64] H. Eskandari Sabzi, P.E.J. Rivera-Díaz-del-Castillo, Composition and process parameter dependence of yield strength in laser powder bed fusion alloys, Mater. Des. 195 (2020) 109024. doi:10.1016/j.matdes.2020.109024.

[65] W.E. King, H.D. Barth, V.M. Castillo, G.F. Gallegos, J.W. Gibbs, D.E. Hahn, C. Kamath, A.M. Rubenchik, Observation of keyhole-mode laser melting in laser powder-bed fusion additive manufacturing, J. Mater. Process. Technol. 214 (2014) 2915–2925. doi:10.1016/j.jmatprotec.2014.06.005.

[66] H.E. Sabzi, S. Maeng, X. Liang, M. Simonelli, N.T. Aboulkhair, P.E.J. Rivera-Díaz-del-Castillo, Controlling crack formation and porosity in laser powder bed fusion: Alloy design and process optimisation, Addit. Manuf. 34 (2020) 101360.

doi:10.1016/j.addma.2020.101360.

[67] A. Hussein, L. Hao, C. Yan, R. Everson, Finite element simulation of the temperature and stress fields in single layers built without-support in selective laser melting, Mater. Des. 52 (2013) 638–647. doi:10.1016/j.matdes.2013.05.070.

[68] M. Morakabati, S. Kheirandish, M. Aboutalebi, a. K. Taheri, S.M. Abbasi, A study on the hot workability of wrought NiTi shape memory alloy, Mater. Sci. Eng. A. 528 (2011) 5656–5663. doi:10.1016/j.msea.2011.04.036.

[69] A.A. Khamei, K. Dehghani, Modeling the hot-deformation behavior of Ni60 wt%-Ti40 wt% intermetallic alloy, J. Alloys Compd. 490 (2010) 377–381. doi:10.1016/j.jallcom.2009.09.187.

[70] A. Shamsolhodaei, A. Zarei-Hanzaki, M. Ghambari, S. Moemeni, The high temperature flow behavior modeling of NiTi shape memory alloy employing phenomenological and physical based constitutive models: A comparative study, Intermetallics. 53 (2014) 140–149. doi:10.1016/j.intermet.2014.04.015.

[71] F. Yazdandoost, R. Mirzaeifar, Generalized stacking fault energy and dislocation properties in NiTi shape memory alloys, J. Alloys Compd. 709 (2017) 72–81. doi:10.1016/j.jallcom.2017.03.090.

[72] J. Frenzel, E.P. George, a. Dlouhy, C. Somsen, M.F.X. Wagner, G. Eggeler, Influence of Ni on martensitic phase transformations in NiTi shape memory alloys, Acta Mater. 58 (2010) 3444–3458. doi:10.1016/j.actamat.2010.02.019.

[73] F. Khelfaoui, G. Guénin, Influence of the recovery and recrystallization processes on the martensitic transformation of cold worked equiatomic Ti-Ni alloy, Mater. Sci. Eng. A. 355 (2003) 292–298. doi:10.1016/S0921-5093(03)00068-6.

[74] H. Shahmir, M. Nili-Ahmadabadi, F. Naghdi, Superelastic behavior of aged and thermomechanical treated NiTi alloy at Af+10C, Mater. Des. 32 (2011) 365–370. doi:10.1016/j.matdes.2010.06.022.

[75] A. Nespoli, E. Villa, L. Bergo, A. Rizzacasa, F. Passaretti, DSC and three-point bending test for the study of the thermo-mechanical history of NiTi and NiTi-based

orthodontic archwires, J. Therm. Anal. Calorim. 120 (2015) 1129–1138. doi:10.1007/s10973-015-4441-3.

Chapter 3

The role of texture and restoration mechanisms in defining the tension-compression asymmetry behavior of aged NiTi alloys fabricated by laser powder bed fusion

Complete Citation:

A. Safdel, N. Zaker, G.A. Botton, M.A. Elbestawi, The role of texture and restoration mechanisms in defining the tension-compression asymmetry behavior of aged NiTi alloys fabricated by laser powder bed fusion, Mater. Sci. Eng. A. 864 (2023) 144592. doi:10.1016/j.msea.2023.144592.

Abstract:

Tension-compression asymmetry is an inherent property of superelastic NiTi alloys linked to the microstructural evolutions and the stress induced martensite transformation during different deformation modes. Deep understanding of NiTi's asymmetry, a topic that is often overlooked in additive manufacturing, is imperative in designing functional parts that experience multiple deformation modes. Accordingly, in this paper, the asymmetry parameters, namely the critical stress for martensite transformation, transformation strain, and strain recoverability were measured for an aged material with optimum superelasticity, which was fabricated by two different scanning strategies. The acquired results were correlated to the changes in the developed texture components during laser powder bed fusion and subsequent annealing processes, highlighting the role of dynamic and static restoration mechanisms, respectively. The deviation of texture from <001>||building direction, caused by the occurrence of the restoration mechanisms during fabrication and subsequent aging, was found to be dissimilar for samples fabricated by 67º or 90º rotation angles, effectively impacting the behavior of the material in different deformation modes. For a sample with enhanced superelasticity, aged at 550°C for 6 hours, 90º scanning strategy resulted in lower asymmetry and superior superelasticity in compression, while 67º rotations led to highest strain recoverability in tension, but an intensified asymmetrical behavior.

Keywords:

NiTi; Laser powder bed fusion; Superelasticity; Asymmetry; Restoration mechanisms.

3.1 Introduction

The discovery of the shape memory effect (SME) in near-equiatomic Ni-Ti alloys in 1963 has triggered a plethora of scientific research on this material's functional properties and promising applications [1]. Numerous studies later revealed that in addition to the SME, NiTi alloys are also capable of exhibiting remarkable superelasticity (SE) and biocompatibility, resulting in their extensive applications in biomedical, aerospace, and civil industries [2–4]. Currently, various stent structures [5–7], orthodontic wires [8,9], scaffolds [10,11], and implants [12,13] are manufactured from NiTi alloys. While SME denotes the behavior of the material to recover a high degree of deformation upon heating, SE is a functional property in which a highly deformed material can return to its initial shape just by unloading [14]. The underlying reasons for observing such unique functional properties lie beneath the presence of two main phases: (1) austenite (A) as the high temperature symmetrical phase, having a cubic B2 crystallographic structure, and (2) martensite (M) as the low temperature asymmetrical phase with B19' monoclinic crystal structure [15]. The martensitic transformation in NiTi alloys is a thermoelastic transition with a relatively small hysteresis meaning that the austenite or martensite phase can transform into each other by a very low strain or temperature stimuli [16].

For superelastic shape memory alloys (SMAs) such as NiTi alloys, stress-induced martensite (SIM) transformation occurs during the loading of an austenitic material leading to a semi-plateau region in the stress-strain flow curve [17,18]. In this region, different martensite variants can form from the austenite parent phase, and afterward, during unloading, reverse transformation takes place, and the initial austenite structure is recovered. Various studies pointed out that high strain values of around 8% can be retrieved during load-unload tensile tests for a NiTi alloy with enhanced SE behavior through elastic

and superelastic recovery mechanisms [19–21]. However, it should be mentioned that this level of recovery is not accessible without conducting a series of post heat-treatments in which (1) dislocations annihilate or rearrange, (2) restoration occurs, and (3) nano-sized coherent Ni_4Ti_3 precipitates form, hindering the movement of the dislocations and facilitating the occurrence of the SIM transformation [22,23].

While understanding SE is imperative in terms of designs and applications, several interconnected factors play an important role in complicating the issue. In many applications, the NiTi alloys experience various modes of deformation during their service condition; accordingly, the SE response is affected and the SIM transformation is governed by the deformation mode [24]. This behavior is related to NiTi's asymmetrical properties, a term introduced a few years after its discovery. To put it simply, asymmetry is the dissimilarity of the stress-strain curves when a NiTi alloy is loaded in different modes of deformation, such as tension and compression [25]. Although early investigations mainly pointed out texture as the leading cause of asymmetric properties, showing that single crystals in different directions exhibit remarkably distinct responses during deformation in different modes, later studies confirmed that this behavior is an inherent property of NiTi alloys since a highly symmetric austenite cubic phase is transformed into an asymmetrical martensite phase [26–28]. Consequently, asymmetry cannot be eliminated and can only be controlled and manipulated by selecting an optimum processing condition. Nonetheless, the texture still plays a significant role in defining the asymmetric behavior, and in this regard, researchers verified that crystallographic orientations near <111> parallel to the loading direction (LD) are favored in the tensile mode of deformation. On the other hand, having grains oriented toward <100> directions indicates that the SIM transformation

occurs at lower stress levels during compression, in which higher strain levels can be accommodated [29,30].

From a manufacturing perspective, it has never been a straightforward process to fabricate NiTi alloys, mainly due to the changes in the chemical composition during the process, the required inert atmosphere, and the limitations in producing complex geometries [31]. The advent of additive manufacturing (AM) processes promised new opportunities to fabricate geometrically complex parts in a controlled atmosphere using pre-alloyed NiTi powder particles [32,33]. Laser powder bed fusion (LPBF), among many AM processes, gained significant attention in which a laser beam selectively scans a thin layer of powder based on a computer-aided design (CAD) model, simultaneously melting and fusing the powder particles layer after layer, contributing to the fabrication of the final part [34].

However, a series of new challenges were encountered in LPBF, such as the presence of different defects, porosities, cracks, lack of fusion, and high values of residual stresses. In recent years, numerous studies [35–37] focused on online monitoring of the LPBF process, aiming to control and eliminate the presence of different defects such as lack of fusions, keyhole, or gas porosities through different imaging techniques. Such studies are imperative in terms of further enhancing the capabilities of the LPBF process and future developments of additive manufacturing technologies to manufacture high quality parts with the desired properties. Moreover, the development of stresses during the LPBF process is another important topic since the fabricated parts' final microstructure and properties can be affected by the level of developed stresses. The measurement of stresses throughout the LPBF process is a challenging task compelling researchers to mostly exploit numerical approaches to simulate and assess the developed residual stresses, although some recent detailed investigations have benefited from novel methodologies, such as

three-dimensional digital image correlation (3D-DIC) to capture the surface distortion during the process and determine the generation of stresses in an in-situ manner [38,39].

In a recent study [40], the present authors systematically examined the effects of numerous process parameters on NiTi parts' integrity and suggested an optimum condition to manufacture dense (relative density >99.8%) NiTi parts with a low level of residual stresses and negligible nickel vaporization. While some aspects of the superelastic response of additively manufactured NiTi alloys have been examined in a few studies [41–44], there is still a considerable lack of understanding regarding the effects of post heat treatment procedures in evolving the microstructure, texture, precipitates, and activating the restoration mechanisms. Most importantly, the "tension-compression asymmetrical behavior" of the LPBF processed NiTi alloys with optimum superelasticity which experience the occurrence of the dynamic and static restoration mechanisms during LPBF and subsequent aging treatments, respectively, has not been yet scrutinized. As is well established, AM processes such as LPBF lead to the formation of elongated grains in a direction that offers the highest heat flow, i.e., the building direction, and in most cases, inverse pole figure (IPF) maps obtained from as-built parts demonstrate the development of a preferred texture close to <100> directions along the building direction (BD) [34]. Interestingly, this favorable orientation toward the <100> direction differs from most of the previously investigated textures formed during conventional processing of NiTi alloys. Generally, the texture is skewed towards <111> and <110> directions for cold worked and subsequently annealed NiTi alloys which are capable of exhibiting the utmost tensile strain recovery and enhanced SE based on the literature [27,45,46].

Consequently, this paper aims to primarily provide a better understanding of the effect of post heat treatment on the tensile and compressive asymmetrical behavior of the LPBF

processed NiTi alloys by focusing on the microstructure evolution, texture, involvement of restoration mechanisms, and the formation of precipitates. Nonetheless, the optimum conditions for achieving a superior SE response in both tensile and compressive deformation modes should be initially investigated. Furthermore, as a highlight of this work, the tension-compression asymmetry behavior of the aged additively manufactured sample with the highest strain recoverability, introduced as the optimum SE sample, will be scrutinized considering the interconnected effects of texture and microstructure, justifiable by the previously established theoretical calculations. Accordingly, the critical foundation for understanding NiTi's functionality is laid to design more efficient components in future studies.

3.2 Materials and methods

The Ni-rich Ni-Ti powder with the chemical composition represented in Table 3-1 was received from the AP&C company (a GE additive company) in Quebec, Canada, which complies with the F2063 standard related to the use of NiTi alloys for medical applications.

Table 3-1 Chemical composition of the initial feedstock (weight percent)

Element	Ni	C	Co	Cu	Cr	Fe	Nb	N + O	Ti
Measured	55.7	0.034	0.010	0.001	0.004	0.023	<0.002	0.021	Bal.

Figure 3-1(a) depicts the obtained images of the powder particles captured by a JEOL6610 scanning electron microscope (SEM). Since the powder particles were plasma atomized from a pre-alloyed NiTi alloy in an inert argon atmosphere, not only they are perfectly spherical in shape without any signs of satellites, but also no inhomogeneity or evidence of secondary phases was observed, showing the high quality of the supplied powder.

Several SEM images were acquired and converted into binary black and white pictures to measure the particle size distribution (PSD) in the commercial ImageJ software. As is plotted in Figure 3-1(b), the calculated cumulative distribution of particles indicates that D10, D50, and D90 values were approximately 14, 27, and 40μm, respectively, which denotes the suitability of the supplied powder for the LPBF process [47]. Furthermore, the X-ray diffraction (XRD) pattern of the NiTi powder, presented in Figure 3-1(c), is consistent with a fully austenitic B2 structure, in which a sharp austenite characteristic peak appears at $2\theta \approx 42°$. An austenitic matrix in NiTi alloys is the main prerequisite for having SE capabilities due to the role of SIM transformation on strain accommodation during loading and reverse transformation on strain recovery during unloading [48]. The XRD analysis was conducted using a CuK_α (λ=1.54$\dot{A}$) radiation in 2θ range of 30-120°.

Differential scanning calorimetry (DSC) analysis was carried out in a temperature range of -70 to 50°C, comprising a heating and cooling cycle and employing a rate of 10°C/min. The corresponding DSC curves are demonstrated in Figure 3-1(d), pointing out the $A \rightarrow M$ transformation temperatures during cooling (blue curve) and the reverse $M \rightarrow A$ transformation temperatures during heating (red curve) of the feedstock powder particles. Consequently, the M_s, M_f, A_s, and A_f transformation temperatures were measured to be around -11, -34, -25, and 3°C, respectively, enabling the material to exhibit enhanced SE at room temperature if correctly treated.

In the LPBF process, numerous factors play an imperative role in determining the fabricated parts' structural integrity, microstructure, physical, and mechanical properties, among which, laser power (P), laser scanning speed (v), hatch distance (h), and layer thickness (t) are the easiest ones to maintain and control in order to ensure manufacturability, reliability, and repeatability. Generally, the values of these parameters

are utilized to derive the volumetric energy density ($E_v - J/mm^3$) value, most commonly referred to as a criterion determining the part's printability [49].

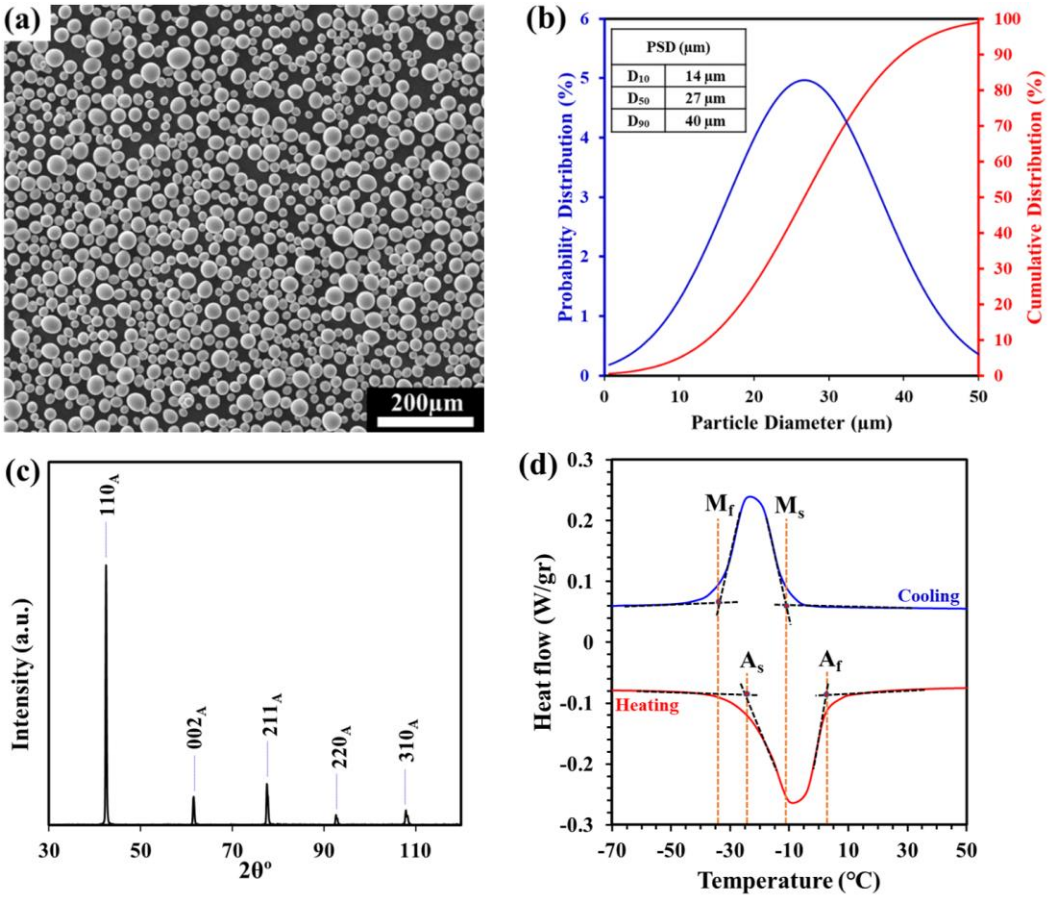

Figure 3-1 The (a) captured SEM image of the as-received NiTi powder feedstock along with its (b) particle size distribution graph, (c) X-ray diffraction pattern, and (d) DSC curves.

Based on a previously published experiment [40], the authors obtained the optimum LPBF processing parameters to manufacture NiTi parts, as summarized in Figure 3-1, which were selected in this study for fabricating NiTi components with the required designs.

Table 3-2 The optimum processing parameters for LPBF processing of NiTi alloys

P (W)	v (mm/s)	h (mm)	t (mm)	E_v (J/mm^3)
100	750	0.08	0.03	55.56

As is illustrated in Figure 3-2, two distinct scanning strategies were employed for this study in which the laser path continuously alternates in the x-axis and y-axis directions and sequentially rotates either 90° or 67°, corresponding to Figure 3-2(a) and Figure 3-2(b), respectively. When a rotation degree of 90° is employed, the laser passes four different iterations before returning to the initial passage. However, the maximum variance is achievable by maintaining a prime angle of 67° in each rotation, contributing to a more randomized structure [50–52]. Moreover, various studies have also proved that the microstructure and texture of parts fabricated by the LPBF process can be affected by utilizing 67º and 90º rotational angles due to the changes in the temperature fields during the process and generation of asymmetric stresses [52,53]. Nonetheless, through the first sections of this study, only the 90° rotation angle is considered for establishing a baseline compared to the previous studies, and the provided results in section 3.3.4 focus on the alternate 67º angle. As depicted in the figure, the stripe width was also limited to 5mm in each laser pass, with an overlap of 100µm, to avoid high heat accumulation in a particular direction and decrease the levels of thermal gradients and residual stresses.

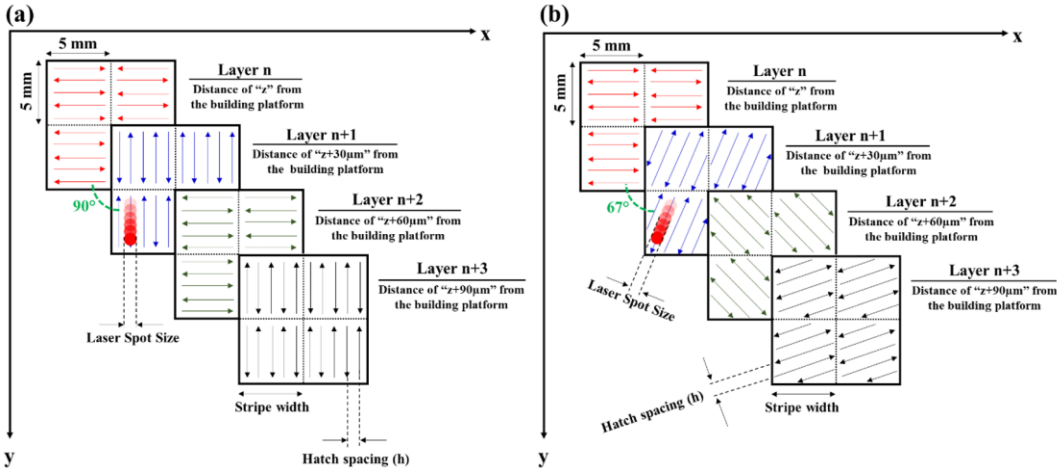

Figure 3-2 The incorporated scanning strategy showing alternating x/y laser passes rotated by (a) 90º and (b) 67º in each successive layer.

An EOS-M280 selective laser melting (SLM) machine (EOS, Germany) was utilized to manufacture the parts, which employs a fiber laser capable of providing a maximum power of 400W. An argon atmosphere was maintained throughout the building process, and specimens were fabricated on a custom-made NiTi building platform, preheated to 200°C to eliminate delamination and further limit the development of residual stresses. Finally, all the manufactured parts were removed from the building platform utilizing electro-discharge machining (EDM).

In order to assess and compare the superelasticity of additively manufactured NiTi alloys in tensile and compressive modes of deformation, samples were manufactured according to ASTM-E8 [54] and E9 [55] standards discussing the preparation of sub-sized specimens for tension and compression tests, respectively. The schematic drawing of the mentioned samples is presented in Figure 3-3. It should be noted that the thickness of all the tensile test samples was 1mm and the loading direction in both deformation modes was perpendicular to the building direction ($LD \perp BD$).

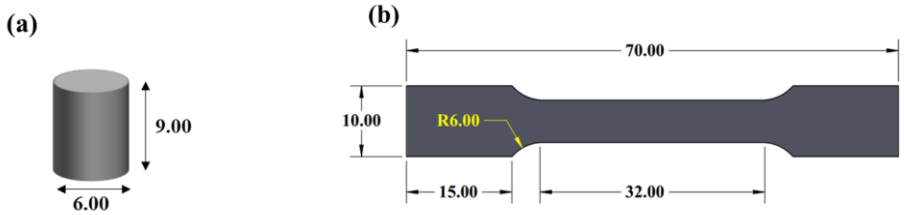

Figure 3-3 Schematic representation of the manufactured (a) compression and (b) tensile test specimens with a thickness of 1mm (all dimensions are in mm).

Heat treatments were conducted using a tube furnace filled with high purity argon gas to eliminate undesired oxidation and impurity pickup. The aging treatment was performed at temperatures of 450 and 550°C for 6, 12, 18, and 24 hours to promote the formation of Ni_4Ti_3 precipitates [56] and stimulate the occurrence of the restoration mechanisms [57].

All heat-treated samples were promptly quenched in room temperature water. For clarity, samples are coded by indicating the temperature and time of the aging process, meaning that 450-18 refers to a sample that was heat treated at 450℃ for 18 hours.

The superelastic response of the specimens was examined in step-by-step cyclic load-unloading tests in which the strain level was increased in increments of 2% up to a total strain value of 12% strain in compression and 8% in tension. Further loading may result in plastic deformation or fracture, which interferes with the discussions related to the SE behavior of the processed NiTi alloys [58]. A universal MTS instrument was utilized for the mechanical tests, and the stress-strain levels during the deformation were recorded under the strain rate of $0.001s^{-1}$ for both modes.

Figure 3-4 presents a schematical representation of the asymmetric behavior of the NiTi alloys during cyclic tension and compression tests. As is illustrated in the compressive portion of the graph, the NiTi alloy exhibits different behaviors during loading, marked by zones (I), (II), and (III) in the figure. Initially, in zone (I), the austenite parent phase is elastically deformed up to reaching a critical stress level, introduced as the SIM stress (σ_{SIM}). When this threshold is reached, the slope of the graph tends to decrease, creating a semi-plateau (zone II), in which various martensitic variants are formed by the progression of the SIM transformation. By further increasing the load and entering zone (III), not only is the SIM transformation still occurring, but specific martensite variants also start to elastically and eventually plastically deform. Plastic deformation is accompanied by martensite stabilization, which is undesired in terms of SE due to the incomplete restoration of the initial austenitic structure; therefore, it must be avoided for SE assessments due to its deteriorating effects [48].

In this study, certain parameters, namely SIM stress, transformation strain (ε_T), superelastic strain (ε_S), elastic strain (ε_e), and the retained strain (ε_R) are all extracted from the curves in each successive cycle to be able to quantitatively discuss and justify the dissimilarities considering different samples and deformation modes. It should be noted that the critical stress for the transformation was estimated by the intersection of two tangent lines connecting the linear elastic and the semi-plateau regions of the curves, as is depicted in Figure 3-4.

For further microstructural characterizations, a JEOL JSM-7000F SEM, fitted with a Schottky field emission gun (FEG) and an Oxford electron backscatter diffraction (EBSD) detector, operating at an accelerating voltage of 20kV, was utilized. For EBSD sample preparation, specimens were ground with SiC abrasive papers with grit sizes of 800-4000 and subsequently polished with 3-0.1µm diamond pastes. As a final step, a 0.02µm colloidal silica suspension was used to obtain a mirror-like surface with low residual stresses, enabling the capture of high-quality Kikuchi patterns for further indexing. The acquired raw data were post-processed using both AZtecCrystal and Channel5 software.

In order to investigate the formation of precipitates and observe the state of the dislocations, transmission electron microscopy (TEM) images and selected area electron diffraction (SAED) patterns were obtained using a Thermofisher Scientific Talos 200X TEM, equipped with a FEG source and an electron energy loss spectrometer (EELS), operating at 200kV. The collection angle and convergence angles during examinations were 10.5 and 30mrad, respectively. TEM samples were prepared by a Thermofisher Scientific Helios G4 dual beam plasma focused ion beam (PFIB), which employs a Xe^+ plasma during the milling process.

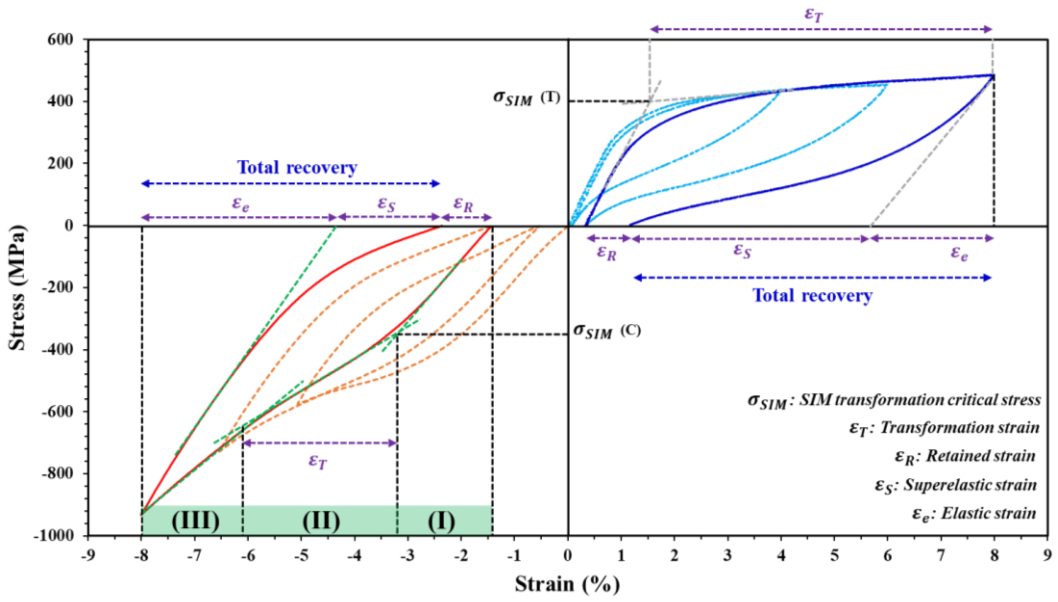

Figure 3-4 An overall presentation of the conducted cyclic loading-unloading tensile and compressive tests and the employed methodology to estimate the asymmetry parameters.

3.3 Results

3.3.1 Superelastic behavior in compressive mode

The cyclic compressive superelastic responses of all the post heat-treated samples were examined by step-by-step incremental loading/unloading stages, and the acquired stress vs. strain curves are demonstrated in Figure 3-5 for all specimens.

As shown, the strain was incrementally increased during loading in each step by a value of 2%, resulting in six load/unload cycles and a final accumulated strain of 12%. A quick inspection of the curves indicates that the samples heat treated at the lower temperature do not show the favorable superelastic hysteresis, and severe strain hardening is observed when the cycling progresses. Strain hardening occurs due to the increased activity of the slip systems, the multiplication of the dislocations, and the generation of new lattice defects in successive cycles [59]. On the other hand, aging at 550°C could result in higher recovery and a distinct transformation plateau. Evidently, the lower temperature of 450°C was not

high enough to provide the required driving force to stimulate the restoration mechanisms and promote the formation of the precipitates. To have a better understanding of the curves, firstly, the aforementioned strain values, namely ε_R, ε_S, and ε_e, are estimated and extracted from the curves, and the results are presented in Figure 3-6.

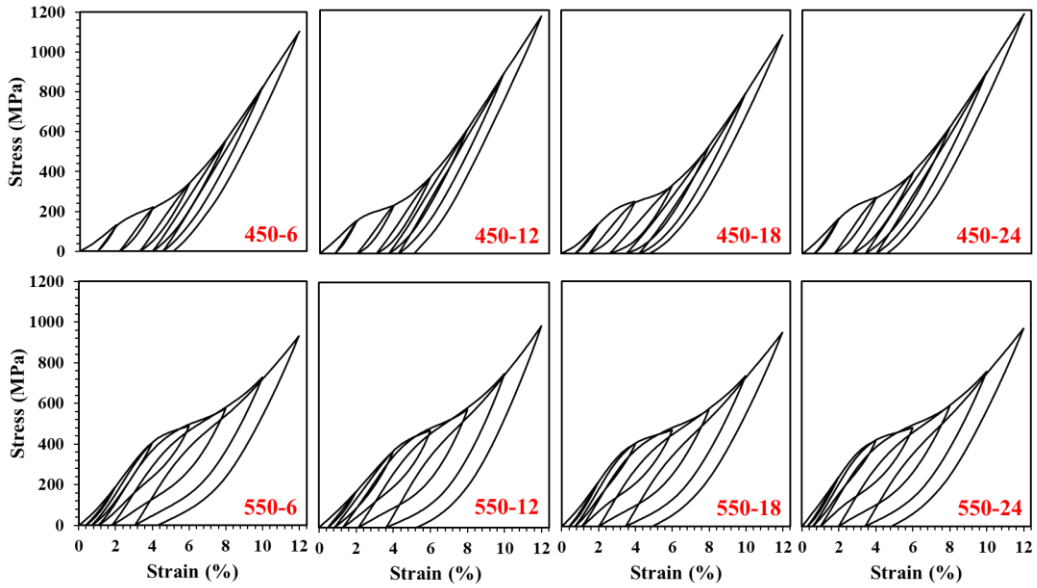

Figure 3-5 Cyclic loading/unloading compressive behavior of LPBF processed samples aged at different temperatures and durations, as denoted on the figures by red labels.

According to Figure 3-6(a), for the samples heat treated at 450°C, elastic recovery plays the dominant role in restoring the initial shape, and superelastic recovery has a minor effect. By continuing the cycles, both of these values increase, corresponding to the higher applied load, but it is only for samples heat treated for longer durations of 18 to 24 hours that the superelasticity starts to meaningfully increase, denoting that the microstructure requires prolonged annealing times to evolve when heat treatment is performed at lower temperatures. The highest strain recovery of 7.43% in the 6th cycle was obtained for sample 450-24, in which strain values of 5.32% and 2.11% were recovered due to elasticity and SE, respectively.

In comparison with the values extracted for the other set of samples aged at 550℃, represented in Figure 3-6(b), in which significantly higher recovery occurred due to SE according to the green sections of the columns, one can conclude that the prerequisites of SE enhancements can be better met during annealing at 550℃, even when heat treatment is conducted for shorter periods.

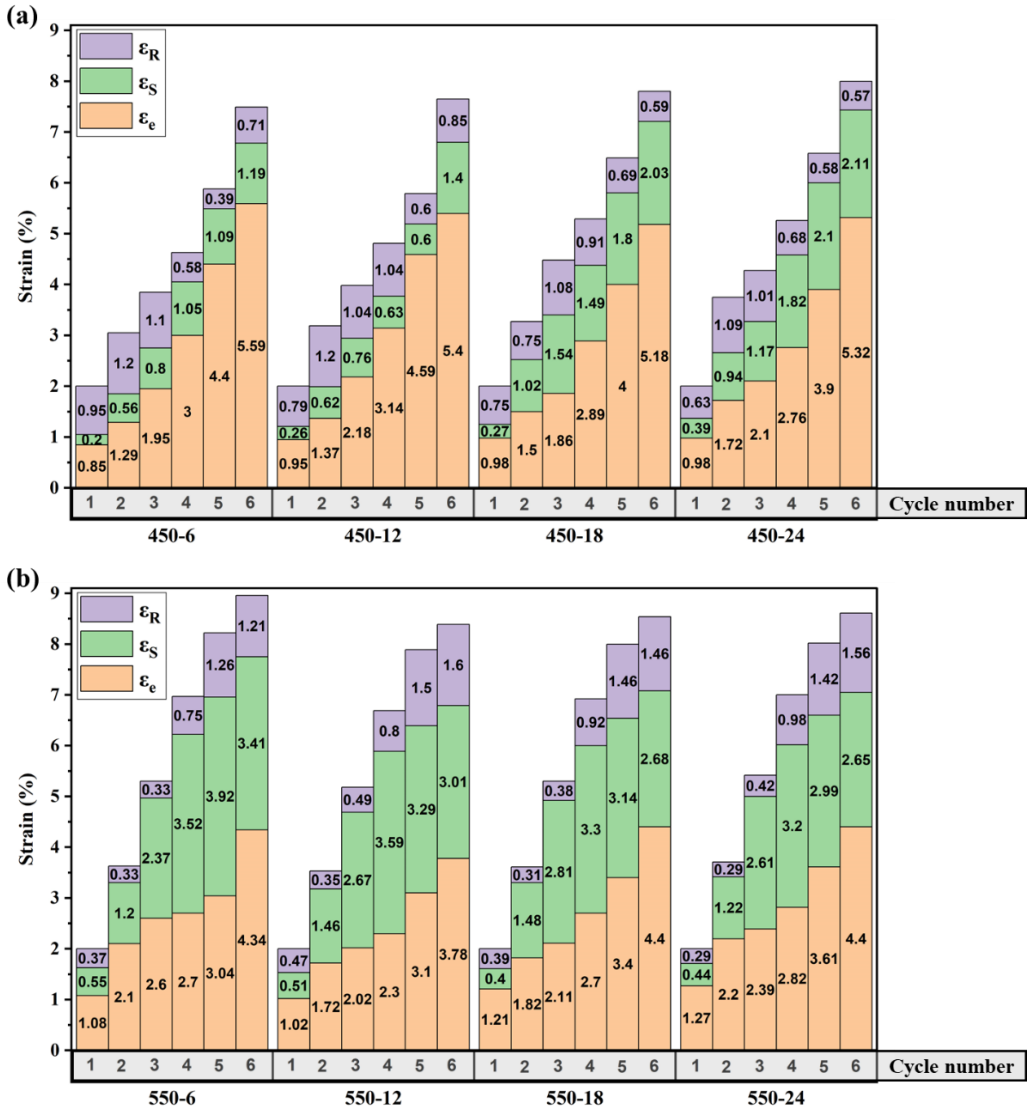

Figure 3-6 The measured retained strain (ε_R), superelastic strain (ε_S), and elastic strain (ε_e) during compressive cyclic testes of samples heat treated at (a) 450 and (b) 550℃ for 6, 12, 18, and 24 hours.

It should be noted that the sum of all the three mentioned strain values results in the total accommodated strain during a selected cycle, which can also be perceived by the diagrams represented in Figure 3-4. The higher total accommodated strain in samples treated at high temperatures denotes that the SIM transformation was actively involved during the deformation. In this regard, the highest recovery was recorded for the specimen aged at 550℃ for 6 hours (i.e., 550-6), amounting to 7.75% strain, from which the strain value of 3.41% was recovered due to superelasticity. This high value of total recovery is significant compared to the previous studies and is comparable to the highest reported strain recoveries of around 8% for conventionally processed samples by a series of cold work and annealing steps [19,60,61]. The other samples treated for extended periods do not show this superior recovery, which is believed to be the effects of enlargement of the Ni_4Ti_3 precipitates, loss of precipitates' coherency, and grain growth mechanisms [62]. In other words, in order to gain the optimum SE behavior, $Ni4Ti_3$ precipitates should be in nano sizes and have a coherent interface with the matrix to act as effective obstacles, hindering the dislocation motion and facilitating the occurrence of the SIM transformation [63]. Furthermore, other precipitates such as Ti_2Ni_3 and $TiNi_3$ might also form during prolonged annealing, which are not as effective as the intermediate Ni_4Ti_3 phase in enhancing the SIM transformation. In conclusion, the acquired evidence suggests that the temperature of 450℃ is not high enough to result in favorable microstructural evolutions, namely the formation of Ni_4Ti_3 precipitates and the occurrence of the restoration mechanisms, in the context of enhancing the SE behavior. Therefore, relatively better SE behavior is only observed for samples kept at 450℃ for a more extended period. In contrast, for the series that was heat treated at 550℃, 6 hours was enough to stimulate the formation of desired precipitates and statically restore the microstructure leading to the highest recoverability. Further information will be

provided on the microstructure of the optimum sample, i.e., 550-6, in the following section, justifying the acquired enhanced SE behavior.

3.3.2 Microstructural characterization of the optimum sample

The acquired EBSD inverse pole figure (IPF) map for sample 550-6 that demonstrated a superior SE response is depicted in Figure 3-7(a) along the building direction. As is apparent in this figure and emphasized in Figure 3-7(b) by the illustrated IPF triangle, the sample is highly textured in directions close to <001>||BD, which is expected for most metallic materials processed by the LPBF process. This preferred texture is indexed by "1" in the figure. During rapid epitaxial solidification throughout the building process, grains tend to orient and grow towards the direction offering the highest heat flow, which in LPBF translates to the formation of grains elongated in the direction of the laser source. However, another texture component is also observed in the IPF triangle, marked by "2", which indicates a considerable number of grains were tilted to directions closer to <111>||BD. The addition of this texture component is believed to be the aftereffect of the restoration processes and, in particular, static recrystallization (SRX). As was mentioned earlier, for conventionally processed NiTi alloys which are treated by a series of cold working and annealing processes, the grains are generally formed in <111> and <110> directions.

For further scrutiny, the restoration maps were extracted from the EBSD data, as is shown in Figure 3-7(c), which reveals the involvement of the restoration phenomenon. In order to acquire recrystallized fraction maps using Tango-Channel5 software, all grains are initially reconstructed based on a defined misorientation angle (10^{o}), and then the internal misorientation angle of subgrains within each grain is also measured and compared to the defined subgrains' misorientation angle (5°). If that average misorientation angle in a single grain exceeds 5^{o}, the grain is classified as deformed. However, if there are grains that their

internal misorientation angle is lower than the defined critical value, but the average misorientation from subgrain to subgrain within that selected grain is above the critical value, the grain can be classified as substructured. Otherwise, grains are recognized as recrystallized. Evidently, recovery and recrystallization both played an imperative role during the processing of sample 550-6. By comparing the IPF map in Figure 3-7(a), the restoration map in Figure 3-7(c), and the kernel average misorientation (KAM) map in Figure 3-7(d), it is evident that a high number of grains in the microstructure which are oriented toward <001>||BD are mostly having a strong substructure that are affected by recovery. In contrast, for other areas which are aligned to directions closer to <111>||BD, recrystallization played the dominant role. In other words, red grains in the IPF maps are observed by a yellow color, defining recovery, while blue grains in the IPF maps are also colored blue in the restoration map, denoting recrystallization. Additionally, the share of low angle grain boundaries (LAGB) and high angle grain boundaries (HAGB) in the final evolved microstructure, and the restored fraction of the microstructure, either recovered or recrystallized, are represented in Figure 3-7(e). As was proved by the authors in a previous study, dynamic recovery (DRV) is actively involved during the LPBF processing of NiTi alloys resulting in dislocation annihilation, rearrangement, and the formation of substantial subgrains or LAGBs [40]. However, during the aging treatment performed in this study, static restoration came into effect, and static recrystallization contributed to the formation of equiaxed fresh grains having HAGBs. Consequently, based on Figure 3-7(e), when the fraction of grain boundaries and restored microstructure is compared for the same sample before and after the annealing treatment, it is clear that the fraction of LAGB was severely decreased during annealing, and the fraction of recrystallized grains was increased from 6.6% to 41.9%. By referring to these measurements, it can be concluded that for the treated

sample, nearly half of the boundaries are LAGB, in which dynamically recovery grains were formed during the LPFB process, and the other half consists of HAGB and recrystallized grains, formed during aging due to the occurrence of static recrystallization.

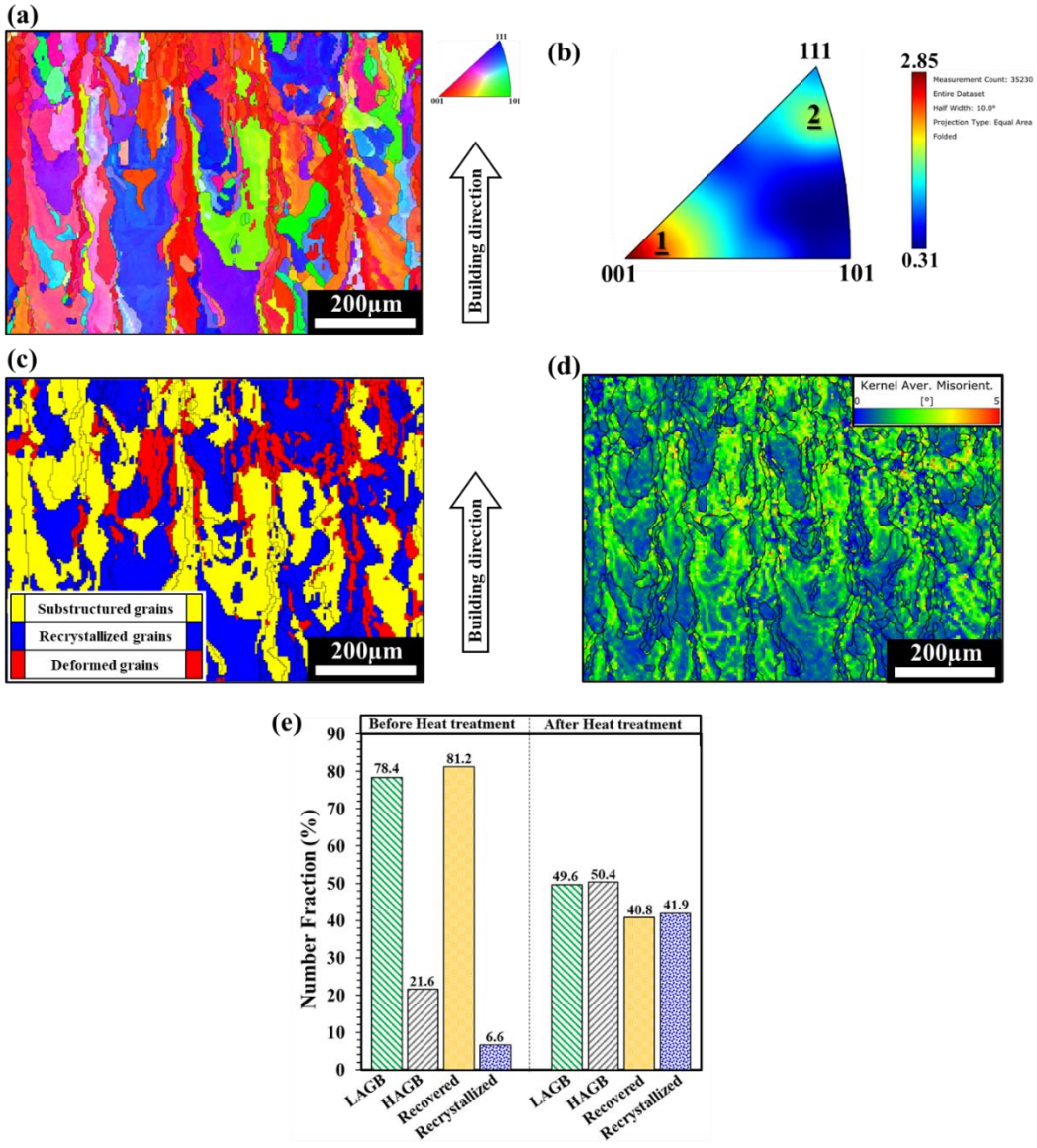

Figure 3-7 The acquired EBSD (a) IPF map, (b) IPF unique triangle||BD, (c) recrystallization fraction map, (d) KAM map, and the (e) comparison of the estimated share of LAGB, HAGB, and the grain fractions affected by either recovery or recrystallization (before and after heat treatment) for sample 550-6.

The involvement of the restoration mechanisms is particularly important due to their imperative role in governing the SE behavior. The transformation mobility is severely restricted for structures having very high dislocation densities, dislocation tangles, and residual stresses in their structure, resulting in the deterioration of the superelastic behavior (e.g., in cold worked structures) [28]. However, by the further progression of the restoration mechanisms during post annealing, the dislocation density is decreased, and fresh grains are formed which leads to higher strain accommodation during the SIM transformation and thus having a higher probability for enhanced superelasticity [57,64]. It should be noted that these mechanisms are only capable of facilitating the occurrence of the transformation and superior elasticity cannot be achieved for such structures without the involvement of precipitation. The improvement of SE properties for conventionally fabricated NiTi alloys that experienced restoration mechanisms during processing was also reported by others in the literature.

As mentioned earlier, an austenitic superelastic NiTi alloy experiences four stages during loading, from which the second stage was correlated to the SIM transformation. However, if the critical resolved shear stress (CRSS) for the activation of slip mechanisms decreased to a level in which it goes below the SIM critical stress, the austenite phase will not undergo the SIM transformation, and straightly after elastic deformation, plastic deformation of austenite occurs. Such behavior is usually witnessed for solutionized NiTi alloys. Therefore, the role of precipitates to increase the CRSS and hinder the slip mechanisms becomes highly significant. In this regard, lenticular Ni_4Ti_3 precipitates formed in the early stages of the aging process are the most effective barriers to dislocation motion due to their shape factor, small size, and distribution throughout the microstructure. These precipitates can only be seen by detailed TEM studies, which form the basis of the following discussion.

The TEM images and SAED patterns acquired from sample 550-6 are demonstrated in Figure 3-8. As it is evident, the matrix consists of an austenitic B2 parent phase, which is expected since the M_s transformation was lower than the room temperature to promote the formation of any martensite variants. Detailed observation indicates that some areas are relatively dislocation free while others include dense dislocation networks and dislocation tangles. During the LPBF process, different regions of the samples are not affected by the same temperature field, causing the generation of dissimilar levels of stresses and dislocations in the sample's microstructure. As a result, the driving force for the occurrence of different restoration mechanisms is not equal in all areas, leading to microstructures consisting of both recovered and recrystallized grains. The observed EBSD recrystallization maps are accordingly justified in which either the involvement of recovery or recrystallization mechanism was dominant in determining the final microstructure.

Furthermore, TEM images in Figure 3-8(b, c) reveal a uniform distribution of a particular lenticular phase in the austenitic matrix, which exhibits a remarkable resemblance to the desired Ni_4Ti_3 precipitates. Further EELS quantitative analysis confirmed the chemical composition of this phase to be Ni_4Ti_3 precipitates. The existence of these precipitates for a heat treated NiTi alloy is accompanied by the formation of an intermediate trigonal phase, introduced as the R-phase, in the vicinity of precipitates. Wang et al. [65,66] reported that the presence of R-phase as an intermediate phase is expected for structures having coherent Ni_4Ti_3 precipitates along with dislocation networks, induced by different heat treatment procedures such as aging. For further verification, SAED patterns were acquired from the area marked by the yellow circle in Figure 3-8(b) and the indexed results are represented in Figure 3-8(d). Accordingly, the matrix consists of an austenitic B2 parent phase, while diffraction spots related to the presence of the R-phase in areas adjacent to the precipitates

are also detected. As is illustrated in Figure 3-8(c), other than the lenticular Ni_4Ti_3 precipitates, another unknown nearly spherical phase is also observed in the TEM images necessitating further investigation.

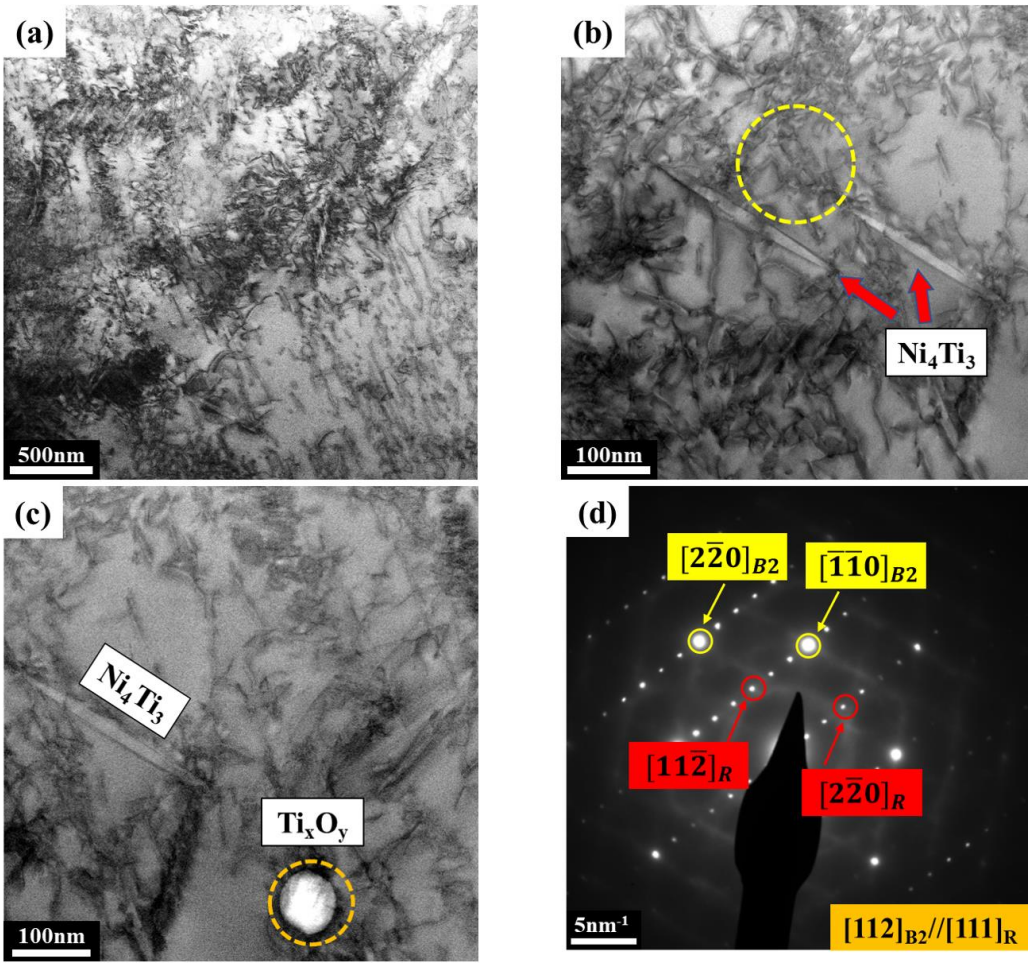

Figure 3-8 (a-c) TEM images obtained from sample 550-6, revealing areas with high density of dislocations, the lenticular Ni_4Ti_3 precipitates, and Ti-oxides inside the structure, and (d) SAED pattern obtained from the area pointed out by yellow circle in (b).

The high angle annular dark field (HAADF) image and EELS maps acquired from this area of interest are represented in Figure 3-9. The EELS maps in Figure 3-9(b) reveal that these unknown phases have a Ti_xO_y composition in which quantitative analysis indicates that

$x = y$. The presence of these oxides is related to either the LPBF process, which occurs at a very high oxidation-prone temperature or the powder feedstock itself. Although the chamber is filled with inert gas, there is still minimal traces of oxygen, either in the chamber or the powder particles (entrapped during atomization), which could react with the susceptible titanium element, mainly in areas where Ni was evaporated, to form such oxides. Some studies suggested that the presence of these oxides can be effectively controlled to obtain a relatively decent SE response for as-built materials [42]. Nonetheless, superior SE is only achieved when Ni_4Ti_3 precipitates are present in the microstructure, hindering the dislocation motion and facilitating the occurrence of the SIM transformation. In conclusion, the observed enhanced SE response for sample 550-6 is attributed to its fully austenitic matrix, which consists of a fair distribution of favorable Ni_4Ti_3 precipitates, dynamically recovered substructure, and statistically recrystallized grains.

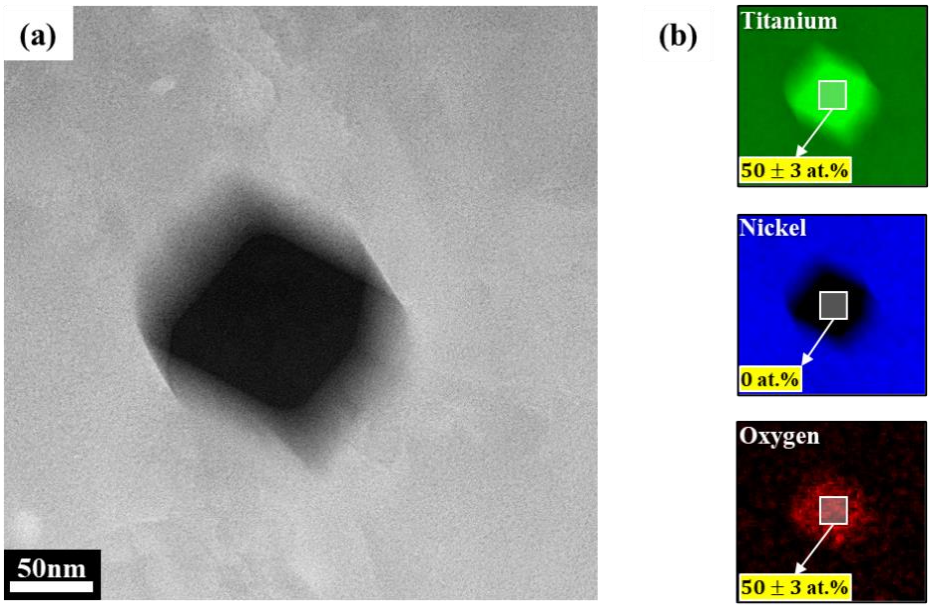

Figure 3-9 The acquired HAADF image of the unknown phase and the (b) EELS maps revealing the distribution of Ti, Ni, and O elements.

3.3.3 Asymmetrical superelastic behavior of sample 550-6

It was shown that the compressive SE behavior of the as-built NiTi alloy was significantly improved for sample 550-6, which was heat treated at 550℃ for 6 hours, owing to the presence of fine precipitates and a restored microstructure. However, to thoroughly understand the SE behavior, the tensile cyclic response of the sample having enhanced recoverability in compression should also be examined. This comparison is imperative due to the service conditions of many NiTi's applications, in which different deformation modes are involved.

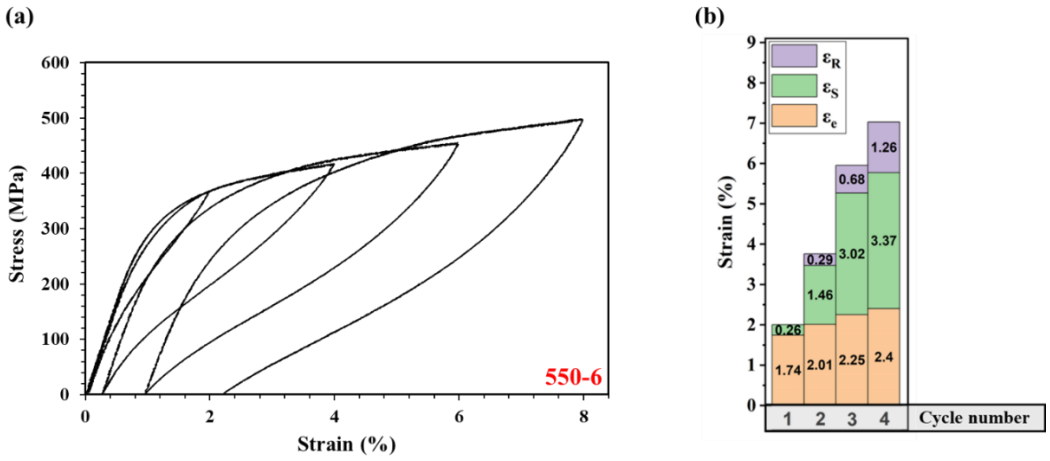

Figure 3-10 (a) Cyclic tensile load-unload behavior of sample 550-6, and the (b) estimated values of retained strain, superelastic strain, and elastic strain in each cycle.

To that end, the tensile cyclic loading-unloading curves for sample 550-6 is plotted in Figure 3-10(a). The sample was strained in 4 repetitive cycles, adding a strain value of 2% in each cycle, amounting to 8% total strain. Further straining was prevented to avoid plastic deformation and fracture. As is apparent, the curves exhibit different behavior in cyclic tensile testing compared to the previously shown compression curves, denoting the asymmetric behavior of the material. The estimated values of ε_R, ε_S, and ε_e are also

represented in Figure 3-10(b), which shows that all these values are increasing by continuing the deformation. However, according to the figure, it is clear that SE plays the dominant role in facilitating the shape recovery. In this regard, for the 4th cycle, a strain value of 5.77% was recovered, from which 2.4% strain was retrieved due to elasticity, while superelasticity resulted in 3.37% recovery. In comparison with the compressive cyclic response shown in Figure 3-6(b), for the 4th cycle, sample 550-6 demonstrated 2.7% and 3.52% recovery due to elasticity and SE, respectively, resulting in a total strain recovery of 6.22%.

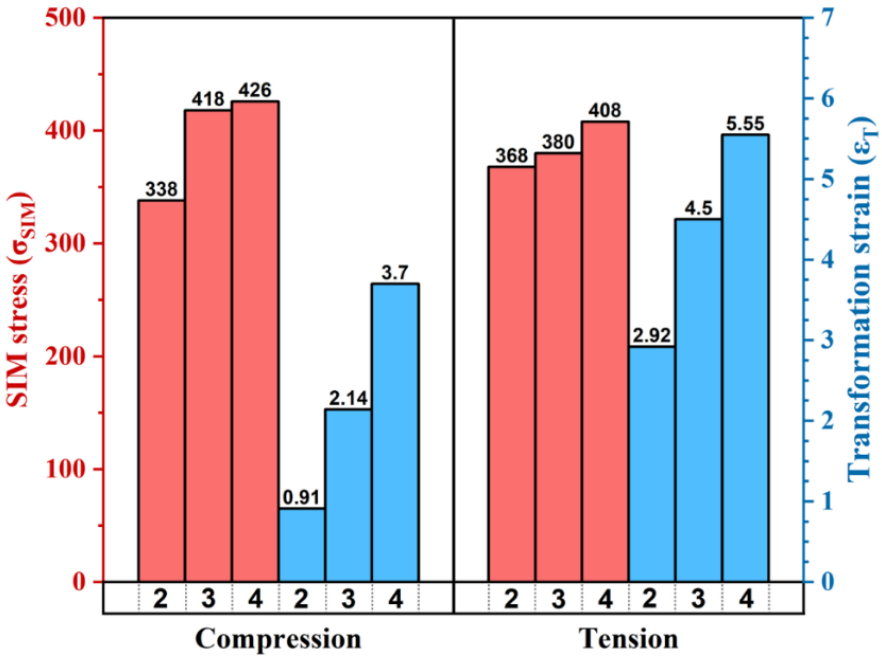

Figure 3-11 The estimated values of SIM stress and transformation strain for sample 550-6, obtained from cyclic loading-unloading compression and tension curves.

To investigate the asymmetric properties of the optimum sample, the two aforementioned most critical asymmetry parameters, namely SIM stress (σ_{SIM}) and transformation strain (ε_T), were extracted from both tension and compression graphs, and the results are represented in Figure 3-11. As is shown, the first cycle was omitted from the calculations

since the SIM transformation begins to effectively occur from the second cycle, and subsequently, higher values of strains are accommodated starting from the second cycle. As is apparent, the required stress to initiate the SIM transformation is higher in compression, while transformation strain is considerably lower. The underlying reasons for such a behavior are scrutinized and discussed in section 3.4.

3.3.4 The effect of scanning strategy on the asymmetrical behavior

It was proven that the crystallographic texture of the material plays a vital role in governing the parts' behavior in tensile and compressive deformation modes. In the previous sections, an alternating x-y scanning path in which the laser direction rotates 90^{o} consecutively was employed for the LPBF process. The results indicated that while the fabricated parts were mainly texturized in <001>||BD, the involvement of the recrystallization mechanism could contribute to the changes in the grain orientations to directions closer to <111>||BD. In LPBF processing, the material's texture can be altered and manipulated by incorporating alternative scanning strategies. Thus, an alternating x-y scanning path with a rotation angle of 67^{o} was utilized to investigate the effects on texture and the asymmetry parameters.

Figure 3-12(a, b) demonstrates the cyclic behavior of a sample manufactured using this scanning strategy and was post heat treated at 550℃ for 6 hours. For simplicity and brevity, this sample is labeled as 550-6-67 compared to the optimum sample produced using 90^{o} as the rotation angle (coded as 550-6-90 hereinafter). When these two samples are compared, 550-6-67 represents a much higher tensile strain recovery in the fourth cycle, showing 6.85% recovery, from which 2.14% and 4.71% strain values were recovered due to elasticity and SE, respectively. Sample 550-6-90 only showed a total recovery value of 5.77% in cyclic tensile tests. On the other hand, when the compressive behaviors of the samples are compared, an opposite trend is observed in which total strain recovery for 550-

6-67 in the 6th cycle is approximately 7.17% (3.05% SE recovery), but sample 550-6-90 exhibited 7.75% recovery.

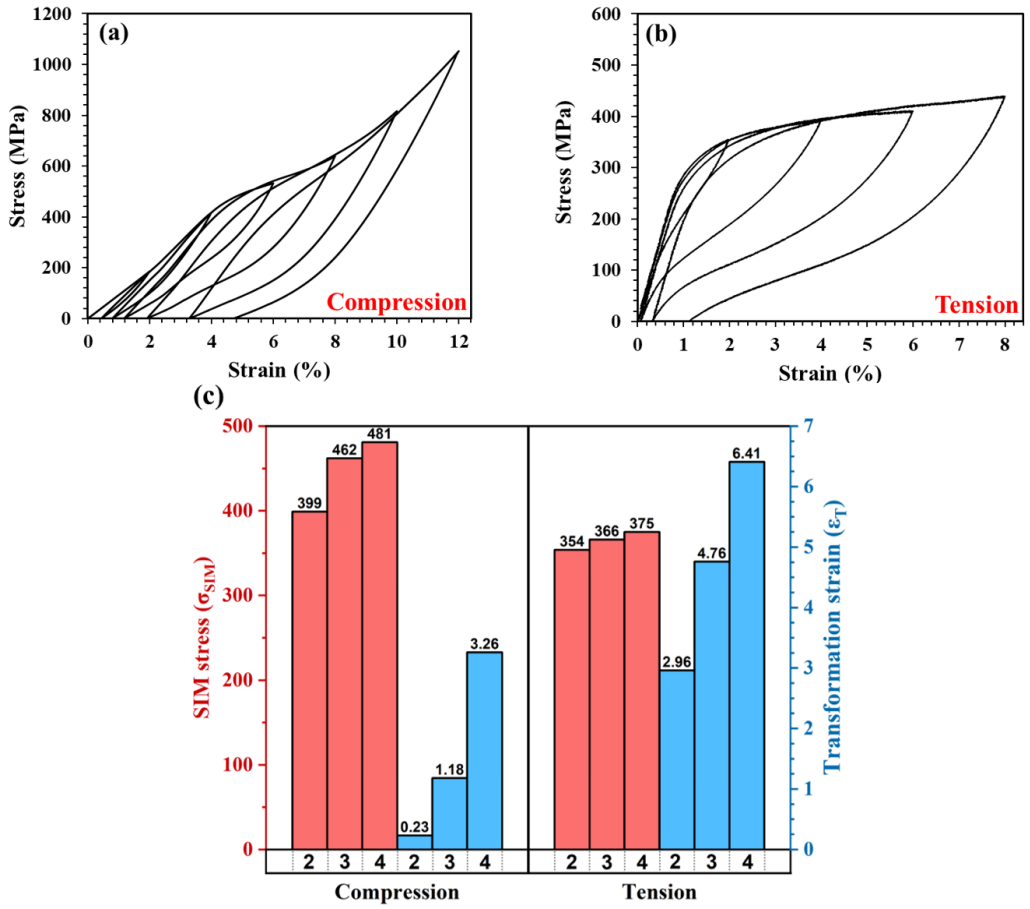

Figure 3-12 The cyclic behavior of sample 550-6-67 during (a) compression and (b) tension tests, and (c) the estimated SIM stress and transformation strain values in cycles 2-4.

Therefore, it can be concluded that 550-6-90 has superior SE properties in compression while 550-6-67 demonstrated higher SE recoverability in tension. The estimated values of SIM stress and transformation strain were also extracted, as illustrated in Figure 3-12(c). Accordingly, sample 550-6-67 exhibits a higher level of asymmetry, and the differences between stresses and strains are much higher in this sample compared to 550-6-90. To

discuss these differences, the microstructure of sample 550-6-67 was studied, resulting in Figure 3-13.

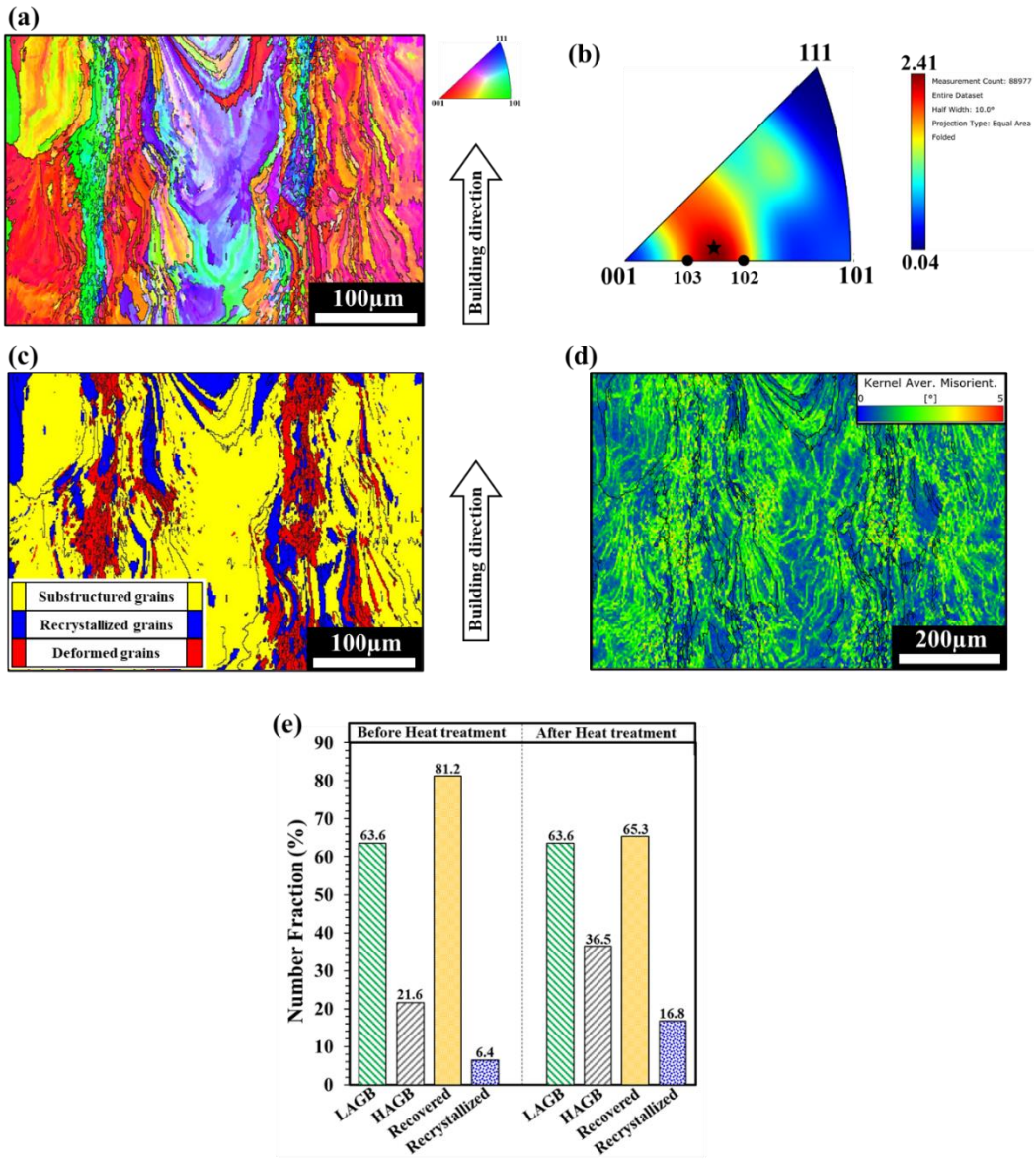

Figure 3-13 The IPF (a) map and (b) unique triangle for sample 550-6-67 in a direction parallel to the BD, and the (c) restoration map, (d) KAM map, and (e) fractions of LAGB, HAGB, and grains affected by recovery or recrystallization (before and after the aging treatment).

According to Figure 3-13(a, b), grains are still oriented to orientations closer to <100>||BD, but the overall texture intensity represents an inclination toward <103> and <102> directions, as is denoted in the figure. The development of such a texture component is believed to be the effect of the scanning strategy. When the laser path rotates 67º in each cycle, as opposed to 90º, the path for each scan is shorter due to the placements of the parts parallel to the recoating direction on the building platform. These shorter scanning paths result in lower heat accumulation in consecutive layers during the LPBF process, preventing a full grain growth process and grain reorientation toward the <100> direction [34].

The restoration and KAM maps for sample 550-6-67 is presented in Figure 3-13(c) and Figure 3-13(d), respectively, and the fractions of LAGB, HAGB, and restoration phenomena are plotted in Figure 3-13(e), revealing the state of the microstructure before and after the heat treatment. Interestingly, by conducting the heat treatment, this sample still consists mainly of recovered grains and subgrains, and recrystallization was involved in less than 17% of the microstructural evolution. Although some partially recrystallized grains were formed during aging, static recovery seems to be the dominant mechanism for 550-6-67. This observation can be justified by the decrease in the heat accumulation discussed above, resulting in lower residual stresses when the direction of the laser path rotates 67º compared to 90º [52]. Consequently, as is evident, the driving force is not high enough for the as-fabricated sample to substantially experience the occurrence of the static recrystallization in the subsequent heat treatment for 550-6-67.

3.4 Discussion

In order to be able to discuss and justify the observed differences in the values of SIM stresses and transformation strains in each deformation mode and for samples fabricated by two different scanning strategies, underlying theories related to the (a) Schmid's law [24,30] and (b) lattice distortion model [27,67] are utilized. In the SIM transformation, different twin-based martensitic variants may form based on the crystallographic orientations of the grains relative to the loading direction. It should be noted that amongst three possible twinning systems in NiTi alloys, namely type I, type II, and compound twins, only the activity of type II twinning mode is considered. This twinning system has been recognized by various studies as the dominant twinning mode in NiTi alloys, playing a dominant role in the SIM transformation during the cyclic deformation of the material [68].

Based on crystallographic relationships and detailed TEM studies, it has been well established that the shearing system of {-0.86 0.26 0.41} <0.45 0.77 0.44> is capable of creating the optimum shearing angle for type II twinning modes [68–70]. Accordingly, this shearing system was nominated for calculating the Schmid factors (SF) of different orientations based on the Schmid's law. According to Schmid's law, the mentioned twinning system requires a certain amount of stress to be activated depending on the crystal orientation and the loading direction. In other words, SF governs the occurrence of the SIM transformation, and the higher the SF, the lower the required stresses to initiate the occurrence of the SIM transformation. It should be noted that for different deformation modes, the value of the maximum resolved shearing factor is dissimilar due to the possibility of the formation of various martensite corresponding variant pairs (CVPs).

On the other hand, the lattice distortion model states that during the transition from an austenitic B2 crystal structure to a monoclinic B19' martensite correspondence variant, a certain level of strain or distortion can be accommodated along the loading direction. In this regard, the martensite variant capable of resulting in the highest level of strain accommodation towards the LD has the maximum driving force to form.

Previous studies [26,27] considered various crystallographic orientations and different martensite CVPs and compared the values of the Schmid's factor and the accommodated transformation strain for tensile and compressive modes of deformation, which are summarized in Figure 3-14 by the illustrated IPF unique triangles for different crystallographic orientations. Figure 3-14(a) depicts the differences between the SF values for different crystallographic orientations in a direction parallel to the LD, revealing that orientations closer to <100>||LD have a higher SF value in compression, while this value is higher in tension for directions closer to <111> and <110>. The black line in the middle denotes that the SF values in both deformation modes are equal.

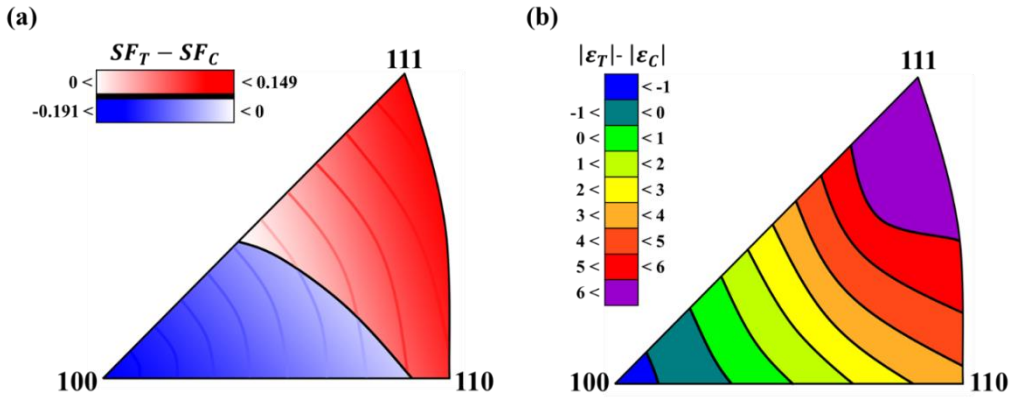

Figure 3-14 The difference between tensile and compressive (a) Schmid factors, and (b) transformation strains, plotted in an IPF unique triangle for different crystallographic orientations || LD. These values are extracted based on previous studies by Mao [26,30] and Bucsek [27], respectively.

Furthermore, Figure 3-14(b) demonstrates the difference between the transformation strain in tensile and compressive loads, and as is shown, the IPF triangle is sectioned into nine different zones. As is illustrated, higher transformation strain is accommodated in tension for materials having grains aligned to <111>||LD, while preferred reorientation towards <100>||LD can result in higher transformation strains in compression.

Now that the underlying reasons for the asymmetric behavior and its dependency on the crystal orientation have been discussed, the differences in the values of SIM stress and transformation strain for sample 550-6-90 in tension and compression, illustrated previously in Figure 3-11, can be justified. The IPF unique triangle for sample 550-6-90 in a direction parallel to the loading direction is plotted in Figure 3-15(a). It is worth mentioning that this IPF||LD, is different from the previously shown IPF||BD for the same sample since the loading direction is perpendicular to the building direction during the LPBF process. Therefore, it can be seen that the grains are oriented toward directions closer to <112> and <113> parallel to the LD, contributing to the increase of texture intensity in these orientations. This IPF was then superimposed on the calculations previously shown in Figure 3-14 for SF and transformation strain, and the results are demonstrated in Figure 3-15(b) and Figure 3-15(c), respectively. Looking at the superimposition of the IPF and SF map (Figure 3-15b), the triangle is divided into two regions, where (I) SF in tension is higher than compression, or (II) SF is lower in tension. The black line in the middle stands out for orientations resulting in the same value for SF. The material is textured mainly in directions where SF values are equal in both deformation modes, and there is only a slight difference between the two. However, a considerable number of grains are inclined to directions closer to <100> where SF is higher in compression. Based on this figure, it can be concluded that the SIM stresses should be relatively the same in different deformation

modes or, at the very least, be higher in tension. This is in fact true for the SIM stress values recorded for both tension and compression plotted in Figure 3-11. Furthermore, the compressive SIM stress is only lower in the second cycle, but it supersedes the recorded tensile SIM stress values in the consecutive cycles. It is believed that this increase in SIM stress in compression is mainly due to the involvement of the slip systems, strain hardening mechanism, and the interaction between the SIM transformation and the dislocation slip. Such an interaction could hinder the movement of the transformation front, leading to higher required stresses for further progression of the SIM transformation. On the other hand, according to Figure 3-15(c), the main texture component is placed in zone (II), where the transformation strain is higher in tension, which justifies the recorded higher tensile transformation strain values in Figure 3-11 in comparison to the compressive mode. Generally, most crystal orientations are placed in zone II, and only a few crystallographic orientations, marked zone (I), can provide higher strains in compression when the transformation from the austenite phase to a selected martensite CVP is considered. Furthermore, the activation of the slip mechanisms and the increase in the slope of the stress-strain curve could similarly limit the transformation strain.

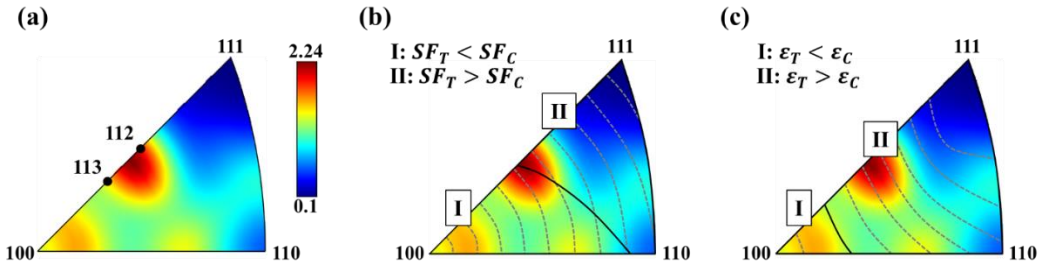

Figure 3-15 (a) the acquired IPF triangle for sample 550-6 in a direction || LD, and its superimposition on (b) Schmid factor and (c) transformation strain IPFs for different crystallographic orientations, divided into regions I and II.

The IPF triangle obtained from sample 550-6-67 is also depicted in Figure 3-16(a), which reveals that the sample is highly textured in directions closer to <111>||LD. It can be seen that in addition to an incomplete rotation toward the <001>||BD, a high texture intensity in the <111>||LD has been developed, justifying the observed differences between the SIM stresses and transformation strains shown previously in Figure 3-12(c). According to the guidelines represented in Figure 3-16(b, c), for orientations closer to <111>||LD, SF and transformation strains are much higher in tension in comparison with compression. These maps are perfectly consistent with the previous results in which higher SIM stresses were recorded in compression, while transformation strains were much higher in tension. Furthermore, since nearly all the grains are placed in region (II) of the IPF triangles, the asymmetric behavior is also intensified.

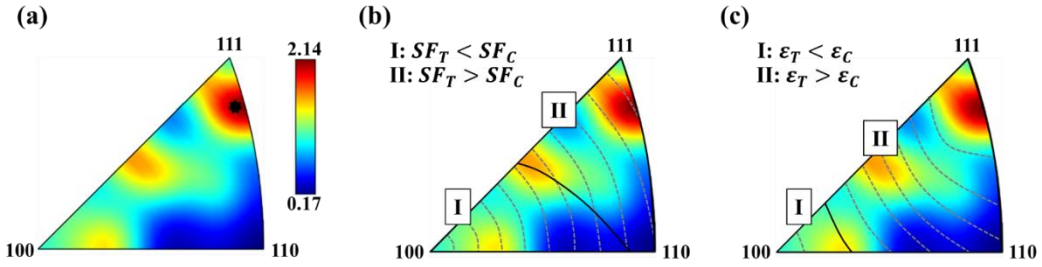

Figure 3-16 The (a) IPF triangle for sample 550-6-67 in a direction || LD and the superimposition of this figure on (b) SF and (c) transformation strain IPF guides.

Before being able to conclude the discussions related to SE and asymmetrical properties, the DSC curves for both 550-6-90 and 550-6-67 should also be viewed and compared since transformation temperatures govern the occurrence of the $A \leftrightarrow M$ transformation at test temperature. As is demonstrated in Figure 3-17, the transformation temperatures for both samples were higher than the as-received powder, which is due to the formation of Ni_4Ti_3 precipitates and Nickel depletion in the matrix. Moreover, for both samples, the A_f temperature was well below the room temperature, meaning that both samples can exhibit

ideal SE behavior at room temperature. Although the transformation temperatures are relatively similar when both samples are compared, the peaks in sample 550-6-67 are sharper, which further justifies the lower residual stresses in this sample and the higher mobility of the A/M interface.

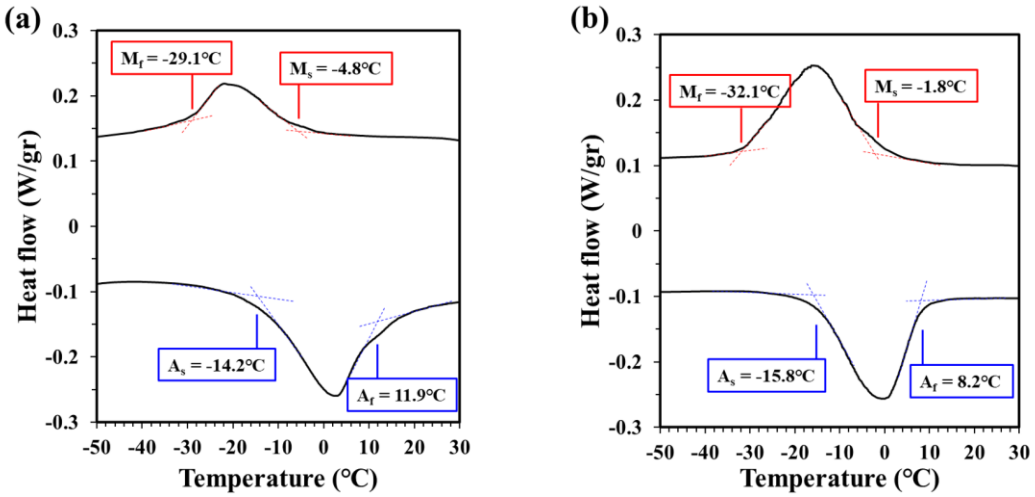

Figure 3-17 The DSC curves obtained from sample (a) 550-6-90, and (b) 5506-6-67, comprising of both cooling and heating cycles.

Ultimately, it can be concluded that the choice between the employed scanning strategy depends on the application of the material. For applications where the part is experiencing multiple modes of deformation and a lower level of asymmetry is preferred, 550-6-90 could yield better performance accompanied by an acceptable level of SE. In contrast, for achieving the highest strain recovery and superior superelasticity, mainly in tensile mode, sample 550-6-67 is better suited to offer the desired response.

3.5 Conclusion

An in-depth understanding of the asymmetrical behavior of aged additively manufactured NiTi alloys with optimum superelasticity in tensile and compressive deformation modes is imperative due to the vast application of this alloy in the biomedical industry and the fact

that nearly all parts experience multiple deformation modes during their service condition. In this paper, the authors utilized optimum LPBF processing parameters and scanning rotation angles of 90º and 67º to manufacture tensile and compression specimens, which were subsequently aged at temperatures of 450 and 550°C for 6, 12, 18, and 24 hours. Both SE response and asymmetric parameters of the processed samples were scrutinized and compared by conducting cyclic tensile and compressive tests, leading to the following conclusions:

- Aging at a lower temperature is unable to provide the required driving force for the precipitation and the occurrence of the restoration mechanism, while heat treatment at 550°C for only 6 hours can lead to the formation of nano-sized Ni_4Ti_3 precipitates and the occurrence of the recovery and recrystallization mechanisms, resulting in the highest strain recovery (i.e., 7.75% in the 6^{th} cycle).
- Employing a rotation angle of 90º during the LPBF process leads to a high texture intensity in directions close to the characteristic <001>||BD orientation. However, during the aging treatment, many grains were reoriented toward <111>||BD due to recrystallization, according to the acquired IPF and restoration maps.
- For the optimum samples fabricated by the LPF process, TEM images reveal the presence of nano-sized Ni_4Ti_3 precipitates and the formation of the R-phase in their vicinity, justifying the enhanced SE behavior of the sample aged at 550°C for 6 hours. In addition, some minor traces of titanium oxides (TiO) were also observed through chemical maps.

- All LPBF processed samples and subsequently aged exhibit an asymmetrical behavior in tension and compression. In this regard, the sample heat treated at 550℃ for 6 hours, manufactured using scanning rotation angles of 90º, shows higher SIM stress and considerably lower transformation strain in compression. These differences were justified by Schmid's law and lattice distortion theory. For this sample, although grains were oriented to <112> and <113>||LD, having relatively equal Schmid factors, the slip-SIM interactions led to higher SIM stress in compression. On the other hand, the distortion theory justified the accommodation of higher transformation strain in the tensile mode in comparison with compression.
- The scanning strategy is paramount and can affect the SE response of the sample in distinct deformation modes. The rotation angle of 67º results in superior strain recoverability during tension, but 90º exhibits better SE behavior in compression.
- By using a 67º rotation angle and subsequently aging at 550℃ for 6 hours, grains preferably reorient toward <103> and <102>||BD directions, and a high texture intensity is developed in <111>||LD. Furthermore, in 67º rotation angles, scanning paths are shorter, resulting in lower heat buildup and an incomplete grain growth toward <100>||BD. Additionally, the distances between laser scanning lines are decreased in consecutive layers, leading to lower heat gradients and residual stresses. Consequently, recovery mechanisms are dominant for a sample fabricated by 67º successive rotation angles.

- In conclusion, aging at 550℃ for 6 hours for a sample fabricated by a 90º scanning strategy can result in lower asymmetry and superior superelasticity in compression, while 67º plus heat treatment leads to the highest strain recoverability in tension, but an intensified asymmetric behavior.

3.6 References

[1] K. Otsuka, X. Ren, Physical metallurgy of Ti–Ni-based shape memory alloys, Prog. Mater. Sci. 50 (2005) 511–678. doi:10.1016/j.pmatsci.2004.10.001.

[2] J.P. Oliveira, R.M. Miranda, F.M. Braz Fernandes, Welding and Joining of NiTi Shape Memory Alloys: A Review, Prog. Mater. Sci. 88 (2017) 412–466. doi:10.1016/j.pmatsci.2017.04.008.

[3] B. Li, L. Wang, B. Wang, D. Li, J.P. Oliveira, R. Cui, J. Yu, L. Luo, R. Chen, Y. Su, J. Guo, H. Fu, Electron beam freeform fabrication of NiTi shape memory alloys: Crystallography, martensitic transformation, and functional response, Mater. Sci. Eng. A. 843 (2022) 143135. doi:10.1016/j.msea.2022.143135.

[4] W. Zhang, S.S. Ao, J.P. Oliveira, Z. Zeng, Z. Luo, Z.Z. Hao, Effect of ultrasonic spot welding on the mechanical behaviour of NiTi shape memory alloys, Smart Mater. Struct. 27 (2018). doi:10.1088/1361-665X/aacfeb.

[5] D. Stoeckel, A. Pelton, T. Duerig, Self-expanding Nitinol stents: Material and design considerations, Eur. Radiol. 14 (2004) 292–301. doi:10.1007/s00330-003-2022-5.

[6] K. Maleckis, E. Anttila, P. Aylward, W. Poulson, A. Desyatova, J. MacTaggart, A. Kamenskiy, Nitinol Stents in the Femoropopliteal Artery: A Mechanical Perspective on Material, Design, and Performance, Ann. Biomed. Eng. 46 (2018) 684–704. doi:10.1007/s10439-018-1990-1.

[7] A. Safdel, M.A. Elbestawi, Distortion and printability of stent structures in laser powder bed fusion processing of NiTi alloys, Mater. Lett. 300 (2021) 130163. doi:10.1016/j.matlet.2021.130163.

[8] T. Eliades, G. Eliades, a E. Athanasiou, T.G. Bradley, Surface characterization of retrieved NiTi orthodontic archwires., Eur. J. Orthod. 22 (2000) 317–326.

[9] F.J. Gil, M. Cenizo, E. Espinar, a. Rodriguez, E. Rúperez, J.M. Manero, NiTi superelastic orthodontic wires with variable stress obtained by ageing treatments, Mater. Lett. 104 (2013) 5–7. doi:10.1016/j.matlet.2013.03.135.

[10] N. Shayesteh Moghaddam, S. Saedi, A. Amerinatanzi, A. Jahadakbar, E. Saghaian, H. Karaca, M. Elahinia, Influence of SLM on compressive response of NiTi scaffolds, in: 2018: p. 13. doi:10.1117/12.2305251.

[11] M. Speirs, B. Van Hooreweder, J. Van Humbeeck, J.P. Kruth, Fatigue behaviour of NiTi shape memory alloy scaffolds produced by SLM, a unit cell design comparison, J. Mech. Behav. Biomed. Mater. 70 (2017) 53–59. doi:10.1016/j.jmbbm.2017.01.016.

[12] M.M. Barney, D. Xu, S.W. Robertson, V. Schroeder, R.O. Ritchie, a. R. Pelton, a. Mehta, Impact of thermomechanical texture on the superelastic response of Nitinol implants, J. Mech. Behav. Biomed. Mater. 4 (2011) 1431–1439. doi:10.1016/j.jmbbm.2011.05.013.

[13] M.H. Elahinia, M. Hashemi, M. Tabesh, S.B. Bhaduri, Manufacturing and processing of NiTi implants: A review, Prog. Mater. Sci. 57 (2012) 911–946. doi:10.1016/j.pmatsci.2011.11.001.

[14] H. Sehitoglu, J. Jun, X. Zhang, I. Karaman, Y. Chumlyakov, H.J. Maier, K. Gall, Shape memory and pseudoelastic behavior of 51.5%Ni-Ti single crystals in solutionized and overaged state, Acta Mater. 49 (2001) 3609–3620. doi:10.1016/S1359-6454(01)00216-6.

[15] K.F. Hane, T.W. Shield, Microstructure in the cubic to monoclinic transition in titanium-nickel shape memory alloys, Acta Mater. 47 (1999) 2603–2617. doi:10.1016/S1359-6454(99)00143-3.

[16] Y. Soejima, S. Motomura, M. Mitsuhara, T. Inamura, M. Nishida, In situ scanning electron microscopy study of the thermoelastic martensitic transformation in Ti–Ni shape memory alloy, Acta Mater. 103 (2016) 352–360. doi:10.1016/j.actamat.2015.10.017.

[17] H. Sehitoglu, I. Karaman, R. Anderson, X. Zhang, K. Gall, H.J. Maier, Y. Chumlyakov, Compressive response of NiTi single crystals, Acta Mater. 48 (2000) 3311–3326. doi:10.1016/S1359-6454(00)00153-1.

[18] X. Zuo, W. Zhang, Y. Chen, J.P. Oliveira, Z. Zeng, Y. Li, Z. Luo, S. Ao, Wire-

based directed energy deposition of NiTiTa shape memory alloys: Microstructure, phase transformation, electrochemistry, X-ray visibility and mechanical properties, Addit. Manuf. 59 (2022) 103115. doi:10.1016/j.addma.2022.103115.

[19] A. Safdel, A. Zarei-Hanzaki, A. Shamsolhodaei, P. Krooß, T. Niendorf, Room temperature superelastic responses of NiTi alloy treated by two distinct thermomechanical processing schemes, Mater. Sci. Eng. A. 684 (2017) 303–311. doi:10.1016/j.msea.2016.12.047.

[20] M. Es-Souni, M. Es-Souni, H. Fischer-Brandies, Assessing the biocompatibility of NiTi shape memory alloys used for medical applications, Anal. Bioanal. Chem. 381 (2005) 557–567. doi:10.1007/s00216-004-2888-3.

[21] C.W. Chan, S.H.J. Chan, H.C. Man, P. Ji, 1-D constitutive model for evolution of stress-induced R-phase and localized L??ders-like stress-induced martensitic transformation of super-elastic NiTi wires, Int. J. Plast. 32–33 (2012) 85–105. doi:10.1016/j.ijplas.2011.12.003.

[22] J.J. Marattukalam, V.K. Balla, M. Das, S. Bontha, S.K. Kalpathy, Effect of heat treatment on microstructure, corrosion, and shape memory characteristics of laser deposited NiTi alloy, J. Alloys Compd. 744 (2018) 337–346. doi:10.1016/j.jallcom.2018.01.174.

[23] Y.X. Tong, F. Chen, B. Guo, B. Tian, L. Li, Y.F. Zheng, D. V. Gunderov, R.Z. Valiev, Superelasticity and its stability of an ultrafine-grained Ti49.2Ni50.8 shape memory alloy processed by equal channel angular pressing, Mater. Sci. Eng. A. 587 (2013) 61–64. doi:10.1016/j.msea.2013.08.049.

[24] K. Gall, H. Sehitoglu, Y.I. Chumlyakov, I. V. Kireeva, Tension-compression asymmetry of the stress-strain response in aged single crystal and polycrystalline NiTi, Acta Mater. 47 (1999) 1203–1217. doi:10.1016/S1359-6454(98)00432-7.

[25] A. Saigal, M. Fonte, Solid, shape recovered “bulk” Nitinol: Part I-Tension-compression asymmetry, Mater. Sci. Eng. A. 528 (2011) 5536–5550. doi:10.1016/j.msea.2011.03.060.

[26] S.C. Mao, J.F. Luo, Z. Zhang, M.H. Wu, Y. Liu, X.D. Han, EBSD studies of the

stress-induced B2-B19′ martensitic transformation in NiTi tubes under uniaxial tension and compression, Acta Mater. 58 (2010) 3357–3366. doi:10.1016/j.actamat.2010.02.009.

[27] A.N. Bucsek, H.M. Paranjape, A.P. Stebner, Myths and Truths of Nitinol Mechanics: Elasticity and Tension–Compression Asymmetry, Shape Mem. Superelasticity. 2 (2016) 264–271. doi:10.1007/s40830-016-0074-z.

[28] A. Safdel, A. Zarei-Hanzaki, H.R. Abedi, S. Pourbabak, D. Schryvers, R. Basu, Asymmetrical superelastic behavior of thermomechanically processed semi-equiatomic NiTi alloy in tensile and compressive modes of deformation, J. Alloys Compd. 878 (2021) 160443. doi:10.1016/j.jallcom.2021.160443.

[29] K. Gall, H. Sehitoglu, Role of texture in tension-compression asymmetry in polycrystalline NiTi, Int. J. Plast. 15 (1999) 69–92. doi:10.1016/S0749-6419(98)00060-6.

[30] S.C. Mao, X.D. Han, Y.B. Tian, J.F. Luo, Z. Zhang, Y. Ji, M.H. Wu, In situ EBSD investigations of the asymmetric stress-induced martensitic transformation in TiNi shape memory alloys under bending, Mater. Sci. Eng. A. 498 (2008) 278–282. doi:10.1016/j.msea.2008.07.072.

[31] M. Elahinia, N. Shayesteh Moghaddam, M. Taheri Andani, A. Amerinatanzi, B.A. Bimber, R.F. Hamilton, Fabrication of NiTi through additive manufacturing: A review, Prog. Mater. Sci. 83 (2016) 630–663. doi:10.1016/j.pmatsci.2016.08.001.

[32] J.P. Oliveira, N. Schell, N. Zhou, L. Wood, O. Benafan, Laser welding of precipitation strengthened Ni-rich NiTiHf high temperature shape memory alloys: Microstructure and mechanical properties, Mater. Des. 162 (2019) 229–234. doi:10.1016/j.matdes.2018.11.053.

[33] S.L. Sing, J. An, W.Y. Yeong, F.E. Wiria, Laser and electron-beam powder-bed additive manufacturing of metallic implants: A review on processes, materials and designs, J. Orthop. Res. 34 (2016) 369–385. doi:10.1002/jor.23075.

[34] T. DebRoy, H.L. Wei, J.S. Zuback, T. Mukherjee, J.W. Elmer, J.O. Milewski, A.M. Beese, A. Wilson-Heid, A. De, W. Zhang, Additive manufacturing of metallic

components – Process, structure and properties, Prog. Mater. Sci. 92 (2018) 112–224. doi:10.1016/j.pmatsci.2017.10.001.

[35] J.L. Bartlett, A. Jarama, J. Jones, X. Li, Prediction of microstructural defects in additive manufacturing from powder bed quality using digital image correlation, Mater. Sci. Eng. A. 794 (2020) 140002. doi:10.1016/j.msea.2020.140002.

[36] J.L. Bartlett, F.M. Heim, Y. V Murty, X. Li, In situ defect detection in selective laser melting via full-field infrared thermography, Addit. Manuf. 24 (2018) 595–605. doi:10.1016/j.addma.2018.10.045.

[37] O. Holzmond, X. Li, In situ real time defect detection of 3D printed parts, Addit. Manuf. 17 (2017) 135–142. doi:10.1016/j.addma.2017.08.003.

[38] J.L. Bartlett, X. Li, An overview of residual stresses in metal powder bed fusion, Addit. Manuf. 27 (2019) 131–149. doi:10.1016/j.addma.2019.02.020.

[39] J.L. Bartlett, B.P. Croom, J. Burdick, D. Henkel, X. Li, Revealing mechanisms of residual stress development in additive manufacturing via digital image correlation, Addit. Manuf. 22 (2018) 1–12. doi:10.1016/j.addma.2018.04.025.

[40] A. Safdel, M.A. Elbestawi, New Insights on The Laser Powder Bed Fusion Processing of a NiTi Alloy and The Role of Dynamic Restoration Mechanisms, J. Alloys Compd. 885 (2021) 160971. doi:10.1016/j.jallcom.2021.160971.

[41] T. Gustmann, F. Gutmann, F. Wenz, P. Koch, R. Stelzer, W.G. Drossel, H. Korn, Properties of a superelastic NiTi shape memory alloy using laser powder bed fusion and adaptive scanning strategies, Prog. Addit. Manuf. 5 (2020) 11–18. doi:10.1007/s40964-020-00118-6.

[42] N. Shayesteh Moghaddam, S. Saedi, A. Amerinatanzi, A. Hinojos, A. Ramazani, J. Kundin, M.J. Mills, H. Karaca, M. Elahinia, Achieving superelasticity in additively manufactured NiTi in compression without post-process heat treatment, Sci. Rep. 9 (2019) 1–11. doi:10.1038/s41598-018-36641-4.

[43] S. Saedi, A.S. Turabi, M.T. Andani, C. Haberland, H. Karaca, M. Elahinia, The influence of heat treatment on the thermomechanical response of Ni-rich NiTi

alloys manufactured by selective laser melting, J. Alloys Compd. 677 (2016) 204–210. doi:10.1016/j.jallcom.2016.03.161.

[44] L. Xue, K.C. Atli, C. Zhang, N. Hite, A. Srivastava, A.C. Leff, A.A. Wilson, D.J. Sharar, A. Elwany, R. Arroyave, I. Karaman, Laser Powder Bed Fusion of Defect-Free NiTi Shape Memory Alloy Parts with Superior Tensile Superelasticity, Acta Mater. 229 (2022) 117781. doi:10.1016/j.actamat.2022.117781.

[45] H. Inoue, M. Ishio, T. Takasugi, Texture of TiNi shape memory alloy sheets produced by roll-bonding and solid phase reaction from elementary metals, Acta Mater. 51 (2003) 6373–6383. doi:10.1016/j.actamat.2003.08.009.

[46] S. Miyazaki, V.H. No, K. Kitamura, a. Khantachawana, H. Hosoda, Texture of Ti-Ni rolled thin plates and sputter-deposited thin films, Int. J. Plast. 16 (2000) 1135–1154. doi:10.1016/S0749-6419(00)00004-8.

[47] A.T. Sutton, C.S. Kriewall, M.C. Leu, J.W. Newkirk, Powders for additive manufacturing processes: characterization techniques and effects on part properties, in: Addit. Manuf., 2009: pp. 1–90. doi:10.1080/17452759.2016.1250605.

[48] J.P. Oliveira, F.M. Braz Fernandes, N. Schell, Miranda, Martensite Stabilization During Superelastic Cycling of Laser Welded NiTi Plates, Mater. Lett. 171 (2016) 273–276. doi:10.1016/j.matlet.2016.02.107.

[49] M. Narvan, K.S. Al-Rubaie, M. Elbestawi, Process-Structure-Property Relationships of AISI H13 Tool Steel Processed with Selective Laser Melting, Materials (Basel). 12 (2019) 2284. doi:10.3390/ma12142284.

[50] I. Serrano-Munoz, A. Ulbricht, T. Fritsch, T. Mishurova, A. Kromm, M. Hofmann, R.C. Wimpory, A. Evans, G. Bruno, Scanning Manufacturing Parameters Determining the Residual Stress State in LPBF IN718 Small Parts, Adv. Eng. Mater. 23 (2021). doi:10.1002/adem.202100158.

[51] J. Liu, G. Li, Q. Sun, H. Li, J. Sun, X. Wang, Understanding the effect of scanning strategies on the microstructure and crystallographic texture of Ti-6Al-4V alloy manufactured by laser powder bed fusion, J. Mater. Process. Technol. 299 (2022). doi:10.1016/j.jmatprotec.2021.117366.

[52] N. Nadammal, T. Mishurova, T. Fritsch, I. Serrano-Munoz, A. Kromm, C. Haberland, P.D. Portella, G. Bruno, Critical role of scan strategies on the development of microstructure, texture, and residual stresses during laser powder bed fusion additive manufacturing, Addit. Manuf. 38 (2021) 101792. doi:10.1016/j.addma.2020.101792.

[53] Y.M. Arısoy, L.E. Criales, T. Özel, B. Lane, S. Moylan, A. Donmez, Influence of scan strategy and process parameters on microstructure and its optimization in additively manufactured nickel alloy 625 via laser powder bed fusion, Int. J. Adv. Manuf. Technol. 90 (2017) 1393–1417. doi:10.1007/s00170-016-9429-z.

[54] ASTM-E8, Standard test method for tension testing of metallic materials, West Conshohocken ASTM Int. (2004).

[55] ASTM-E9, Standard test methods of compression testing of metallic materials at room temperature, West Conshohocken, PA ASTM Int. (2000) 98–105.

[56] J. Khalil-Allafi, A. Dlouhy, G. Eggeler, Ni4Ti3-precipitation during aging of NiTi shape memory alloys and its influence on martensitic phase transformations, Acta Mater. 50 (2002) 4255–4274. doi:10.1016/S1359-6454(02)00257-4.

[57] K. Kazemi-Choobi, J. Khalil-Allafi, V. Abbasi-Chianeh, Influence of recrystallization and subsequent aging treatment on superelastic behavior and martensitic transformation of Ni50.9Ti wires, J. Alloys Compd. 582 (2014) 348–354. doi:10.1016/j.jallcom.2013.08.063.

[58] X.M. Wang, B.X. Xu, Z.F. Yue, Micromechanical modelling of the effect of plastic deformation on the mechanical behaviour in pseudoelastic shape memory alloys, Int. J. Plast. 24 (2008) 1307–1332. doi:10.1016/j.ijplas.2007.09.006.

[59] Z. Xie, Y. Liu, J. Van Humbeeck, Microstructure of NiTi shape memory alloy due to tension–compression cyclic deformation, Acta Mater. 46 (1998) 1989–2000. doi:10.1016/S1359-6454(97)00379-0.

[60] M.E. Mitwally, M. Farag, Effect of cold work and annealing on the structure and characteristics of NiTi alloy, Mater. Sci. Eng. A. 519 (2009) 155–166. doi:10.1016/j.msea.2009.04.057.

[61] F. Khaleghi, J. Khalil-Allafi, V. Abbasi-Chianeh, S. Noori, Effect of short-time annealing treatment on the superelastic behavior of cold drawn Ni-rich NiTi shape memory wires, J. Alloys Compd. 554 (2013) 32–38. doi:10.1016/j.jallcom.2012.11.183.

[62] J. Michutta, C. Somsen, a. Yawny, a. Dlouhy, G. Eggeler, Elementary martensitic transformation processes in Ni-rich NiTi single crystals with Ni4Ti3 precipitates, Acta Mater. 54 (2006) 3525–3542. doi:10.1016/j.actamat.2006.03.036.

[63] S. Saedi, A.S. Turabi, M.T. Andani, N.S. Moghaddam, M. Elahinia, H.E. Karaca, Texture, aging, and superelasticity of selective laser melting fabricated Ni-rich NiTi alloys, Mater. Sci. Eng. A. 686 (2017) 1–10. doi:10.1016/j.msea.2017.01.008.

[64] K. Kazemi-Choobi, J. Khalil-Allafi, V. Abbasi-Chianeh, Investigation of the recovery and recrystallization processes of Ni 50.9Ti49.1 shape memory wires using in situ electrical resistance measurement, Mater. Sci. Eng. A. 551 (2012) 122–127. doi:10.1016/j.msea.2012.04.106.

[65] X. Wang, B. Verlinden, J. Van Humbeeck, Effect of post-deformation annealing on the R-phase transformation temperatures in NiTi shape memory alloys, Intermetallics. 62 (2015) 43–49. doi:10.1016/j.intermet.2015.03.006.

[66] X.B. Wang, B. Verlinden, J. Van Humbeeck, R-phase transformation in NiTi alloys, Mater. Sci. Technol. 000 (2014) 1743284714Y.0000000590. doi:10.1179/1743284714Y.0000000590.

[67] S. Miyazaki, S. Kimura, K. Otsuka, Y. Suzuki, The habit plane and transformation strains associated with the martensitic transformation in Ti-Ni single crystals, Scr. Metall. 18 (1984) 883–888. doi:10.1016/0036-9748(84)90254-0.

[68] E. Polatidis, M. Šmíd, I. Kuběna, W.N. Hsu, G. Laplanche, H. Van Swygenhoven, Deformation mechanisms in a superelastic NiTi alloy: An in-situ high resolution digital image correlation study, Mater. Des. 191 (2020) 1–10. doi:10.1016/j.matdes.2020.108622.

[69] H. Yan, B. Yang, Y. Zhang, Z. Li, C. Esling, X. Zhao, L. Zuo, Variant organization and mechanical detwinning of modulated martensite in Ni–Mn–In metamagnetic

shape-memory alloys, Acta Mater. 111 (2016) 75–84. doi:10.1016/j.actamat.2016.03.049.

[70] O. Matsumoto, S. Miyazaki, K. Otsuka, H. Tamura, Crystallography of martensitic transformation in Ti-Ni single crystals, Acta Metall. 35 (1987) 2137–2144. doi:10.1016/0001-6160(87)90042-3.

Chapter 4

Distortion and printability of stent structures in laser powder bed fusion processing of NiTi alloys

Complete Citation:

A. Safdel, M.A. Elbestawi, Distortion and Printability of Stent Structures in Laser Powder Bed Fusion Processing of NiTi Alloys, Mater. Lett. (2021) 130163. doi:10.1016/j.matlet.2021.130163.

Abstract

Self-expandable NiTi stents are extensively used to treat coronary or peripheral arterial disease due to their remarkable biocompatibility and superelasticity. However, the feasibility of fabricating patient-specific NiTi stents through laser powder bed fusion (LPBF) is yet to be determined. Two supposedly optimized energy density values (low and high) were used to investigate the residual stresses evolution and in-process distortion of the stents. Numerical predictions and experimental results revealed that employing an energy density of 56J/mm^3 results in an acceptable level of in-process distortion and ensures the manufacturability of dense austenitic stent structures via LPBF. However, fabricated stents suffer from low dimensional accuracy and a rough surface, which necessitates future studies to overcome these obstacles.

Keywords:

NiTi; Laser powder bed fusion; Simulation; Residual stresses; Stent.

4.1 Introduction

Stents are tubular mesh-like structures that are inserted into the vessels or tubular organs in the body to maintain a safe flow and keep the passageway open. While many alloys are utilized to produce balloon-expandable stents, NiTi alloys are primarily used to fabricate self-expandable stents due to their unique superelastic behavior and biocompatibility [1]. One of the many challenges associated with off-the-shelf stents is migration. This issue, which is related to the design of the stents, can be mitigated by fabricating patient-specific stents and exploiting the freedom of design offered by additive manufacturing (AM) [1].

Laser Powder Bed Fusion (LPBF) is one the most efficient approaches to additively manufacture metallic components with complex geometries [2]. However, process-related defects such as porosities and residual stresses led to numerous challenges, underscoring the significance of novel studies to control and monitor the process via innovative approaches [3,4]. Residual stresses, in particular, are of utmost importance due to their role in determining the part's printability. In LPBF, the extreme temperature gradients lead to high residual stress levels, causing delamination during the process and a distorted final product [5]. If the former exceeds a critical threshold, the process gets disrupted due to the impact between the distorted part and the recoater blade. In recent years, many researchers endeavored to evaluate the developed residual stresses during LPBF through destructive or more advanced non-destructive methods (e.g., digital image correlation) [6]. Alternatively, numerical approaches were also implemented to prevent conducting numerous costly and time-consuming experiments [5].

In this study, the development of residual stresses is initially assessed by utilizing two supposedly optimum energy densities and implementing the classical cantilever approach

[2]. Then the optimized parameters are employed to investigate the level of distortion during LPBF of a NiTi stent structure and determine its printability, which is a topic yet to be explored.

4.2 Modeling methodology and experimental procedure

As shown in Figure 4-1(a, b), the cantilever design was adopted, and the simulation was conducted in a sequential manner using the commercial ABAQUS2019 software. A comprehensive explanation of the modeling methodology is provided by other studies [7,8]. The model consists of two steps, in which transient heat transfer equations are initially solved to predict the temperature fluctuations of each element, and then the developed residual stresses are calculated. The heat source movement was inputted into the process by a g-code generated by the open-source ReplicatorG software. The g-code indicates the time and the coordinate that the laser beam scans a layer, and the scanning speed ($v_1 = 750, v_2 = 500mm/s$), layer thickness ($t = 30\mu m$), hatch distance ($h = 80\mu m$), and scanning strategy (alternating x/y) are all incorporated into this parameter. The laser power ($P_1 = 100, P_2 = 150mm/s$) and diameter ($d = 100\mu m$) were assumed to be constant throughout the process, having a uniform distribution on the powder bed. The mentioned parameters result in volumetric energy densities of $E_{v_1} = 56$ and $E_{v_2} = 125$J/mm^3. The part was meshed using linear hexadedron (DC3D8) elements, which were added layer by layer, having a dwell time of 10 seconds (resembling the recoater movement). Each element was activated at the melting temperature without having any strain, and the thermal stresses were subsequently calculated during rapid heating and cooling stages. Heat convection and radiation of the part and the surrounding media were considered to mimic the actual process. As is illustrated in Figure 4-1(c), a final cutting step was added to simulate the separation during cutting with an electro-discharge machine,

which facilitates the stress relaxation and results in a deflected cantilever. The values of the room temperature thermophysical properties of the NiTi alloy are presented in Table 4-1.

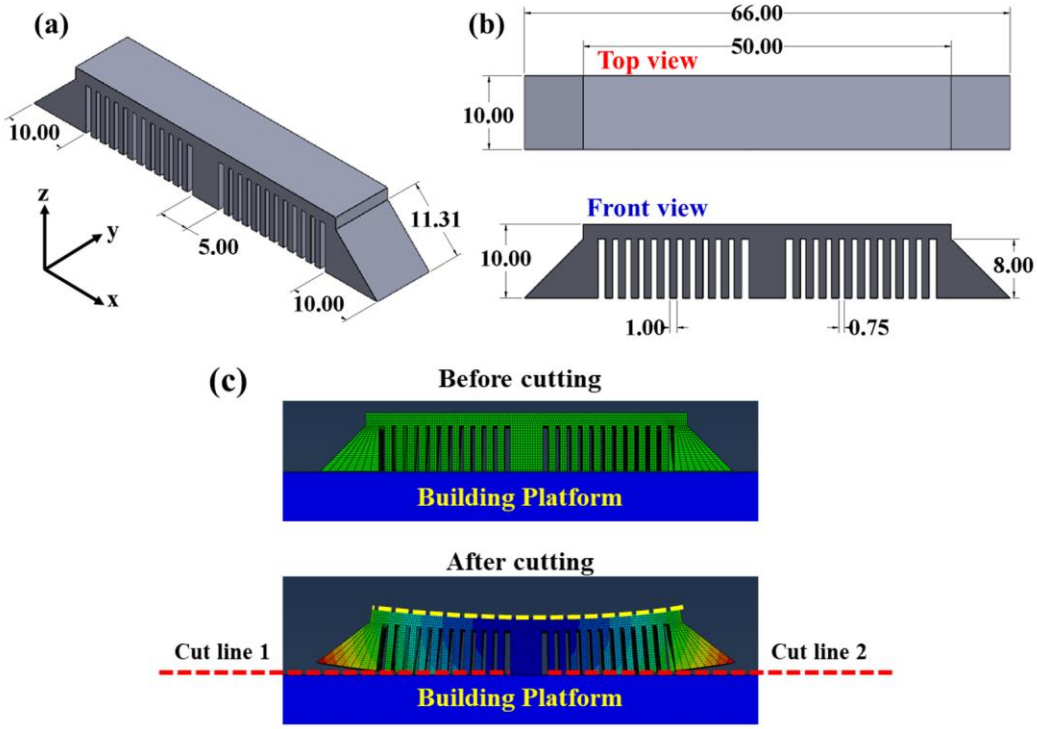

Figure 4-1 (a) the 3D design and (b) the top and front view of the cantilever, showing the dimensions (in mm), and (c) the schematic view of the fabricated cantilever, before and after cutting the sides.

Upon optimizing the model and selecting the best energy density, the simulation was carried out to predict the behavior of a stent structure during LPBF. An EOS-M280 LPBF machine equipped with a 400W fiber laser was used to manufacture the parts, and the initial feedstock was a pre-alloyed plasma atomized Ni55.7%wt-Ti powder (sieved to a particle size of 15-45μm). X-ray diffraction (XRD) patterns were acquired using a CuK_{α} (λ=1.5406$\dot{A}$) radiation and nickel content was measured by a Varian Inc. inductively

coupled plasma atomic emission spectrometer (ICP-OES). A JEOL7000 scanning electron microscope (SEM) was utilized for surface characterizations.

Table 4-1 Room temperature thermophysical properties of the NiTi alloy used for the simulations

Property	Unit	Value
Laser absorption efficiency	-	0.35
Austenite thermal expansion coefficient	$1/K$	11×10^{-6}
Martensite thermal expansion coefficient	$1/K$	6.6×10^{-6}
Austenite Young's Modulus	GPa	83
Martensite Young's Modulus	GPa	28
Poisson's ratio	-	0.33
Austenite thermal conductivity	$W/m.K$	18
Martensite thermal conductivity	$W/m.K$	8.6
Specific heat capacity	$J/g.K$	0.46
Emissivity	-	0.5

4.3 Results and Discussion

The nickel content of the fabricated samples is demonstrated in Figure 4-2(a), revealing a significant drop from 55.64 to 54.89wt% when the value of E_v is increased from 56 to 125J/mm^3. The equilibrium vapor pressure of nickel is much higher than that of titanium, indicating that nickel is more prone to evaporation at higher energy densities [9]. Optical microscopy images (Figure 4-2a) also revealed numerous spherical porosities caused by the formation of unstable keyholes at higher heat inputs [10].

Different studies [11,12] stated that the onset of the martensitic transformation (M_s) is significantly affected by the nickel content of the matrix, and the higher the nickel content,

the lower the M_s temperature. Accordingly, as is shown in Figure 4-2(b), the M_s temperature for each sample was predicted. The increase in M_s to temperatures higher than the room temperature for the sample fabricated by the energy density of 125J/mm^3 is clearly shown, denoting that the martensite phase is most likely to form. Comparing the acquired XRD patterns from both samples (Figure 4-2c) confirmed the previous statement, highlighting the characteristic peaks of the B19′ monoclinic martensite phase for the sample fabricated by the higher energy density. Therefore, the phase transformation in higher energy density was considered in the model by changing the thermophysical properties of the phases from austenite to martensite. During this transition, thermal conductivity significantly decreases, which impedes an effective heat dissipation and results in extreme thermal gradients [13].

Figure 4-2 (d) illustrates the measured deflection of the cantilever beam after cutting the sides and the occurrence of stress relaxation. While the energy density of 56J/mm^3 resulted in a very low deflection, extreme distortion was obtained for the cantilever fabricated by the higher energy density (125J/mm^3). The higher deflection in the latter is attributed to the higher heat input of the process and the increased thermal gradient, on the one hand, and the drop in the material's thermal conductivity during transformation, on the other hand. In other words, the combination of both effects leads to the development of higher residual stresses at increased energy levels.

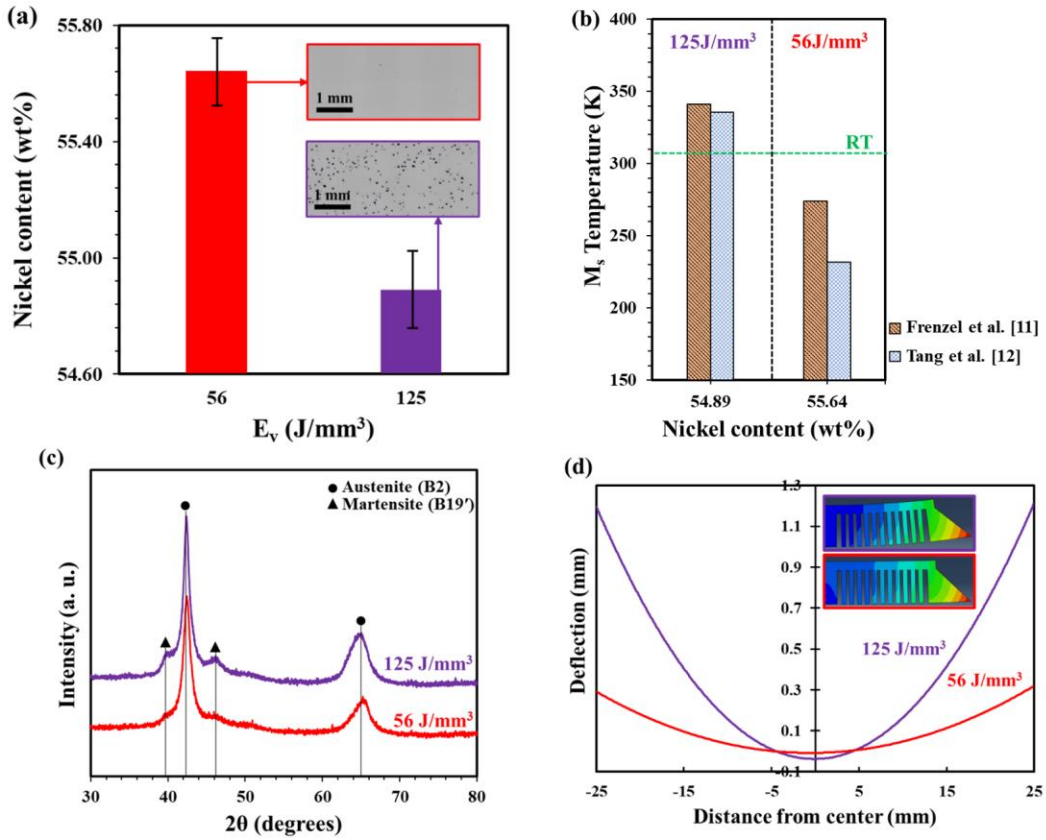

Figure 4-2 The (a) nickel content (wt%) of the matrix and optical micrographs, (b) predicted M_s temperatures, (c) XRD patterns, and (d) simulated deflection of the samples fabricated by energy densities of 56 and 125J/mm^3.

Two initial conditions should be critically considered for a NiTi alloy to be considered for stent applications: having (1) low martensitic transformation temperatures (lower than the human body temperature) and (2) minimum defects and residual stresses. It was shown that the energy density value of 56J/mm^3 results in a highly dense austenitic part with lower deflection values. Hence, it was selected for assessing the capabilities of the LPBF process in manufacturing stent structures. Figure 4-3(a) depicts a simple stent design that was employed to perform the simulations. Four nodes were selected at different building heights to examine their temperature profile and displacement during the process. The fluctuations in temperature for each of the selected nodes are presented in Figure 4-3 (b).

As is evident, the temperature of each node exceeded the melting temperature of the material (1584K) at multiple times during the process, revealing that even using a lower E_v can lead to the occurrence of an epitaxial solidification. The peak temperature of the melt pool was also lower than 2000K, which, according to Khan et al. [9], denotes negligible nickel evaporation. The numerous rapid heating and cooling cycles displayed in the figure result in significant thermal strain, distorting the stent. As was mentioned earlier, if the displacement of the material in z-direction surpasses the layer thickness at any point, the recoater blade will hit the part, resulting in a failed experiment. The displacement of each node in the Z-direction (U_Z), calculated via Eq. (1), is plotted in Figure 4-3(c) as a function of time.

$$U_Z = Z_P - Z_0 \tag{4.1}$$

where Z_P is the predicted height of a selected node at any given time during the process, and Z_n is its initial design height. As is shown, several expansion ($^{dU_Z}/_{dt} > 0$) and contraction ($^{dU_Z}/_{dt} < 0$) cycles occur during the process, correlating to the applied thermal cycle. Most importantly, the values of U_Z were lower than the selected layer thickness at all times, confirming the process feasibility and continuity.

Experimental fabrication also confirmed the predictions, in which stent structures were successfully printed using an energy density of 56J/mm^3, although other critical challenges were identified. Figure 4-3(d) demonstrates an SEM image acquired from the surface of the manufactured stent, in which the strut's thickness was measured to be 160µm as opposed to the expected 100µm. Moreover, many partially melted particles were adhered to the surface, causing a very rough surface. Consequently, the LPBF process is

capable of manufacturing NiTi stents, but further studies are still required to optimize the process and identify the necessary post-processing steps in enhancing their functionality.

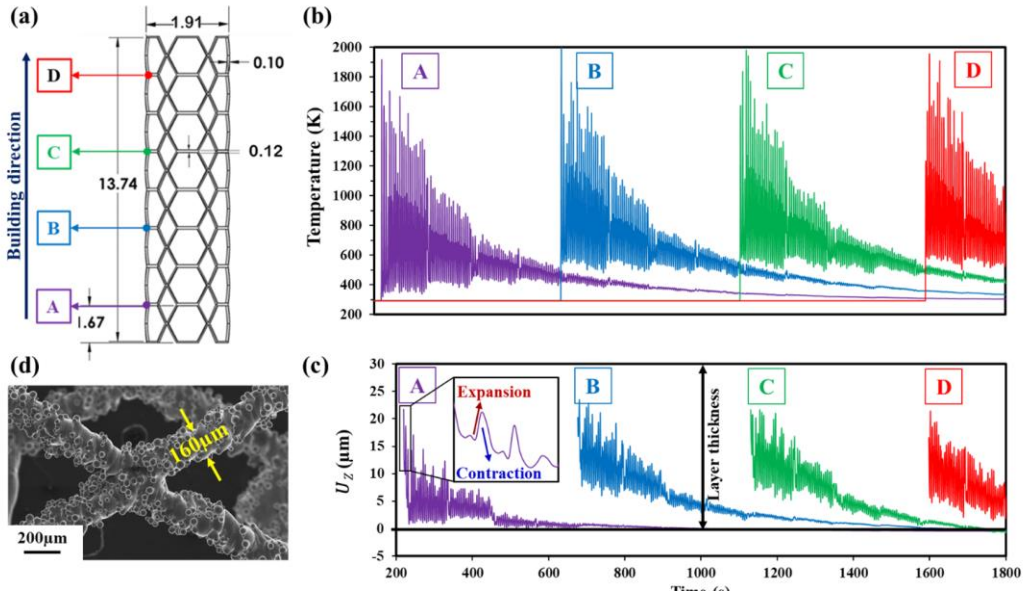

Figure 4-3 (a) dimensions of the stent structure (in mm) and the location of each node, (b) temperature profile and (c) in-process displacement of the selected nodes, and (d) the SEM image of the stent's surface.

4.4 Conclusion

Two volumetric energy densities values (56 and 125J/mm^3) were initially utilized in this study to predict the deflection that occurs after fabricating a NiTi cantilever beam. The energy density of 125J/mm^3 resulted in severe distortion due to the combining effects of the extreme thermal gradient and the martensitic transformation, which effectively increased the residual stresses. On the contrary, the energy density of 56J/mm^3 was found to be the optimum value to fabricate a defect-free austenitic part and avoid high residual stresses. Simulations based on this energy level were carried out for NiTi stent structures in which the distortion of the stent at different heights was monitored. Measurements revealed an acceptable level of in-process displacement, ensuring process continuity and

feasibility. Therefore, the LPBF process can be considered as a promising technique to fabricate patient-specific stent structures, given that the optimized processing parameters are employed. Although NiTi stents were printed for the first time, future studies are still required to enhance the additively manufactured stents' dimensional accuracy and surface characteristics before considering clinical implementations.

4.5 References

[1] K. Maleckis, E. Anttila, P. Aylward, W. Poulson, A. Desyatova, J. MacTaggart, A. Kamenskiy, Nitinol Stents in the Femoropopliteal Artery: A Mechanical Perspective on Material, Design, and Performance, Ann. Biomed. Eng. 46 (2018) 684–704. doi:10.1007/s10439-018-1990-1.

[2] M. Elahinia, N. Shayesteh Moghaddam, M. Taheri Andani, A. Amerinatanzi, B.A. Bimber, R.F. Hamilton, Fabrication of NiTi through additive manufacturing: A review, Prog. Mater. Sci. 83 (2016) 630–663. doi:10.1016/j.pmatsci.2016.08.001.

[3] O. Holzmond, X. Li, In situ real time defect detection of 3D printed parts, Addit. Manuf. 17 (2017) 135–142. doi:10.1016/j.addma.2017.08.003.

[4] J.L. Bartlett, F.M. Heim, Y. V Murty, X. Li, In situ defect detection in selective laser melting via full-field infrared thermography, Addit. Manuf. 24 (2018) 595–605. doi:10.1016/j.addma.2018.10.045.

[5] J.L. Bartlett, X. Li, An overview of residual stresses in metal powder bed fusion, Addit. Manuf. 27 (2019) 131–149. doi:10.1016/j.addma.2019.02.020.

[6] J.L. Bartlett, B.P. Croom, J. Burdick, D. Henkel, X. Li, Revealing mechanisms of residual stress development in additive manufacturing via digital image correlation, Addit. Manuf. 22 (2018) 1–12. doi:10.1016/j.addma.2018.04.025.

[7] C. Li, J.F. Liu, X.Y. Fang, Y.B. Guo, Efficient predictive model of part distortion and residual stress in selective laser melting, Addit. Manuf. 17 (2017) 157–168. doi:10.1016/j.addma.2017.08.014.

[8] M. Narvan, A. Ghasemi, E. Fereiduni, S. Kendrish, M. Elbestawi, Part deflection and residual stresses in laser powder bed fusion of H13 tool steel, Mater. Des. 204 (2021) 109659. doi:10.1016/j.matdes.2021.109659.

[9] M.I. Khan, A. Pequegnat, Y.N. Zhou, Multiple memory shape memory alloys, Adv. Eng. Mater. 15 (2013) 386–393. doi:10.1002/adem.201200246.

[10] J.L. Bartlett, A. Jarama, J. Jones, X. Li, Prediction of microstructural defects in additive manufacturing from powder bed quality using digital image correlation,

Mater. Sci. Eng. A. 794 (2020) 140002. doi:10.1016/j.msea.2020.140002.

[11] J. Frenzel, E.P. George, a. Dlouhy, C. Somsen, M.F.X. Wagner, G. Eggeler, Influence of Ni on martensitic phase transformations in NiTi shape memory alloys, Acta Mater. 58 (2010) 3444–3458. doi:10.1016/j.actamat.2010.02.019.

[12] W. Tang, Thermodynamic study of the low-temperature phase B19′ and the martensitic transformation in near-equiatomic Ti-Ni shape memory alloys, Metall. Mater. Trans. A. 28 (1997) 537–544. doi:10.1007/s11661-997-0041-6.

[13] C. Zanotti, P. Giuliani, G. Riva, A. Tuissi, A. Chrysanthou, Thermal diffusivity of Ni-Ti SMAs, J. Alloys Compd. 473 (2009) 231–237. doi:10.1016/j.jallcom.2008.05.040.

Chapter 5

Laser powder bed fusion of differently designed NiTi stent structures having enhanced recoverability and superelasticity

Complete Citation:

A. Safdel, H. Torbati-Sarraf, M.A. Elbestawi, Laser powder bed fusion of differently designed NiTi stent structures having enhanced recoverability and superelasticity, Submitted to the Journal of Alloys and Compounds (2023).

Abstract

Tubular mesh structured NiTi stents have been integral to the biomedical industry in the treatment of arteries' narrowings or blockages. Conventionally manufactured stents are not patient-specific and the process consists of a series of expensive and time-consuming tube drawings, laser cutting, and post-processing techniques. In this study, laser powder bed fusion (LPBF) was utilized to fabricate four differently designed NiTi stent structures with very thin struts (~0.08-0.3mm) which were subsequently heat treated. Surface modification through electropolishing not only decreased the average surface roughness but also contributed to remarkable dimensional accuracy. Structural examinations revealed that stents are highly dense with only a few minor spherical gas porosities. Extremely high recoverability (~80-96%) during compression could be recorded and bending angles varied from 16.3° to 27.9° before fracture or kinking. Nanoindentation tests indicated that the fabricated parts are all having an enhanced level of superelasticity in which depth recovery values of higher than ~95% were achieved. Microstructural characterization identified near-identical microstructures, with equiaxed grains in axial surfaces and elongated grains in radial surfaces oriented toward <001> direction parallel to the building direction. Consequently, LPBF proved to be a highly capable alternative to fabricate NiTi stents enabling the production of patient-specific stents in near future.

Keywords:

NiTi; Laser powder bed fusion; Superelasticity; Stent; Nanoindentation; Recovery.

5.1 Introduction

Biomedical stents are tubular mesh-like structures that are inserted into tubular organs or vessels in the body to remedy the stenosis and narrowing that can occur due to a variety of reasons such as the build-up of fatty deposits, accumulation of plaques, inflammation, or external compression [1,2]. While different materials, namely stainless steel, cobalt chromium (CoCr), and platinum chromium (PtCr) are being utilized to fabricate balloon-expandable stents, NiTi alloys are dominating the market when it comes to the production of self-expandable stents due to their exceptional superelasticity (SE) and biocompatibility [3–5]. For a superelastic NiTi alloy, having an austenitic B2 parent phase, high levels of strain can be accommodated in deformation through the occurrence of stress-induced martensite transformation which can be mostly recovered by unloading and the involvement of the reverse transformation [6]. The diameter of most NiTi stents after insertion can range from 2 to 5mm and a catheter is generally used to insert the compressed stent into the location of interest [7]. The current approach in manufacturing NiTi stents involves a series of complicated and challenging processing steps, including tube drawing, laser micro-cutting, and machining, along with conducting post processes such as heat treatment and surface modifications [2,8]. Such an approach is not only limited in terms of repeatability and production rate but also requires various pieces of machinery, cumulatively adding to both the cost and time of the fabrication process and eventually the price of the NiTi stents. Most importantly, the currently available off-the-shelf stents are not patient-specific and are extremely limited in terms of their design, which could cause other problems such as stent migration, due to the mismatch between the shape or diameter of the stents and the patients' arteries, necessitating secondary surgeries to remove the unusable expanded stent [9,10]. The recent developments in laser powder bed fusion

(LPBF), the most prominent additive manufacturing (AM) technique to fabricate metallic parts, led to various studies focusing on assessing the capabilities of the LPBF to manufacture high quality NiTi stents with the required properties [2,11–13].

In the LPBF process, parts are manufactured in a layer-by-layer manner on a powder bed in which a high-powered laser beam selectively scans a 2D slice of a 3D computer-aided design, melting and fusing the powder particles [14]. Although LPBF excels in fabricating parts with complex geometries, other concerns, such as the formation of porosities, changes in the chemical composition, and the generation of high levels of residual stresses should be primarily addressed [15]. The current authors previously studied the printability of ultra-thin NiTi stents, having struts with diameters around 100µm, by focusing on the developed stresses and the occurred distortion throughout the LPBF process, concluding that the fabrication is indeed feasible given that lower volumetric energy densities (~56J/mm^3) are employed [9]. Moreover, Jamshidi et al. [2] focused on Ni-evaporation during LPBF of NiTi stents (strut sizes of 250 to 560µm), indicating that lower laser energy inputs are more favorable in terms of loss of alloying elements and preserving the transformation temperatures. Although the LPBF process promises a high potential for substituting the conventional stent fabrication approaches and the ability to manufacture hundreds of stents in one print taking less than a day, there is still a lack of a comprehensive understanding of the mechanical properties and the microstructural characteristics of the fabricated stents, especially when different designs with very thin struts (~100-300µm) are involved. Accordingly, further investigations is necessary to evaluate the stents' properties and address the shortcomings prior to any clinical application. To this end, this research aims to provide an in-depth investigation into the LPBF processing of NiTi stents with four

different mesh structures and strut sizes and examine the correlation between the designs, defects, surface quality, mechanical properties, superelasticity, and microstructure.

5.2 Experimental procedures

The initial powder feedstock with a chemical composition noted in Table 5-1 was supplied by the AP&C company, located in Quebec, Canada, confirming that the elemental composition is in the accepted range of the F2063 standard, which corresponds to the application of NiTi alloys for biomedical applications [16].

Table 5-1 Chemical analysis of the as-received powder (weight percent)

Element	Ti	Ni	C	Co	Cu	Cr	Fe	Nb	N + O
Measured	Balanced	55.7	0.034	0.010	0.001	0.004	0.023	<0.002	0.021
F2063	Balanced	54.5-57.0	0.050	0.050	0.010	0.010	0.050	0.025	0.050

The obtained scanning electron microscopy (SEM) micrograph is also demonstrated in Figure 5-1, showing that nearly all particles are spherical in shape without having any adherent defects and satellites. Such quality could be achieved through a meticulous plasma atomization process in which the rate of cooling is much lower compared to other atomization processes, providing enough time for the melted particles to reach a fully spherical shape during cooling and solidification in a controlled environment [17]. The quality of the feedstock is imperative in the current study due to the thin and delicate designs of the stents' struts and ensuring the repeatability of the process. The particle size for the as-received powder feedstock was in the range of 15-45μm, and D_{10}, D_{50}, and D_{90} values were measured to be approximately 14, 27, and 40μm, respectively. The results of the conducted X-ray diffraction (XRD) and differential scanning calorimetry (DSC)

analysis in the authors' previous study also represented that the powder particles are fully austenitic, and A_f, A_s, M_f, and M_s temperatures are 3, -25, -34, and -11℃, respectively [16,18]. Therefore, the martensitic transformation temperature is well below the room temperature, enabling the manufactured parts to have the potential of showing enhanced superelasticity if properly post-heat treated.

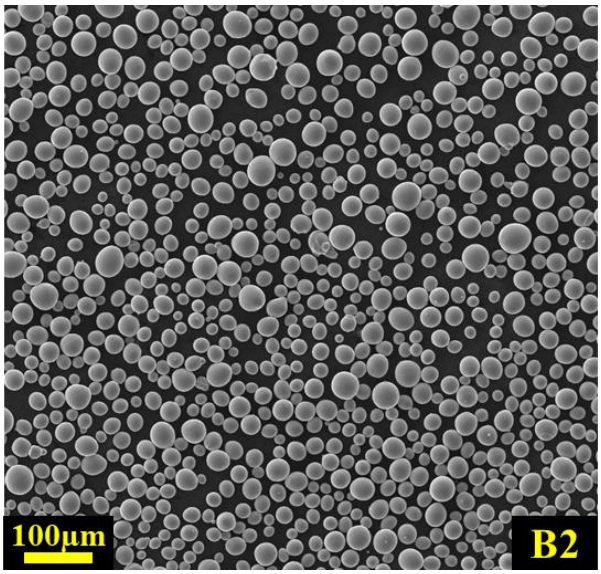

Figure 5-1 The acquired SEM image of the utilized fully austenitic (B2) powder feedstock, with D_{10}, D_{50}, and D_{90} values of 14, 27, and 40µm, respectively.

Based on the literature, different tubular meshed structures were initially considered and modified to comply with the design requirements of the LPBF process resulting in the final designs as illustrated in Figure 5-2, labeled D1, D2, D3, and D4. Figure 5-2(a-d) shows the reiterating unit for each of the structures across the building platform, contributing to the fabrication of the final parts with a height of 50mm and an outer diameter of 5mm. As is shown, the stents are having very thin struts, ranging from the highest thickness of 340µm for D1 to a very thin 80µm strut size for D4. Moreover, while D2 and D4 do not have any overhang surfaces with a 90° angle relative to the building platform, some struts in D1 and

D3 are built having surfaces horizontal to the building platform without the addition of any supports throughout the process.

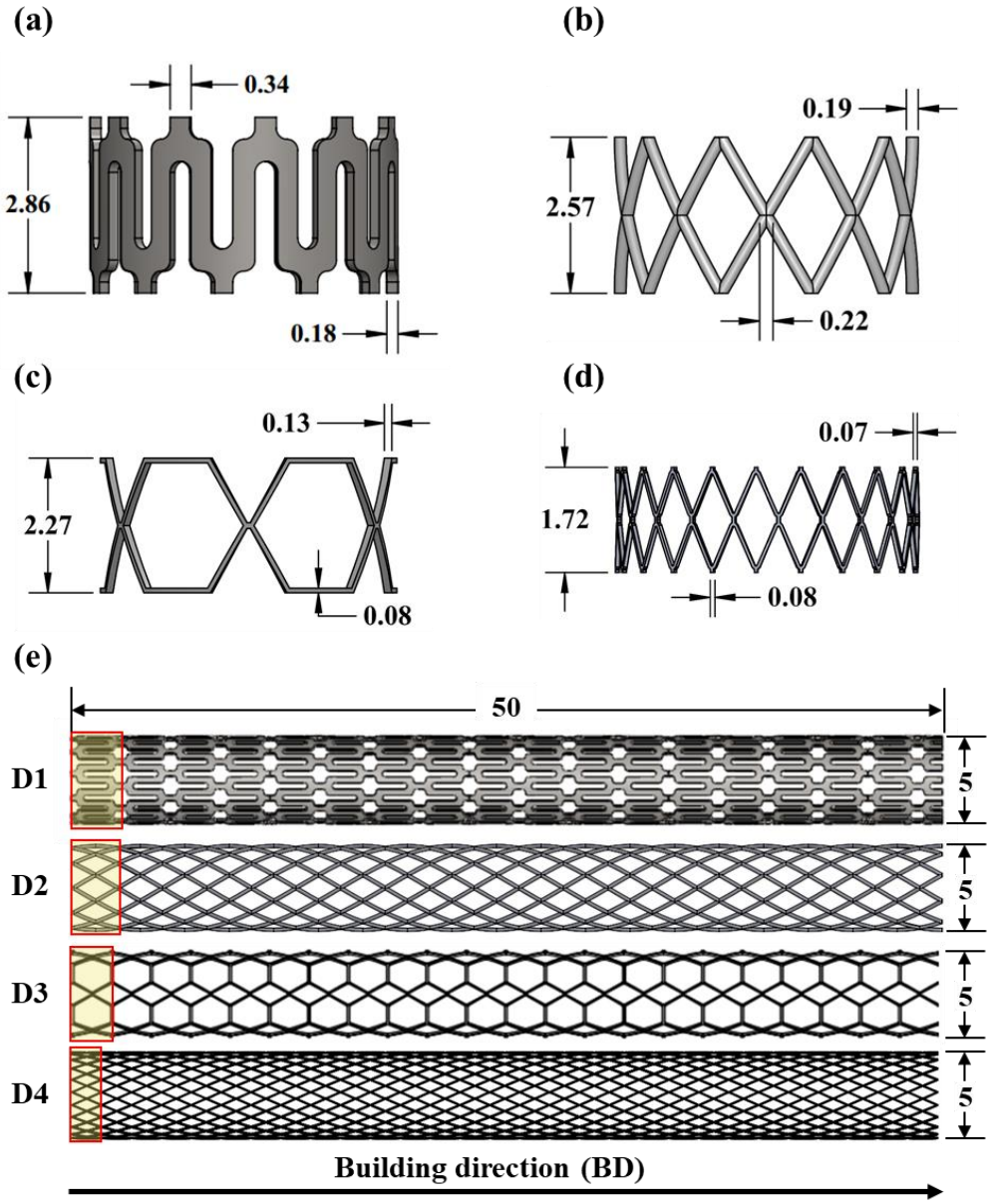

Figure 5-2 (a-d) the schematic representation of one unit cell for each stent structure and (e) the ultimate view for each design comprising of the iteration of the shown unit cell in the building direction. The diameter and the final building height for all designs were 5 and 50mm, respectively.

The selection of LPBF processing parameters is crucial in fabricating such structures and based on the authors' previous study, the optimum values to fabricate dense defect-free NiTi components, as represented in Table 5-2, were utilized [16]. It has been proven that such parameters could result in the fabrication of NiTi components without having any major defects such as gas or keyhole porosities, cracking, or loss of alloying elements, while transformation temperatures are still favorable for SE and only low levels of residual stresses can be generated. For the scanning strategy, the alternation of laser passes in x/y directions and the rotation angle of 67° was selected due to the complexity of the designs and the advantage of a high level of randomness that such a strategy could provide.

An EOS-M280 selective laser melting (SLM) machine (EOS, Germany) equipped with a fiber laser with a maximum power of 400W was used to fabricate the NiTi stent structures. The Ni-rich NiTi building platform was also preheated to the maximum allowable temperature of 200℃, helping to reduce the thermal gradients and further prevent the development of high residual stresses to ensure fabrication feasibility. Additionally, the constant flow of Argon was maintained during the process to avoid oxidation and prevent the formation of undesired secondary phases. In this experiment, 300 stents with the presented designs were all printed in less than 12 hours. Subsequent to the fabrication, an electro-discharge machine (EDM) was utilized to separate the manufactured stents from the building platform.

Different studies have pointed out that as-fabricated NiTi alloys suffer from a lower level of superelasticity and exhibit inferior deformation recoverability [19–22]. Therefore post heat treatment processes such as aging are necessary to enhance the SE behavior of the material [23]. The authors have previously examined the optimum heat treating conditions and concluded that aging the manufactured NiTi samples at 550ºC for 6 hours in a tube

furnace filled with high-purity Argon gas could stimulate the occurrence of the restoration mechanisms and promote the formation of Ni_4Ti_3 precipitates, satisfying the prerequisites of having enhanced SE [18]. Accordingly, all stents were tested after heat treatment and the obtained results are discussed in the following sections.

Table 5-2 The employed LPBF processing parameters to manufacture high-quality NiTi structures

Laser power (*P*)	100W
Scanning speed (*v*)	750mm/s
Hatch distance (*h*)	80µm
Layer thickness (*t*)	30µm
Scanning strategy	Alternating x/y with 67° rotation angle
Volumetric energy density (E_v)	55.56J/mm^3

In order to examine the structural integrity of the stents and the state of defects, especially porosities, the X-ray micro-computed tomography (µ-XCT) technique was utilized. This technique would help to reveal the shape and sizes of the internal porosities in 3D, providing a better understanding of the structural integrity of each structure [24]. The XCT scans were conducted by a Zeiss Xradia Versa 520 machine, operating at 100kV and a resolution of 1.5µm voxel size. The 3D visualization of the segmented voxels was performed by the ParaView software.

As was noted, the LPBF process is limited in creating a smooth surface after production, and either chemical or electrochemical polishing steps are required to treat the surface. To this end, electrochemical polishing was conducted to improve the surface roughness and remove the impartially melted or adherent particles in which stents acted as the anode in a solution of acetic acid (CH_3COOH), perchloric acid ($HClO_4$), ethanol (C_2H_6O), and

glycerol ($C_3H_8O_3$) with volume percentages (wt.%) of 82:5:10:3, respectively. The treatment was performed at room temperature and the voltage and current density were set to 45V and 0.55mA/cm^2, respectively.

The mechanical properties and superelasticity of the manufactured structures were assessed by compression, three-point bending, and nanoindentation tests. For the compression tests, a universal MTS instrument equipped with a cylindrical loading pin, having a diameter of 15mm, was utilized to compress the stents in a direction perpendicular to the stents' axial axis (i.e., $LD \perp BD$) to a displacement value equal to half of their nominal outer diameter (i.e., 2.5mm), followed by an unloading step to zero load. In other words, stents were deformed to 50% of their outer diameter and then unloaded to allow the occurrence of shape recovery. It should be mentioned that the loading-unloading rate was 10mm/min in each step. To ensure repeatability, each compression test was conducted on five identical samples and the average values along with the standard deviations are reported in the corresponding section.

As for bending, three-point bending tests were performed using the same instrument and the same loading-unloading rate, in which a length of 40mm was bent to the point that catastrophic strut fracture or kinking occurred, and the bending angles were extracted based on the displacement values.

Nanoindentation tests were carried out using an Anton Paar NHT^3 testing system and two indenter tips, Berkovich and spherical (radius = 20μm), were used to discuss the hardness values and the SE response of the stents. It has been previously shown that for the Berkovich indenter, depth recovery ratio is extremely limited due to the promotion of plastic deformation and generation of a higher density of dislocation [25]. On the other

hand, the spherical tip can be better suited to present the material's superelasticity by recording the depth recovery ratio since stress induced martensite transformation is the dominant deformation mechanism [26]. With the Berkovich indenter, the maximum load was set to 100mN, and the loading/unloading rate and dwell time were 50mN/min, and 10s, respectively. For SE assessment by the spherical tip, three loading/unloading cycles were performed with the same rate and dwell time, adding the maximum load in each step from 50 to 150mN in increments of 50mN. The depth recovery ratio and the dissipated energy ratio were extracted from the graphs which will be discussed in more detail in the following section. As is illustrated in Figure 5-3, the stents were cut in half via EDM in the axial and radial directions and the nanoindentation tests were performed on polished radial surfaces in which the loading direction would be perpendicular to the building direction ($LD \perp BD$). To put it simply, due to the nature of the application, stents are loaded in the radial direction, which dictates that the mechanical properties and SE assessments should all be performed in the same direction.

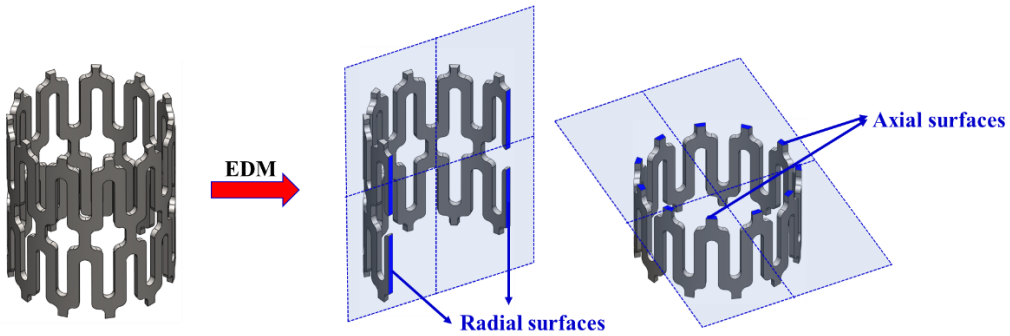

Figure 5-3 Schematic views of the examined radial and axial surfaces extracted by EDM for a sample stent.

Both axial and radial surfaces of the stents were characterized by a JEOL JSM-7000F field emission-SEM, operating at 20kV and equipped with an electron backscatter diffraction

(EBSD) detector to examine the grain morphology and texture. Samples were meticulously prepared for EBSD characterization by an initial grinding step using SiC papers with grit sizes of 800 to 4000 and a subsequent polishing process consisting of 3 to 0.1µm diamond pastes and a 0.02µm colloidal silica suspension as the last step. These steps could guarantee the acquisition of high-quality Kikuchi-pattern data for further post-processing by the utilized commercial AZtecCrystal and Channel5 software.

5.3 Results and Discussion

5.3.1 Dimensional accuracy

Figure 5-4 displays the acquired XCT images of the stent structures viewed from either the side (Figure 5-4a) or top (Figure 5-4 b). Firstly, it should be mentioned that despite very low strut sizes, the acquired processing parameters were capable of manufacturing all the structures without any major failure. Nonetheless, as is depicted in Figure 5-4 (a), it is clear that two designs, D1 and D3 suffer from a rougher surface in regions where overhangs are present, marked by arrows. In LPBF, while the laser is scanning a new layer, previous layers are also partially melted which could contribute to the occurrence of epitaxial solidification and grain growth in the building direction. However, for these overhang areas, while the laser is scanning the 2D section of the part, the heat accumulation transferred to the lower layers of the powder bed in the absence of support structures could result in considerable levels of adherent particles and increased surface roughness. On the other hand, D2 and D4 were designed to have a lower angle to avoid horizontal surfaces parallel to the BD which resulted in smoother surfaces without the issues mentioned observed for the other two designs.

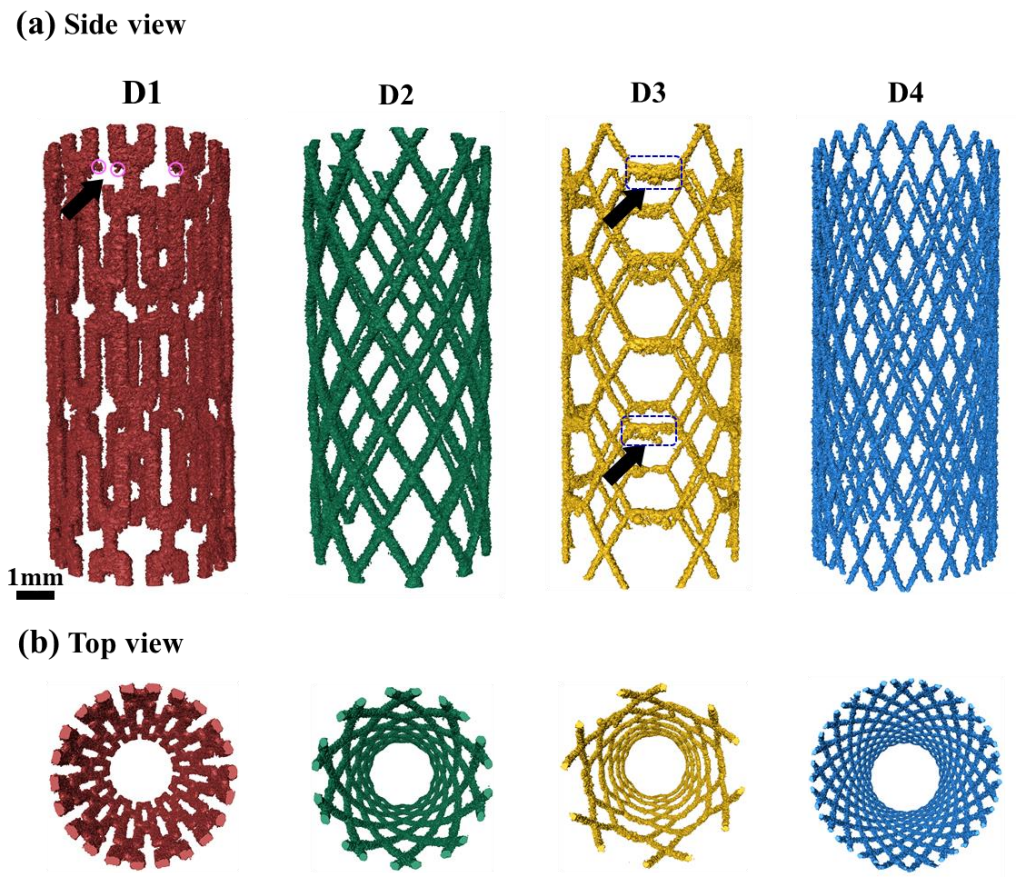

Figure 5-4 The acquired (a) side and (b) top view of the XCT images of the fabricated structures.

In general, surface roughness is an inherent property of the parts fabricated by LPBF due to the impact of the staircase effect, and as is shown all four designs are having a certain roughness, especially when downward-facing surfaces are manufactured. Furthermore, the dimensional accuracy of the fabricated parts would also be affected by both the surface roughness and the laser scanning strategy. The effective laser diameter is smaller than the gaussian laser beam profile affecting the energy distribution on the power bed causing a bigger melt pool and an enlarged heat-affected area. This is also evident in Figure 5-4(b) in which the cross sections of the stents reveal that not only there are random particles attached to the surfaces of the part, but also the strut area is higher than the designed size.

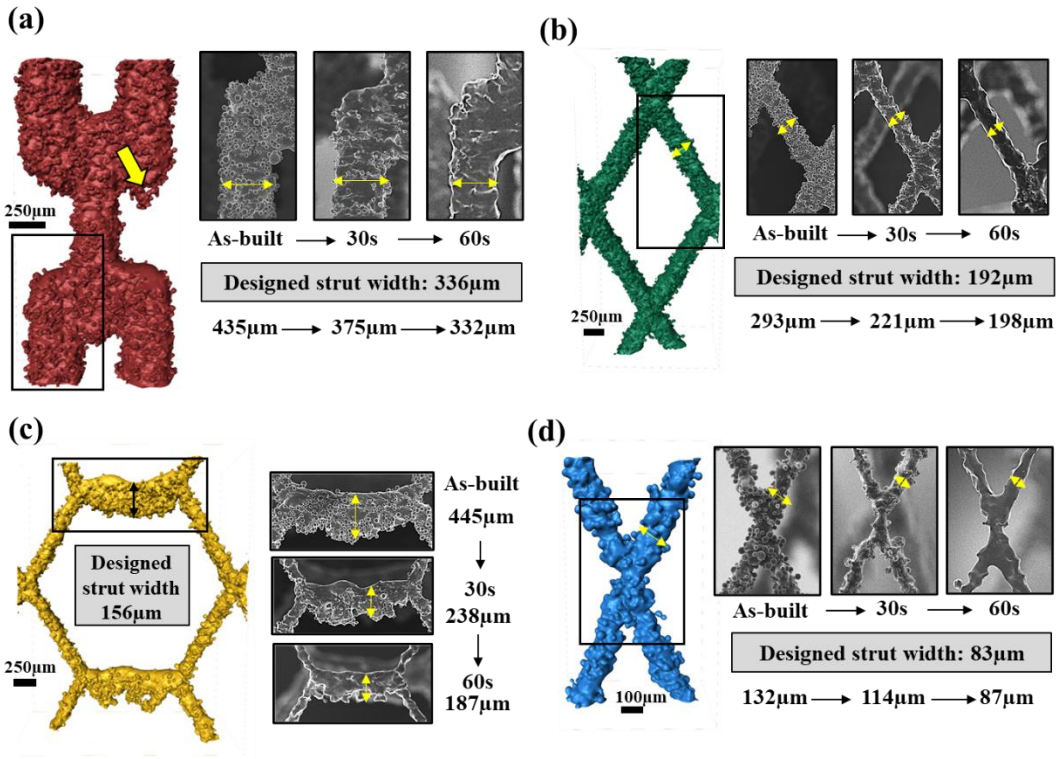

Figure 5-5 The XCT image of a selected strut from the stent structures and the acquired SEM images of the marked struts after conducting the electropolishing treatment for 30 and 60s. The designed strut size and the changes of the thickness from as-built to electropolished samples are presented for each SEM image.

In order to simultaneously enhance the dimensional accuracy of the fabricated parts and mitigate the surface roughness, electropolishing treatment was conducted and the XCT image of the as-built stent along with the SEM images that reveal the changes of the thickness of a selected strut for each design after 30 and 60s polishing treatment is demonstrated in Figure 5-5. For all samples, it is shown that not only adherent particles and impartially melted particles are considerably removed from the surface of the stents, contributing to a smoother surface, but also the dimensional accuracy is significantly enhanced as well. For surfaces facing the building platform, the problem could only be partially resolved since the struts were abnormally thicker, and prolonged electropolishing

times lead to severe thinning and an unfavorable decrease in the adjacent struts' thickness, as is plotted in Figure 5-5(c).

By considering various struts for a specific structure, the average surface roughness value (R_a) was measured, and the results are represented in Figure 5-6. Clearly, the surface roughness was improved by conducting the polishing treatments and in all cases, lower R_a values were recorded by increasing the electropolishing time. Expectedly, D1 and D3 showed the highest roughness (7.82 and 9.07µm, respectively) due to the presence of overhangs while the R_a value for D2 and D4 was approximately 6.27 and 6.54µm.

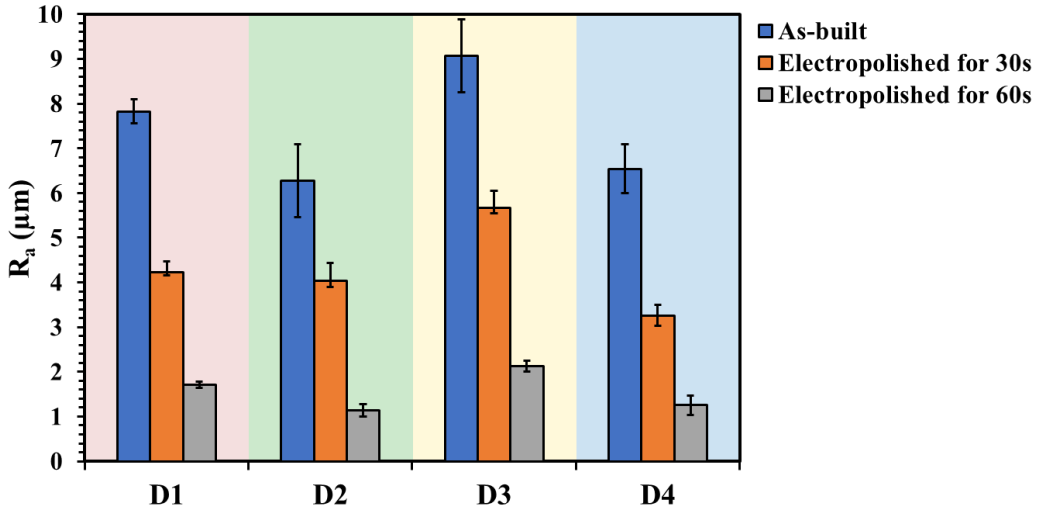

Figure 5-6 The measured changes in the average surface roughness (R_a) value for each stent design after the LPBF process and the electropolishing treatments.

Different studies on conventionally fabricated NiTi stents reported different values for the level of R_a in terms of biocompatibility ranging from 1-5µm but as a safe practice, the lower the average surface roughness, the better the material's biocompatibility [27,28]. However, in recent years many studies have revealed that biocompatibility can be significantly improved if NiTi stents were covered by a highly biocompatible coating in which the surface roughness can be an advantage, enhancing the level of stent/coating

adhesion [29–31]. In this study, the lowest roughness values of 1.70, 1.14, 2.12, and 1.25µm were obtained for D1 to D4, respectively, proving that the combination of LPBF and electrochemical polishing could be a notable alternative to conventional stent manufacturing approaches, especially if the processed stents are too be coated to achieve maximum biocompatibility.

5.3.2 Internal porosities

The presence of internal defects and porosities is another imperative aspect in determining the NiTi stents' functionality. Therefore, the results of the XCT analysis were post-processed and the diameter and sphericity of all the porosities inside the mesh structures were measured. Accordingly, the acquired results in Figure 5-7 represent that all samples had a very limited number of porosities, and the overall relative density was higher than 99.8% in all cases. The average pore diameter for each design is also denoted in the figure stating that the pore diameter was around 20.18, 22.87, 23.29, and 15.15µm for designs D1 to D4, respectively. More importantly, the sphericity index was measured for the porosities, revealing that most pores are having a near to perfect sphere shape. The lack of pores with a sphericity index much lower than 1 signifies that irregularly shaped pores are not present in the final microstructure of the samples. Irregularly shaped pores are usually formed by a lack of fusion and inadequate penetration of the melt pool from the currently built layer to the previous ones.

On the other hand, spherical pores could be caused by either keyhole or gas porosities from which the former is much bigger in size in comparison with the latter. The authors' previously proved that for lower volumetric energy density levels and the parameters that were used in this study, nickel evaporation is negligible which rules out the formation of keyhole porosities [16]. Thus, it can be concluded that the majority of these pores are gas

porosities, formed due to the presence of gases inside the powder particles entrapped during the atomization process or the entrapment of Ar or O inside the melt pool in the course of the LPBF. In conclusion, all parts were found to be relatively defect free, having a very high density which is imperative since such internal defects adversely affect the mechanical properties.

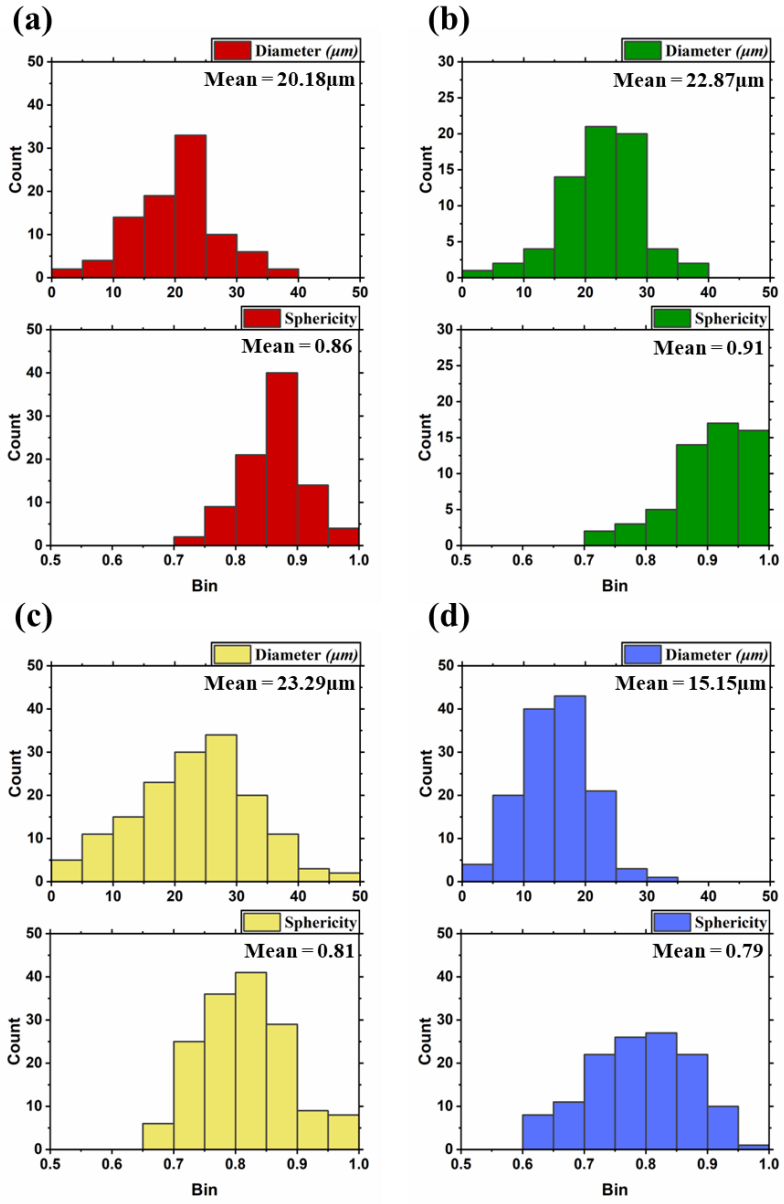

Figure 5-7 The distribution profile of the diameter of the pores and their corresponding sphericity inside samples (a) D1, (b) D2, (c) D3, and (d) D4.

5.3.3 Compressive response

The force-displacement curves were acquired through the loading-unloading compression tests and the displacement values were changed to deformation, considering that the stents were compressed in a direction perpendicular to their axial axis by a value of 2.5mm, equal to half of the nominal outer diameter, resulting in 50% deformation as is displayed in Figure 5-8. Accordingly, the load values were different for each stent corresponding to the structure and design of each specimen, and also varying degrees of recovery ratios were obtained. Moreover, while D1 and D2 are showing smoother curves, D3 and D4 are exhibiting some serrations at much lower loads due to their lower strut thicknesses. Thinner struts have a higher tendency to get dislodged and disconnected, affecting the parts' properties. The total recovery ratio was measured by dividing the value of the recovered deformation by the total deformation as presented in Figure 5-8(a) leading to Figure 5-9 in which, the maximum force at 50% deformation and total recovery values are represented.

As is demonstrated in Figure 5-9, the applied force when the stent structures are compressed to half of their diameter is the highest for D2 which possesses a higher average strut size, followed by D1, D3, and D4 with sequentially thinner struts and lower average strut sizes. Direct comparison of the force values is not easily feasible due to the lack of standardization, and the differences in the testing setup, specifically the loading pin diameter, as well as the diameter of the stents [5,32]. For instance, considering various commercial NiTi stents with a diameter of 8mm, Dyet et al. [33] established that when a 6.35mm diameter loading pin is utilized, the maximum forces at 50% deformation can be ranged from 2.7 to 3.4N. Zou et al. [34] also focused on the compressive behavior of 6-mm diameter braided NiTi stents by utilizing a 5mm diameter presser foot. The maximum forces to attain 50% deformation varied from approximately 2 to 8N, with different levels

of recovery ratios ranging from 70 to 90%. Indeed, due to the bigger diameter for the loading pin in this study, the extracted forces are expectedly higher.

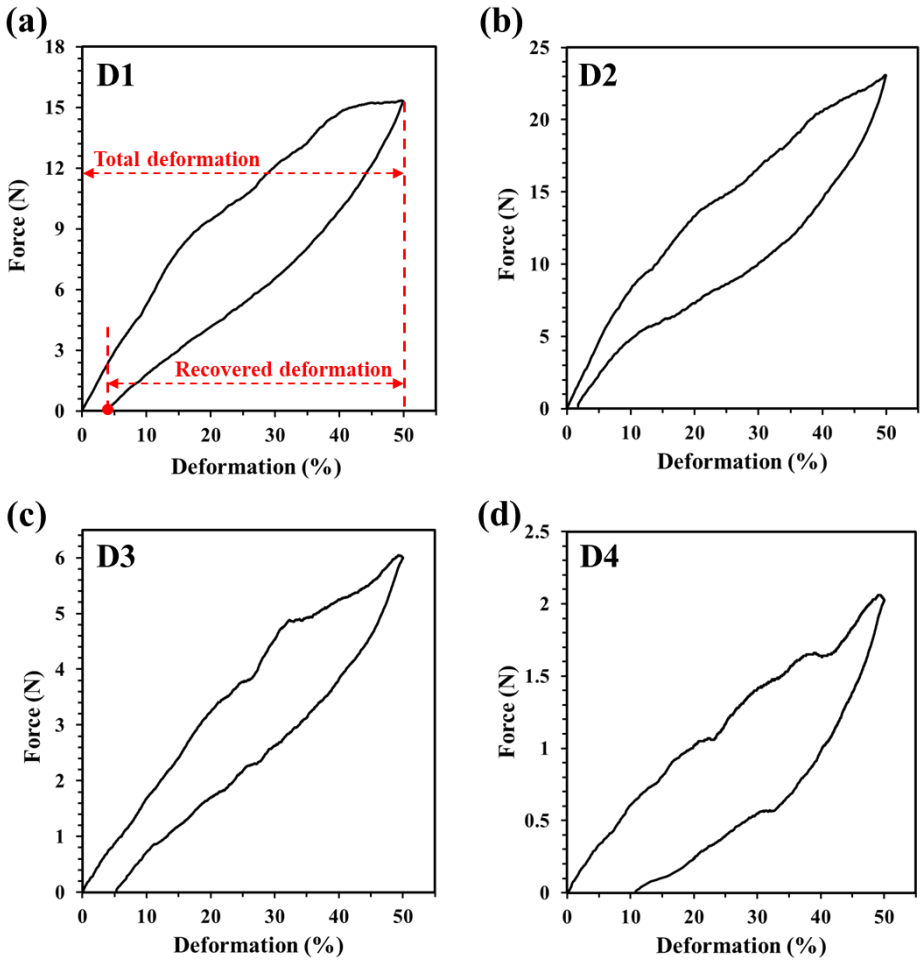

Figure 5-8 The correlation between force and the deformation ratio of the stents in a loading-unloading compression test.

Furthermore, recovery ratio should be carefully assessed as one of the most critical parameters to determine the NiTi stents expansion after contraction. In this regard, several samples were assessed, and the average recovery ratio was measured as is show in Figure 5-9 by red squares. All samples exhibited remarkable recovery during the unloading proving that the acquired ratios are well in the range of current stents [33,34], emphasizing the capabilities of LPBF to manufacture NiTi stents as a competitive alternative fabrication

process. In this regard, D2 showed the highest recovery (95.72%) and excellent testing repeatability, followed by D1 in which 89.2% recovery was recorded. Samples D3 and D4 were able to only achieve 87.8% and 79.2% recovery, which is believed to be due to the strut displacement and disconnection that were mentioned above.

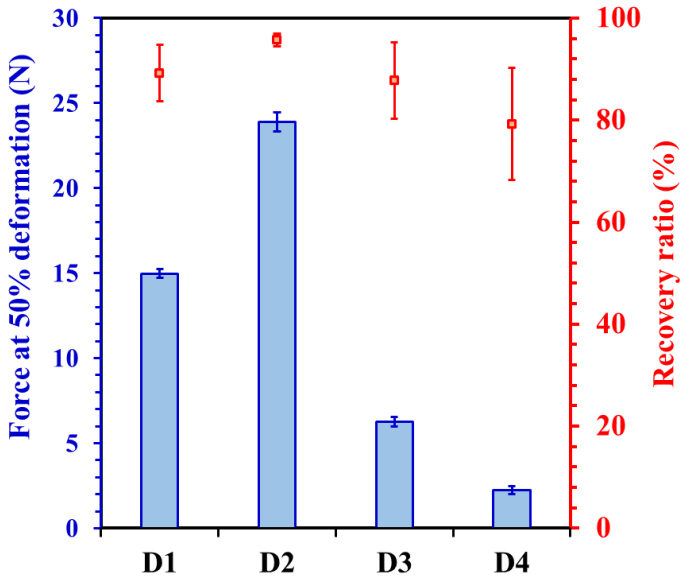

Figure 5-9 The required force for 50% deformation during compressive loading and the measured total recovery after unloading.

5.3.4 Three-point bending test

Bending is another important characteristic of a NiTi stent, both during the insertion stage when the stent is navigated to the area of blockage and when the stent is deployed in a certain angled artery. In this regard, the bending angle is usually measured by employing a three-point bending setup, shown schematically in Figure 5-10(a). Force is applied to the stent in a radial direction up to the point that major failure occurs. In other words, during the test, the force is increased by the increase in the bending angle to a maximum value and subsequently decreases by the occurrence of strut dislocation or minor fractures, leading to an ultimate catastrophic fracture or kinking. The bending angles at these two

points were extracted from the raw data, as represented in Figure 5-10(b). Accordingly, the highest bending angle at the maximum load could be achieved for D2, exhibiting a 17.4° of deformation. D3 is showing a close value of 16.3°, while D1 and D2 were capable of having a 12.6° and 10.2° angle at maximum pressure. By further loading, the bending angle would start to increase but minor failures adversely affect the structural stability of the stents resulting in lower load values and eventually a major failure. For the second stage, D1 takes the lead, showing the ability to be bent to 27.9° despite some minor issues before failure. In the literature, a wide range of bending angles have been reported [35,36], and while some studies are pointing out kinking at angles higher than 10° [5,37], others could acquire higher deflection angles, as was established in a study by Nikanorov et al. [38] in which promising results were obtained for bending up to 48°.

Although the results of deformation recovery during loading-unloading compression tests in the radial direction were very promising in the previous step and the acquired values were comparable to available commercial stents, bending results indicates that for the designs selected in this study, the conducted LPBF and post-processing can only yield relatively lower bending angles ranging from the highest 27.9° angle to the lowest value of 16.3°. It is believed that the main reason for obtaining lower bending angles lies within the LPBF process as the number of adherent particles to the surface and the presence of impartially melted powder particles vary in different struts having different angles relative to the building direction. Although considerable improvements could be achieved through electropolishing treatments, nonuniformity still exists at some locations, adversely affecting the bending properties and resulting in early fracture.

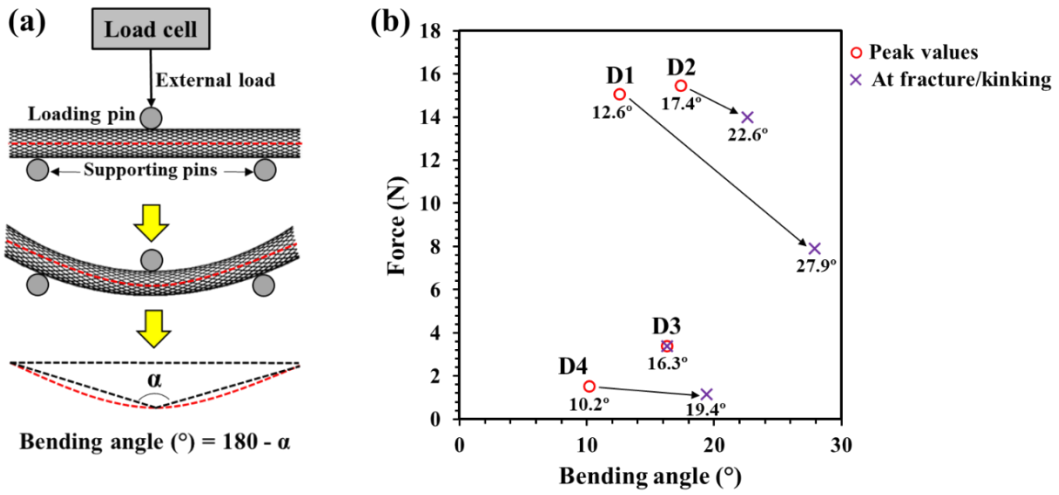

Figure 5-10 (a) schematic illustration of the three-point bending test and the measured bending angle, and (b) the force versus the bending angle at specific stages during the test.

5.3.5 Nanoindentation and superelasticity

In the previous sections, the mechanical properties of the fabricated stents were discussed through the deformation recovery in compression tests and the maximum bending angle in three-point bending tests. It is imperative to note that the acquisition of high deformation recovery as was demonstrated in Figure 5-9 is possible due to the involvement of two critical factors: (1) the mesh-like structure of the stents and (2) the inherent superelasticity of the NiTi alloy. The latter is imperative in terms of application, offering NiTi a competitive advantage in comparison to other biocompatible alloys. In this regard, nanoindentation tests have proven to be a versatile technique for further examination of the processed NiTi properties and superelasticity. In the first step, the Berkovich indenter was utilized to place 20 indents on the radial surface of the stents, and hardness values and elastic modulus were measured according to the Oliver-Pharr method as summarized in Figure 5-11. As anticipated, both the hardness values and elastic modulus for all the

samples are relatively the same since the processing parameters and the post heat treatment conditions used for all samples were identical. Moreover, the recorded hardness and elastic modulus correspond to the values obtained for aged NiTi austenitic structures that consist of Ni_4Ti_3 precipitates [39,40]. The presence of such precipitates is essential for SE purposes since they hinder the movement of the dislocations, increase the critical resolved shear stress (CRSS) and provide the opportunity for the material to experience the occurrence of the stress-induced martensite transformation. The presence of these precipitates in similarly processed materials has been proved in the authors' previous work [18].

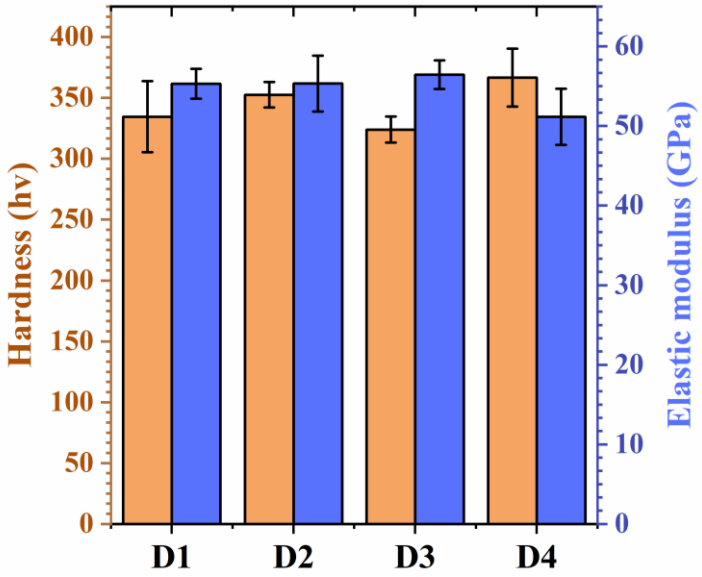

Figure 5-11 The measured hardness (hv) and elastic modulus (GPa) of the fabricated stents with different designs in the radial direction.

To assess the superelastic response of the stents, loading-unloading cycles were conducted by utilizing a spherical tip and the obtained data regarding the indentation force versus indentation depth are represented in Figure 5-12. Clearly, all samples are exhibiting a favorable degree of elastic recovery and enhanced SE properties. To quantitatively analyze

the curves from SE's respective, depth recovery ratio and dissipated energy ratio values were extracted from the curves as noted in Figure 5-13(a).

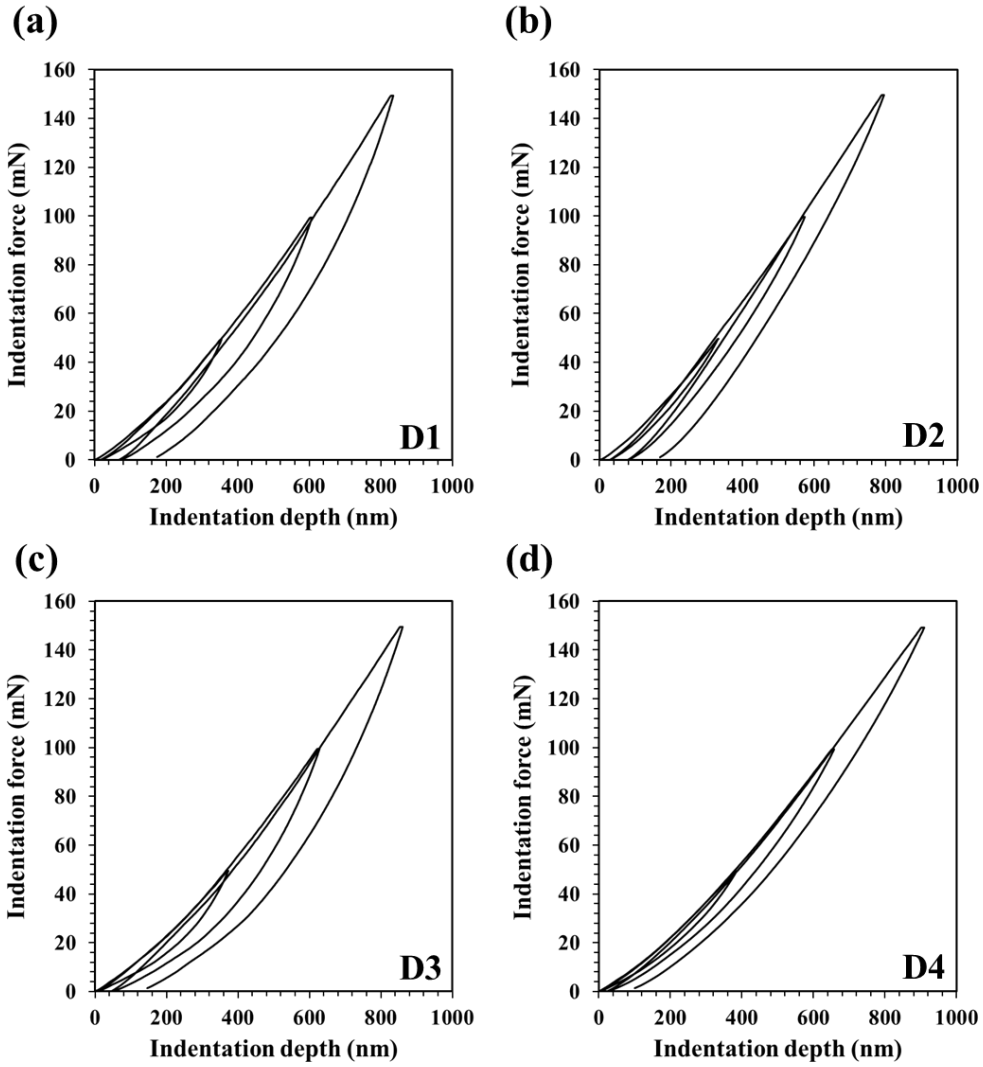

Figure 5-12 A representation of the conducted cyclic loading-unloading nanoindentation tests by utilizing a spherical indenter in order to assess the stents' superelasticity.

According to Figure 5-13(a), the total area under the curve corresponds to the total conducted work (W_{total}) from which the grey area inside the hysteresis denotes the plastic work ($W_{plastic}$) proportional to the dissipated energy and the cyan area under the curve

represents the elastic work ($W_{elastic}$) or the recovery energy. The highest indentation depth at maximum indentation force and the irrecoverable depth after unloading are also indicated by h_{max}, and $h_{irrec.}$, respectively. Accordingly, depth recovery ($\frac{h_{max}-h_{irrec.}}{h_{max}}$ X 100) and dissipated energy ($\frac{W_{plastic}}{W_{elastic}+W_{plastic}}$ X 100) ratios were extracted as summarized in Figure 5-13(b).

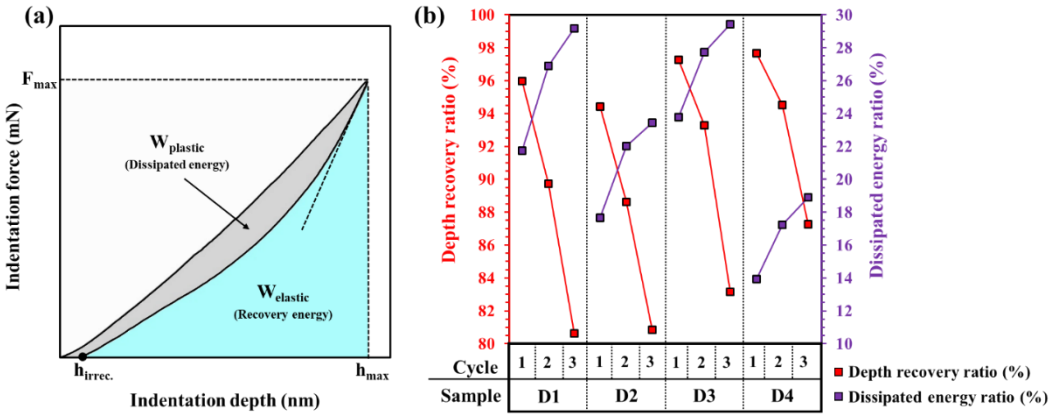

Figure 5-13 (a) the schematic representation of a typical indentation force vs. depth obtained from nanoindentation tests specifying the critical parameters and (b) the calculated depth recovery and dissipated energy ratios for all stent structures in each cycle.

During the first cycle and loading to 50mN, a very high depth recovery ratio of more than approximately 95% was recorded for all samples, which was reduced consecutively in the second and third cycles to values around 80-90% recovery. This high degree of recovery denotes that the NiTi has reached its ultimate potential in exhibiting an improved SE response, attributed mainly to the formation of Ni_4Ti_3 precipitates and the occurrence of restoration mechanisms, through the conducted post-heat treatment as justified by the measured hardness values and discussion provided above.

The sequential drop in recovery could be attributed to the dissipated energy ratio and the involvement of plastic deformation. If loading continues after the occurrence of the stress-induced martensite transformation, plastic deformation mechanisms are activated, resulting in dislocation multiplication and the stabilization of the formed martensite variant, thus limiting the recovery ratio of the material after unloading [41]. As is shown for all samples, the dissipated energy ratio has successively increased in each cycle, signifying that the occurring slip mechanisms are most likely hindering the reverse transformation to occur. Nonetheless, the overall results indicate that the material is presenting a very good level of superelasticity which was mentioned to be one of the two critical factors governing the achieved deformation recovery in compression tests.

5.3.6 Microstructural characterization

Samples were extracted from the processed stents and EBSD inverse pole figure (IPF) maps were obtained from both axial and radial surfaces according to the schematic views presented previously in Figure 5-3. These maps are illustrated in Figure 5-14 considering a reference direction in which the IPFs for axial and radial surfaces are extracted in a direction perpendicular and parallel to the BD, respectively. Comparing the shape of the grains in both surfaces for a selected design indicates that axial surfaces consist of relatively smaller equiaxed grains while radial surfaces comprise enlarged elongated grains in the building direction. As was previously mentioned, during the course of the LPBF process and the occurrence of epitaxial solidification, grains tend to grow in the building direction which is offering the highest heat flow [42]. Furthermore, based on the competitive growth of the dendrites with various crystallographic orientations, those dendrites that are favored based on their growth directions could dominate the microstructure causing a relatively uniform texture throughout the structure [14,43]. For a

cubic material such as NiTi, the easy growth direction has been established to be <001> and usually columnar structures are formed since favorable dendrites can outgrow the other misaligned dendrites. Consequently, the microstructure consists of columnar grains oriented in <001> ||BD, as is evident in images of the radial surfaces in Figure 5-14. Such grain geometry in the radial surfaces leads to the formation of equiaxed grains as plotted in the IPFs perpendicular to the BD, which can also be considered as the loading direction when stent compression tests are conducted. In this regard, a randomized structure with respect to the loading direction in compression is favored in terms of asymmetrical SE [44]. The near-identical microstructures of the processed stents and the similarity of the nanoindentation results point out that the previously acquired different recovery values in compression and the changes in the maximum bending angles are mainly attributed to the mesh structure of the stents as opposed to the superelasticity behavior or the evolved microstructures.

In conclusion, LPBF can be considered as an appealing technique to fabricate high-quality patient-specific NiTi stents with a high degree of recoverability and superelasticity, capable of producing stent components that can potentially compete with the conventionally built commercial stents. The ability to design stents specifically for each patient and the geometry of the blocked or narrowed area, as the biggest advantage of LPBF, can mitigate different issues such as poor patient/stent conformity and stent migration. However, future studies in the biomedical field are absolutely necessary to focus on the biocompatibility of the stents and possible coatings to further improve the stents' functionality prior to any medical implementations.

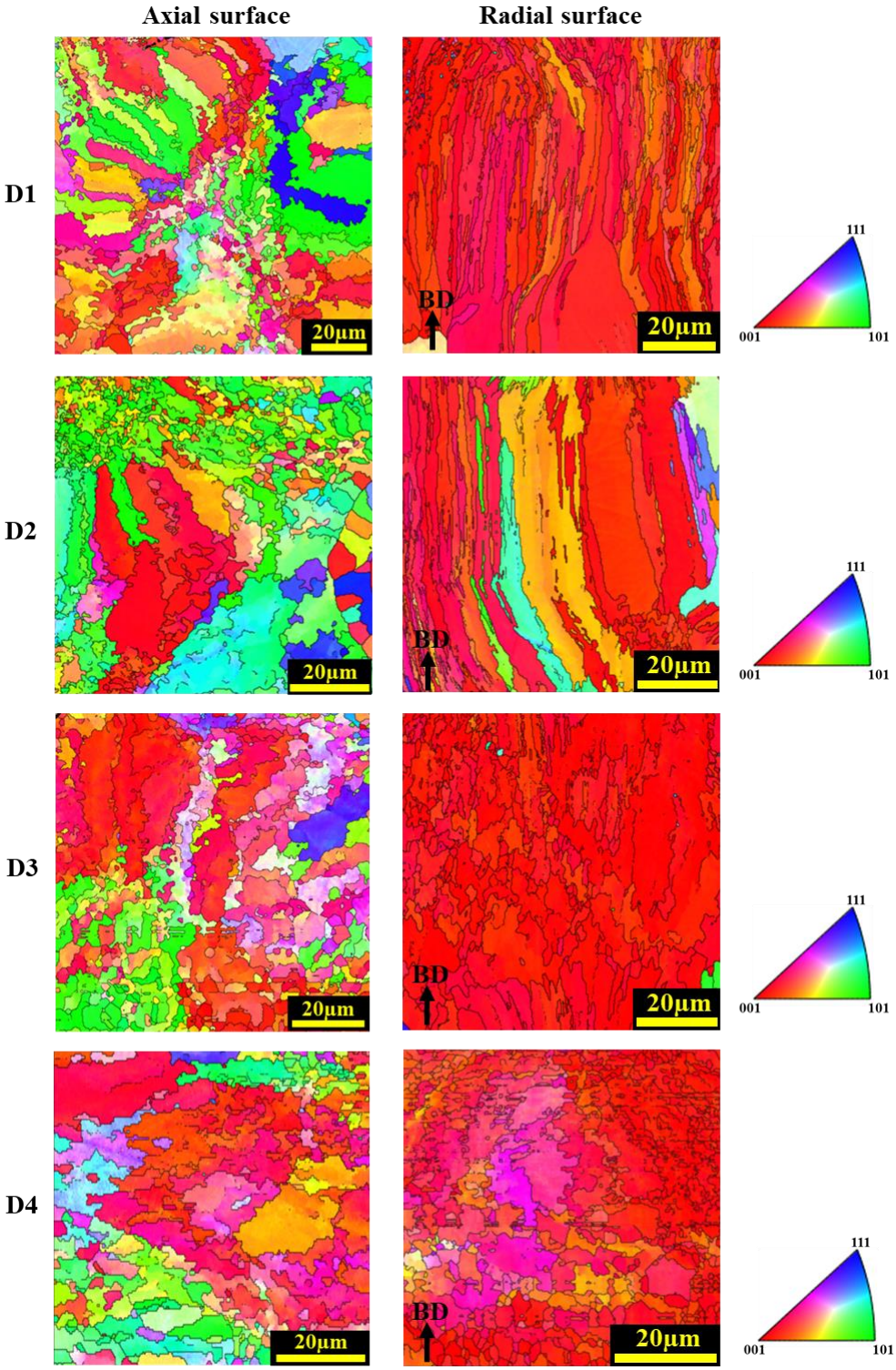

Figure 5-14 IPF maps acquired from the axial surfaces of the stents in a direction perpendicular to the BD and radial surfaces in a direction parallel to the BD.

5.4 Conclusions

NiTi alloys are extensively used in the biomedical industry to fabricate self-expandable stents which are capable of exhibiting excellent superelasticity, recoverability, and biocompatibility. The currently available commercial stents are manufactured in several costly steps including tube preparation, laser micro-cutting, machining, and subsequent surface and heat treatments. Due to the rate of failure, the strict quality requirements, and the design constraints of the mentioned techniques, current commercial stents are not patient-specific on the one hand, and are relatively expensive, on the other hand. The recent progresses in LPBF of NiTi alloys and the ability to readily design parts with complex geometries led the authors to assess the capabilities of the LPBF process to fabricate high-quality stents with four different designs consisting of very thin struts. The fabricated stents were meticulously examined considering properties such as surface characteristics and dimensional accuracy, internal defects, recoverability, superelasticity, and microstructural features. To the best of the authors' knowledge, the mechanical properties and microstructure of additively manufactured NiTi stents have not been comprehensively investigated thus far.

The acquired results indicated that as-built additively manufactured stents have a high average surface roughness (~7-10µm) due to the adherence of impartially melted particles to the stents' surfaces as well as having a low dimensional accuracy. However, a proper electrochemical polishing treatment for just 60s significantly improves the surface roughness ($R_a < 2\mu m$) and greatly enhances the dimensional accuracy. In this regard, very thin struts with thickness values of around 80µm could be successfully produced. The XCT study revealed that all stent structures are highly dense (relative density > 99.8%) without having any major cracks or defects. However, a low level of mostly spherical gas porosities

was witnessed in the fabricated parts formed by the entrapment of gases present in the chamber or the powder particles.

Furthermore, the assessment of mechanical properties showed a high level of deformation recovery through unloading a compressed stent to half of its nominal diameter. The recovery ratio fluctuated from the lowest value of 80% to the highest value of 96%, which is in the range of acceptable deformation levels of stents. As for bending characteristics, The highest acquired bending angle was around 28° for D1, while D3 could only be bent to 16.3° prior to experiencing major fracture or kinking. Early failure was attributed to the non-uniformity of the struts' thicknesses. Nanoindentation tests revealed that the obtained hardness values and elastic modulus for the stents correspond to an austenitic structure and further cyclic loading-unloading indentations demonstrated a remarkable level of superelasticity and recovery values of ~95%. The microstructural images from the extracted axial and radial surfaces of stents revealed the presence of equiaxed, and elongated grains, respectively, and a high <001> texture intensity parallel to the building platform attributed to the occurrence of the epitaxial solidification and competitive grain growth.

The obtained results indicate that the LPBF process has the potential to fabricate high quality stents capable of competing with the current commercial ones in terms of recovery, superelasticity, and surface characteristics. In addition, not only LPBF can offer advantages in terms of customization and production rate but is also an efficient approach to designing patient-specific stents and addressing challenges like stent migration. However, future complementary studies are still required to focus on the biomedical aspects and biocompatibility of the additively manufactured stents.

5.5 References

[1] J. Kendall, F. Serracino-Inglott, C. Banks, P. Jamshidi, M. Attallah, J. Feng, In-vitro study of effect of the design of the stent on the arterial waveforms, Procedia Struct. Integr. 15 (2019) 33–40. doi:10.1016/j.prostr.2019.07.007.

[2] P. Jamshidi, C. Panwisawas, E. Langi, S.C. Cox, J. Feng, L. Zhao, M.M. Attallah, Development, characterisation, and modelling of processability of nitinol stents using laser powder bed fusion, J. Alloys Compd. 909 (2022) 164681. doi:10.1016/j.jallcom.2022.164681.

[3] A.G. Demir, B. Previtali, Additive manufacturing of cardiovascular CoCr stents by selective laser melting, Mater. Des. 119 (2017) 338–350. doi:10.1016/j.matdes.2017.01.091.

[4] C. Jorge, C. Dubois, Clinical utility of platinum chromium bare-metal stents in coronary heart disease, Med. Devices Evid. Res. 8 (2015) 359–367. doi:10.2147/MDER.S69415.

[5] K. Maleckis, E. Anttila, P. Aylward, W. Poulson, A. Desyatova, J. MacTaggart, A. Kamenskiy, Nitinol Stents in the Femoropopliteal Artery: A Mechanical Perspective on Material, Design, and Performance, Ann. Biomed. Eng. 46 (2018) 684–704. doi:10.1007/s10439-018-1990-1.

[6] J.P. Oliveira, F.M.B. Fernandes, R.M. Miranda, N. Schell, J.L. Ocaña, Residual stress analysis in laser welded NiTi sheets using synchrotron X-ray diffraction, Mater. Des. 100 (2016) 180–187. doi:10.1016/j.matdes.2016.03.137.

[7] D. Stoeckel, A. Pelton, T. Duerig, Self-expanding Nitinol stents: Material and design considerations, Eur. Radiol. 14 (2004) 292–301. doi:10.1007/s00330-003-2022-5.

[8] J. Kim, J.K. Park, H.K. Kim, A.R. Unnithan, C.S. Kim, C.H. Park, Optimization of electropolishing on NiTi alloy stents and its influence on corrosion behavior, J. Nanosci. Nanotechnol. 17 (2017) 2333–2339. doi:10.1166/jnn.2017.13324.

[9] A. Safdel, M.A. Elbestawi, Distortion and printability of stent structures in laser

powder bed fusion processing of NiTi alloys, Mater. Lett. 300 (2021) 130163. doi:10.1016/j.matlet.2021.130163.

[10] D.J. McGrath, B. O′Brien, M. Bruzzi, P.E. McHugh, Nitinol stent design – understanding axial buckling, J. Mech. Behav. Biomed. Mater. 40 (2014) 252–263. doi:10.1016/j.jmbbm.2014.08.029.

[11] X. Li, S. Hao, B. Du, B. Feng, H. Li, P. Qiu, B. Huang, L. Cui, Y. Yang, High-Performance Self-Expanding NiTi Stents Manufactured by Laser Powder Bed Fusion, Met. Mater. Int. (2022). doi:10.1007/s12540-022-01317-2.

[12] L. Yan, S.L. Soh, N. Wang, Q. Ma, W.F. Lu, S.T. Dheen, A.S. Kumar, J.Y.H. Fuh, Evaluation and characterization of nitinol stents produced by selective laser melting with various process parameters, Prog. Addit. Manuf. 7 (2022) 1141–1153. doi:10.1007/s40964-022-00289-4.

[13] S. Maffia, V. Finazzi, F. Berti, F. Migliavacca, L. Petrini, B. Previtali, A.G. Demir, Selective laser melting of NiTi stents with open-cell and variable diameter, Smart Mater. Struct. 30 (2021). doi:10.1088/1361-665X/ac1908.

[14] T. DebRoy, H.L. Wei, J.S. Zuback, T. Mukherjee, J.W. Elmer, J.O. Milewski, A.M. Beese, A. Wilson-Heid, A. De, W. Zhang, Additive manufacturing of metallic components – Process, structure and properties, Prog. Mater. Sci. 92 (2018) 112–224. doi:10.1016/j.pmatsci.2017.10.001.

[15] J.L. Bartlett, X. Li, An overview of residual stresses in metal powder bed fusion, Addit. Manuf. 27 (2019) 131–149. doi:10.1016/j.addma.2019.02.020.

[16] A. Safdel, M.A. Elbestawi, New Insights on The Laser Powder Bed Fusion Processing of a NiTi Alloy and The Role of Dynamic Restoration Mechanisms, J. Alloys Compd. 885 (2021) 160971. doi:10.1016/j.jallcom.2021.160971.

[17] D. Herzog, V. Seyda, E. Wycisk, C. Emmelmann, Additive manufacturing of metals, Acta Mater. 117 (2016) 371–392. doi:10.1016/j.actamat.2016.07.019.

[18] A. Safdel, N. Zaker, G.A. Botton, M.A. Elbestawi, The role of texture and restoration mechanisms in defining the tension-compression asymmetry behavior

of aged NiTi alloys fabricated by laser powder bed fusion, Mater. Sci. Eng. A. 864 (2023) 144592. doi:10.1016/j.msea.2023.144592.

[19] S. Saedi, A.S. Turabi, M.T. Andani, C. Haberland, H. Karaca, M. Elahinia, The influence of heat treatment on the thermomechanical response of Ni-rich NiTi alloys manufactured by selective laser melting, J. Alloys Compd. 677 (2016) 204–210. doi:10.1016/j.jallcom.2016.03.161.

[20] C. Haberland, H. Meier, J. Frenzel, On the Properties of Ni-Rich NiTi Shape Memory Parts Produced by Selective Laser Melting, in: Smart Mater., 2013: p. 97. doi:10.1115/smasis2012-8040.

[21] S. Saedi, A.S. Turabi, M.T. Andani, N.S. Moghaddam, M. Elahinia, H.E. Karaca, Texture, aging, and superelasticity of selective laser melting fabricated Ni-rich NiTi alloys, Mater. Sci. Eng. A. 686 (2017) 1–10. doi:10.1016/j.msea.2017.01.008.

[22] P.R. Halani, I. Kaya, Y.C. Shin, H.E. Karaca, Phase transformation characteristics and mechanical characterization of nitinol synthesized by laser direct deposition, Mater. Sci. Eng. A. 559 (2013) 836–843. doi:10.1016/j.msea.2012.09.031.

[23] A. Safdel, A. Zarei-Hanzaki, A. Shamsolhodaei, P. Krooß, T. Niendorf, Room temperature superelastic responses of NiTi alloy treated by two distinct thermomechanical processing schemes, Mater. Sci. Eng. A. 684 (2017) 303–311. doi:10.1016/j.msea.2016.12.047.

[24] P.J. Withers, C. Bouman, S. Carmignato, V. Cnudde, D. Grimaldi, C.K. Hagen, E. Maire, M. Manley, A. Du Plessis, S.R. Stock, X-ray computed tomography, Nat. Rev. Methods Prim. 1 (2021). doi:10.1038/s43586-021-00015-4.

[25] Y. Zhou, A. Fillon, H. Jabir, D. Laillé, T. Gloriant, Investigation of the superelastic behavior of a Ti-16Zr-13Nb-2Sn sputtered film by nanoindentation, Surf. Coatings Technol. 405 (2021). doi:10.1016/j.surfcoat.2020.126690.

[26] A. Shamsolhodaei, A. GhateiKalashami, A. Safdel, A.R.H. Midawi, M.A. Elbestawi, P. Peng, Y.N. Zhou, Resistance spot welding of NiTi shape memory alloy sheets: Microstructural evolution and mechanical properties, J. Manuf. Process. 81 (2022) 467–475. doi:10.1016/j.jmapro.2022.07.006.

[27] Y. Wang, X. Wei, Z. Li, X. Sun, H. Liu, X. Jing, Z. Gong, Experimental Investigation on the Effects of Different Electrolytic Polishing Solutions on Nitinol Cardiovascular Stents, J. Mater. Eng. Perform. 30 (2021) 4318–4327. doi:10.1007/s11665-021-05736-x.

[28] M.C. Cadena, E. Vázquez-Lepe, J.I. Martínez-López, C.A. Rodríguez, E. García-López, Influence of process parameters on surface topography of nitinol manufactured by fiber laser cutting for medical applications, Procedia CIRP. 110 (2022) 82–86. doi:10.1016/j.procir.2022.06.017.

[29] G. Wang, Y. Shen, Y. Cao, Q. Yu, R. Guidoin, Biocompatibility study of plasma-coated nitinol (NiTi alloy) stents, IET Nanobiotechnology. 1 (2007) 102–106. doi:10.1049/iet-nbt:20070011.

[30] M. Burke, B. Clarke, Y. Rochev, A. Gorelov, W. Carroll, Estimation of the strength of adhesion between a thermoresponsive polymer coating and nitinol wire, J. Mater. Sci. Mater. Med. 19 (2008) 1971–1979. doi:10.1007/s10856-007-3274-4.

[31] R. Podila, T. Moore, F. Alexis, A.M. Rao, Graphene coatings for enhanced hemo-compatibility of nitinol stents, RSC Adv. 3 (2013) 1660–1665. doi:10.1039/c2ra23073a.

[32] K. Maleckis, P. Deegan, W. Poulson, C. Sievers, A. Desyatova, J. MacTaggart, A. Kamenskiy, Comparison of femoropopliteal artery stents under axial and radial compression, axial tension, bending, and torsion deformations, J. Mech. Behav. Biomed. Mater. 75 (2017) 160–168. doi:10.1016/j.jmbbm.2017.07.017.

[33] J.F. Dyet, W.G. Watts, D.F. Ettles, A.A. Nicholson, Mechanical properties of metallic stents: How do these properties influence the choice of stent for specific lesions?, Cardiovasc. Intervent. Radiol. 23 (2000) 47–54. doi:10.1007/s002709910007.

[34] Q. Zou, W. Xue, J. Lin, Y. Fu, G. Guan, F. Wang, L. Wang, Mechanical characteristics of novel polyester/NiTi wires braided composite stent for the medical application, Results Phys. 6 (2016) 440–446. doi:10.1016/j.rinp.2016.07.007.

[35] Q. Zheng, P. Dong, Z. Li, X. Han, C. Zhou, M. An, L. Gu, Mechanical characterizations of braided composite stents made of helical polyethylene terephthalate strips and NiTi wires, Nanotechnol. Rev. 8 (2019) 168–174. doi:10.1515/ntrev-2019-0016.

[36] A. Ganguly, J. Simons, A. Schneider, B. Keck, N.R. Bennett, R. Fahrig, In-vitro imaging of femoral artery nitinol stents for deformation analysis, J. Vasc. Interv. Radiol. 22 (2011) 236–243. doi:10.1016/j.jvir.2010.10.017.

[37] A.K. Kareem, M.M. Gabir, I.R. Ali, A.E. Ismail, I. Taib, N. Darlis, O.M. Almoayed, A review on femoropopliteal arterial deformation during daily lives and nickel-titanium stent properties, J. Med. Eng. Technol. 46 (2022) 300–317. doi:10.1080/03091902.2022.2041749.

[38] A. Nikanorov, H.B. Smouse, K. Osman, M. Bialas, S. Shrivastava, L.B. Schwartz, Fracture of self-expanding nitinol stents stressed in vitro under simulated intravascular conditions, J. Vasc. Surg. 48 (2008) 435–440. doi:10.1016/j.jvs.2008.02.029.

[39] S.M. Saghaian, H.E. Karaca, H. Tobe, A.S. Turabi, S. Saedi, S.E. Saghaian, Y.I. Chumlyakov, R.D. Noebe, High strength NiTiHf shape memory alloys with tailorable properties, Acta Mater. 134 (2017) 211–220. doi:10.1016/j.actamat.2017.05.065.

[40] I. Kaya, H.E. Karaca, M. Nagasako, R. Kainuma, Effects of aging temperature and aging time on the mechanism of martensitic transformation in nickel-rich NiTi shape memory alloys, Mater. Charact. 159 (2020) 110034. doi:10.1016/j.matchar.2019.110034.

[41] J.P. Oliveira, F.M. Braz Fernandes, N. Schell, Miranda, Martensite Stabilization During Superelastic Cycling of Laser Welded NiTi Plates, Mater. Lett. 171 (2016) 273–276. doi:10.1016/j.matlet.2016.02.107.

[42] A. Rai, H. Helmer, C. Körner, Simulation of grain structure evolution during powder bed based additive manufacturing, Addit. Manuf. 13 (2017) 124–134. doi:10.1016/j.addma.2016.10.007.

[43] M. Rappaz, C.A. Gandin, Probabilistic modelling of microstructure formation in solidification processes, Acta Metall. Mater. 41 (1993) 345–360. doi:10.1016/0956-7151(93)90065-Z.

[44] K. Gall, H. Sehitoglu, Role of texture in tension-compression asymmetry in polycrystalline NiTi, Int. J. Plast. 15 (1999) 69–92. doi:10.1016/S0749-6419(98)00060-6.

Chapter 5

Conclusions and closing remarks

Near-equiatomic NiTi alloys have been extensively used in the biomedical industry to fabricate bone staples, scaffolds, implants, and most importantly, stents due to their unique functional properties such as shape memory effect and superelasticity. Due to the difficulties of production in conventional approaches, laser powder bed fusion has been considered in recent years by the scientific community to manufacture NiTi components with complex geometries and tailored properties. Although several studies have investigated the optimum processing conditions to fabricate dense NiTi parts, many questions and challenges were overlooked. For instance, the generation of a high level of residual stresses during the process has been commonly recognized, but their impact on the microstructural evolution of the material at elevated temperatures and the possibility of the stimulation of the dynamic recovery mechanisms throughout fabrication has not been assessed before. Accordingly, a novel systematic investigation was initially carried out to examine the involvement of the dynamic recovery and dynamic recrystallization mechanisms. By utilizing theoretical principles, numerical modeling, and experimental data, it was established that the driving force for the occurrence of such mechanisms is

indeed provided during LPBF, and microstructural examinations revealed that dynamic recovery is the dominant mechanism evolving the microstructure of the material. Changing the process parameters affects the contribution of the recovery mechanism and the higher the heat input of the process, the higher the fraction of the subgrains and low angle grain boundaries. Such mechanisms are imperative since functional properties and superelasticity of the fabricated NiTi components are governed by the evolved microstructure and the occurrence of the stress induced martensite transformation. As a result, the optimum processing conditions to fabricate dense NiTi parts with the desired properties were introduced.

A comprehensive understanding of the asymmetrical superelastic response of LPBF processed NiTi alloys which are capable of exhibiting enhanced superelasticity was also another critical topic, previously overlooked. For samples produced by the identified optimum processing parameters, a series of post heat treatments were conducted and SE was assessed in both tensile and compressive deformation cycles. Such a study is crucial since in most applications NiTi components experience multiple deformation modes, and therefore contributions could be made to help the industry to develop highly functional parts. It was found that aging at 550°C for only 6 hours can promote the formation of fine Ni_4Ti_3 precipitates and activate the static restoration mechanisms leading to favorable SE. The texture of the material was also affected by the aging process and degree of recrystallization, resulting in changes in the asymmetry parameters. The differences in the asymmetry parameters were also justified by utilizing fundamental theories. It was concluded that aging at 550°C for 6 hours for a sample fabricated by a 90º scanning strategy, results in favorable compressive SE and a lower level of asymmetry, while

samples manufactured by rotation angles of 67º are capable of exhibiting superior SE, although asymmetry is intensified.

In the second phase, the feasibility of fabricating thin NiTi stents was scrutinized by using two different volumetric energy densities (56 and 125J/mm^3) and focusing on the residual stresses, delamination, and distortion. Lower energy levels were proven to be beneficial in terms of residual stresses and process continuity. For the first time, the acquired results pointed out the fabrication feasibility and processability of the designed thin NiTi stent structures via LPBF given that lower volumetric energy density values are employed, and accordingly, very thin mesh structured stents were successfully fabricated. Nonetheless, many challenges including high average surface roughness and low dimensional accuracy were encountered, demanding further analyses.

As was mentioned, the ability to manufacture patient-specific NiTi stents was acknowledged and as a result, further steps were taken to evaluate the capabilities of LPBF to manufacture stents having comparable properties in a comparison with commercial stents produced by conventional approaches. In this regard, various properties such as average surface roughness, dimensional accuracy, structural integrity, and mechanical properties were examined, offering novel conclusions. It was found that although the initial average surface is higher than the competition, surface modification treatments such as electropolishing could provide a very smooth surface suitable for application or novel coating processes. Furthermore, remarkable recoverability of up to 96% could be achieved, while the bending angle was limited to the maximum value of ~28°. Overall, it can be concluded that LPBF has the potential to substitute the commercial approaches to fabricate NiTi stents and offers a higher production rate and most importantly, the freedom of designing patient-specific NiTi stents.

Last but not least, the author would like to suggest areas and topic for future research which were not in the scope of this work but are imperative in terms of future advancements in LPBF processing of NiTi alloys and the production of stents. It was found out that the texture can be manipulated through the changes in the scanning strategy, however, all samples in this study were fabricated in a direction in which the loading direction is perpendicular to the loading direction. Changes in the building orientation and scanning strategy, simultaneously, could contribute to different microstructures, providing a higher degree of tunability in terms of superelasticity and asymmetrical parameters.

It was stated that fabrication of stents via LPBF is feasible and different designs were assessed considering surface characteristics, mechanical properties, and microstructural evolutions. Nonetheless, further studies are necessary to modify the introduced design or suggest new ones, especially with respect to the subsequent electropolishing treatments. Nonuniformities was recognized as one of the issues deteriorating the mechanical properties of the stents after fabrication which could be mitigated by having differently designed stent structures. Moreover, fatigue properties of additively manufactured stents should be further scrutinized, especially for stents that are deployed in areas that are continuously deformed (e.g., femoropopliteal artery). These studies could contribute to a set of design rules which could be readily used to identify the best design candidate for certain application. Furthermore, nickel-ion release and effects of surface roughness should be further investigated to determine biocompatibility levels. In this regard, it was observed that the obtained surface roughness values for the stents produced in this study could promote stent/coating adhesions which could be a point of focus for remarkable enhancements in biocompatibility.